SLAC-247
CONF-811233

PROCEEDINGS OF THE SLC WORKSHOP ON EXPERIMENTAL USE OF THE SLAC LINEAR COLLIDER

SLAC-REPORT-247

MARCH 1982

PREPARED FOR THE DEPARTMENT OF ENERGY

UNDER CONTRACT NUMBER DE-AC03-76SF00515

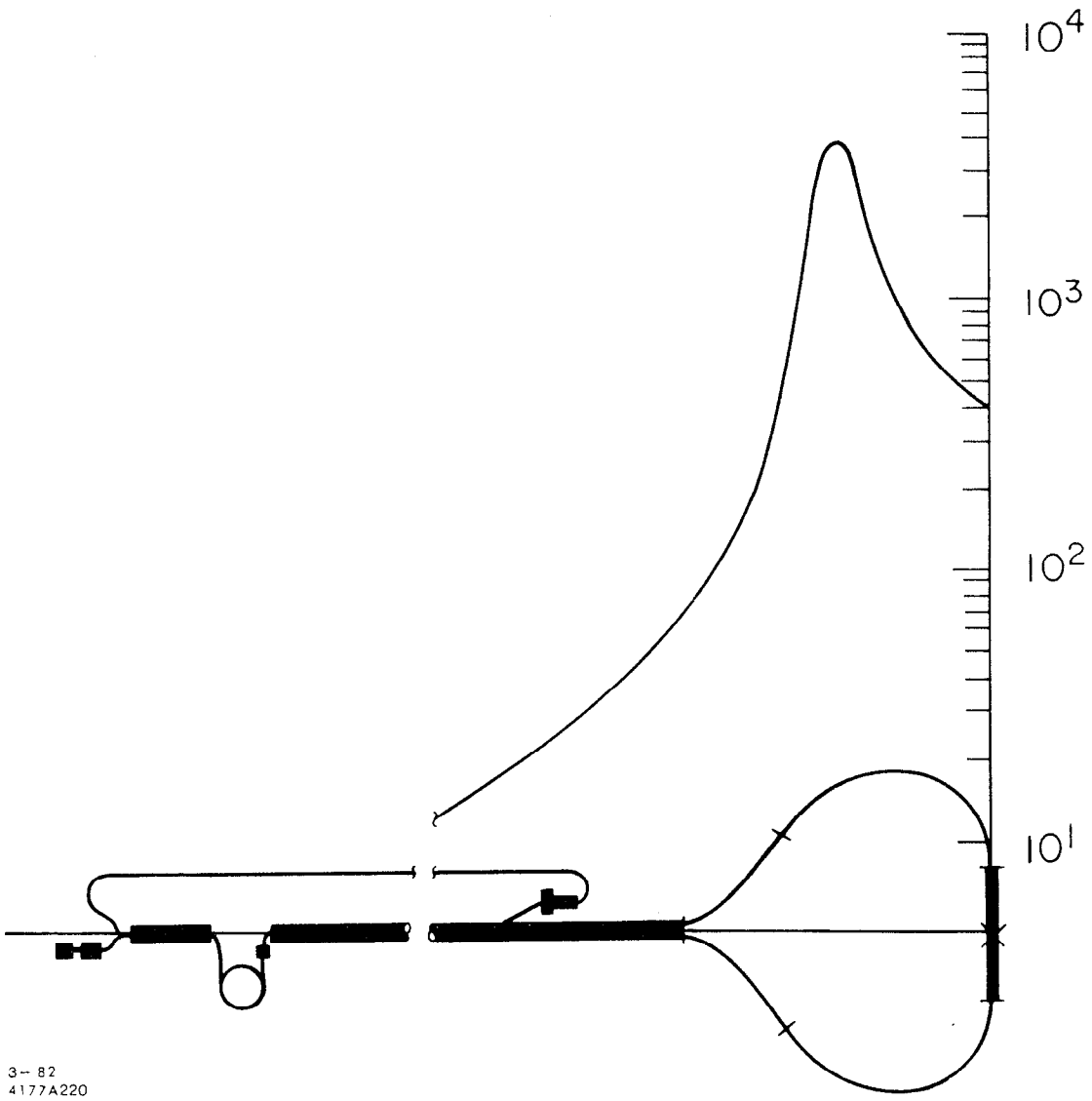

NEW MACHINE - NEW PHYSICS

The schematic of the SLAC Linear Collider (SLC) forms a natural energy scale in this plot of the relative multi-hadron cross section which peaks sharply at the predicted location of the Z°.

TABLE OF CONTENTS

FOREWORD

In March 1981, the SLAC management, together with the SLAC users organization, invited interested physicists to a three day meeting to discuss the laboratory's plans and progress on the new colliding e^+e^- machine--the Stanford Linear Collider (SLC). Those attending were encouraged to join together to study the challenges and opportunities presented by the SLC. So began the SLC Workshop.

About 200 physicists from universities and laboratories in the United States joined eight working groups which focused on the specific topics indicated in the table below. These groups were cochaired by a SLAC physicist and a colleague from the user community; their names are listed in the table. The study of the "Parameters" for experiments on 100 GeV e^+e^- collisions, and the reviews of the state-of-the-art in the four areas of detector technology--"Tracking," "Calorimetry," "Particle Identification" and "Electronics and Computing"--were undertaken from a general standpoint, and not from the particular perspective of a specific experimental proposal. Each group met approximately once per month during the period March through December, including a week-long "Workfest" in August, in which all eight groups met to give an extra 'push' to their specific studies and to communicate their progress to their colleagues working in other areas. The Workshop culminated in a three day meeting in December in which draft reports from the eight groups were reviewed and discussed. These reports were subsequently edited by the cochairman and have been compiled into this Proceedings by William Ash. Giora Tarnopolsky joined the cochairmen of the "Parameters" groups to produce the final report from that group.

Each of the eight sections in these Proceedings is self-contained with its own figure numbers and references. The figures have been inserted in the text to make for convenient reading. Most of the references are to the SLC Workshop Notes--a complete list of all the titles and authors is included as an appendix. These notes are commended to the serious reader who wishes more detailed information or to identify a contact person to follow up specific studies.

I am happy to acknowledge the specific and expert help of the SLAC staff. The SLAC Technical Publications Department managed most of the typing, illustration and assembly of these Proceedings with enthusiasm and professional care. I would like to thank Ms. D. Edminster, L. Loesing, A. Mosher and L. Beers for their hard and very effective organizing and running the three large meetings during the Workshop. I would like to specially thank Ms. Lilian Loesing for her continued administrative support of each of the eight working groups and for organizing the library system for the SLC Workshop Notes. I would also like to thank Ben Shen and David Pellett who helped us chair the March and December meetings of the Workshop.

Finally, it is the physicists who contributed to the Workshop, the working community who committed time and effort over the nine month period of the SLC Workshop, that made these Proceedings possible, and the following list of Participants is presented with great appreciation.

The SLC Workshop has been a very useful endeavor, and I believe that this stage of its work will prove to be a useful guide to everyone in the design of SLC experiments.

David W. G. S. Leith
(SLAC)

SLC Workshop Groups--Topics and Cochairmen

Polarization	Richard Prepost University of Wisconsin	Charles Prescott SLAC
Parameters	Jonathan Dorfan SLAC	George Trilling LBL
Tracking	John Jaros SLAC	Abe Seiden UC, Santa Cruz
Calorimetry	William Ash SLAC	David Hitlin Cal Tech
Particle Identification	Donald Meyer University of Michigan	Daniel Scharre SLAC
Electronics & Computing	Martin Breidenbach SLAC	Vincent Peterson University of Hawaii
Two-Detector Management	John Kadyk LBL	Martin Perl SLAC
Interaction Region	David Leith SLAC	John Matthews Johns Hopkins University

SLC WORKSHOP

LIST OF PARTICIPANTS

G. Abrams
LBL

K. J. Anderson
University of Chicago

W. W. Ash
SLAC

W. Atwood
SLAC

D. Badtke
Johns Hopkins University

P. Baillon
CERN

B. Barnett
Johns Hopkins University

G. Baranko
Indiana University

A. Barbaro-Galtieri
LBL

R. Bell
SLAC

H. H. Bingham
LBL

B. Blumenfeld
Johns Hopkins University

G. Bonneaud
SLAC

J. Brau
SLAC

M. Breidenbach
SLAC

A. Bross
LBL

J. Brown
SLAC

K. Brown
SLAC

F. Bulos
SLAC

D. Burke
SLAC

T. Burnett
University of Washington

M. Cavalli-Sforza
Princeton University

T. Carroll
SLAC

R. Cence
University of Hawaii

A. Clark
LBL

P. Cooper
Yale University

B. Cork
LBL

D. Coward
SLAC

D. Coyne
Princeton University

C. Day
LBL

G. Donaldson
SLAC

J. Dorfan
SLAC

D. Dorfan
UC, Santa Cruz

S. Ecklund
SLAC

K. Einsweiler
SLAC

A. Eisner
UC, San Diego

R. Erickson
SLAC

R. Fabrizio
UC, Santa Cruz

G. Feldman
SLAC

T. Fieguth
SLAC

C. Field
SLAC

G. Fischer
SLAC

W. Ford
University of Colorado

L. Galtieri
LBL

F. Gilman
SLAC

G. Goldhaber
LBL

F. Grancagnolo
UC, Santa Cruz

S. Gray
Argonne

Y. Guo
Yale University

F. Hall
SLAC

G. Hanson
SLAC

J. Hauptman
LBL

C. Heusch
UC, Santa Cruz

D. Hitlin
CIT

R. Hollebeek
SLAC

R. Holsinger
Field Effects, Inc.

D. Hon
Johns Hopkins University

D. Hutchinson
SLAC

W. Innes
SLAC

J. Jaros
SLAC

E. Jenkins
University of Arizona

C. R. Johnson
SLAC

D. Johnson
LBL

J. Johnson
University of Wisconsin

J. Kadyk
LBL

T. Kamae
University of Tokyo

L. Keller
SLAC

A. Kilert
SLAC

K. Kinoshita
UC, Berkeley

W. Ko
UC, Davis

D. Koltick
Purdue University

P. Kooijman
Argonne

P. Kunz
SLAC

R. Lander
UC, Davis

W. Langeveld
NIKEF

A. Lankford
LBL

R. Larsen
SLAC

J. Layter
UC, Riverside

D. Leith
SLAC

L. Levinson
SLAC

A. Litke
Stanford University

N. Lockyer
SLAC

V. Luth
SLAC

G. Lynch
LBL

H. Lynch
UC, Santa Barbara

L. Madansky
Johns Hopkins University

J. Matthews
Johns Hopkins University

D. Meyer
University of Michigan

W. Michael
UC, Davis

E. Miller
UC, San Diego

G. Mills
CIT

P. Mockett
University of Washington

L. Moss
SLAC

M. Nelson
LBL

R. Nelson
SLAC

C. Newman
Princeton University

D. Nitz
University of Michigan

A. Ogawa
SLAC

H. Ogren
Indiana University

R. Oppenheim
Yale University

L. Paffrath
SLAC

S. Parker
University of Hawaii

D. Pellett
UC, Davis

M. Perl
SLAC

D. Perret-Gallix
SLAC

I. Peruzzi
LNF-INFN, Frascati

H. Petersen
SLAC

V. Peterson
University of Hawaii

M. Piccolo
LNF-INFN, Frascati

B. Pifer
University of Arizona

R. Pitthan
SLAC

D. Porat
SLAC

R. Prepost
University of Wisconsin

C. Prescott
SLAC

L. Price
Argonne

B. Ratcliff
SLAC

W. Reay
Ohio State University

D. Rust
Indiana University

A. Sabersky
SLAC

H. Sadrozinski
UC, Santa Cruz

T. Schalk
UC, Santa Cruz

D. Scharre
SLAC

K. P. Schuler
Yale University

A. Seiden
UC, Santa Cruz

A. Seidl
University of Michigan

H. Sens
NIKEF

J. Shafer
University of Massachusetts

G. Shapiro
LBL

S. Shapiro
SLAC

J. Siegrist
SLAC

C. Sinclair
SLAC

D. Smith
UC, Santa Cruz

J. Spencer
SLAC

H. Steiner
LBL

R. Stiening
SLAC

S. St. Lorant
SLAC

D. Stork
UC, Los Angeles

R. Stroynowski
CIT

S. Suzuki
SLAC

G. Tarnopolsky
SLAC

T. Tauchi
SLAC

R. Taylor
SLAC

G. Trilling
LBL

K. Ukai
INS-Tokyo University

J. Va'Vra
SLAC

W. Vernon
UC, San Diego

F. Villa
SLAC

D. Walz
SLAC

S. Wang
SLAC

J. Weiss
Argonne

W. Wenzel
LBL

M. Werlen
SLAC

H. H. Williams
University of Pennsylvania

S. Williams
SLAC

R. Wilson
Purdue University

D. Wood
Purdue University

M. Woodley
SLAC

R. K. Yamamoto
MIT

S. Yellin
UC, Santa Barbara

D. E. Yount
University of Hawaii

F. Harris
University of Hawaii

J. Strait
SLAC

POLARIZATION

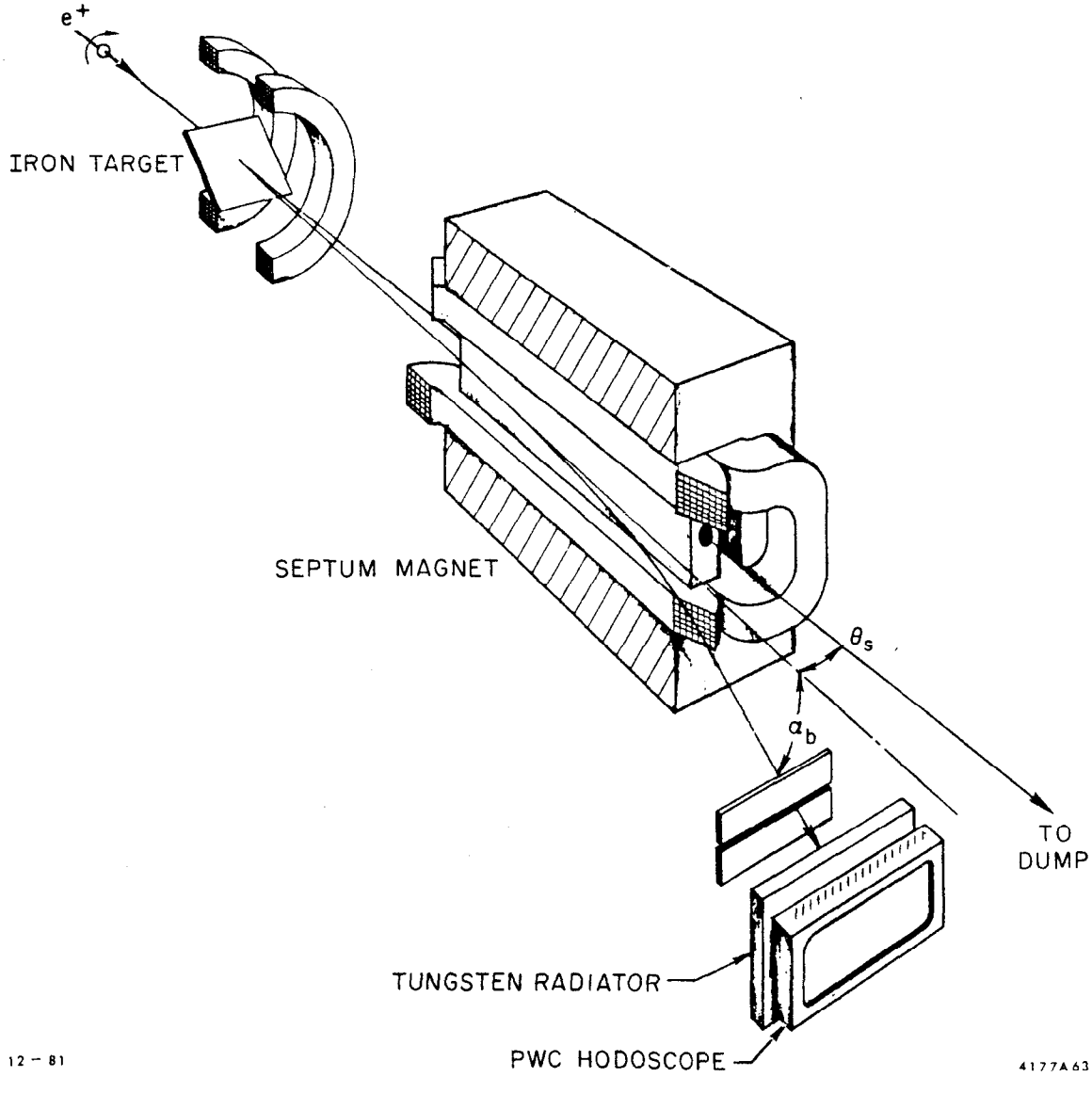

POLARIZATION

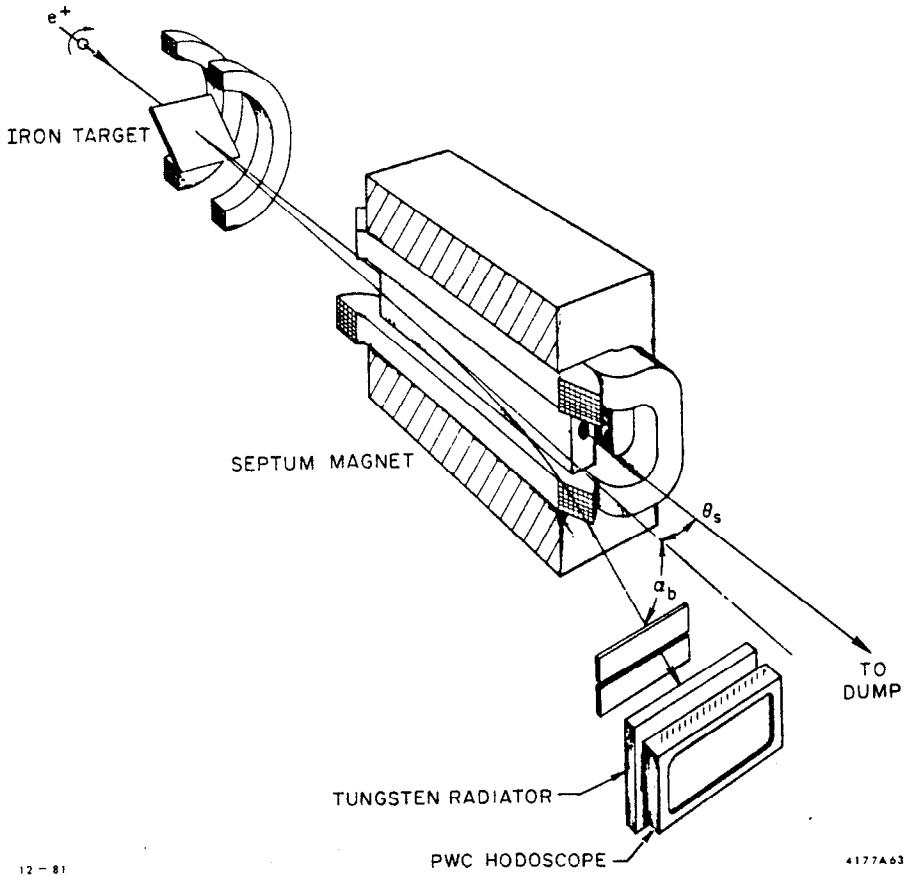

I. INTRODUCTION

Electroweak interactions at sufficiently high energies are expected to exhibit sizeable spin-dependent effects. In e^-e^+ annihilation at our present available energies of PETRA and PEP, and beyond, the weak neutral current begins to contribute along with the electromagnetic current, and at high enough energies should strongly dominate these processes. Experiments using transversely polarized e^+e^- beams have shown azimuthal asymmetries in jet axes as expected for production from spin 1/2 constituents. Measurements with longitudinal spin have not been attempted due to the complexities associated with rotating the spin. Although the electromagnetic current exhibits no helicity preference, the weak neutral current is expected to have sizeable helicity-dependent effects and longitudinal polarization should play a significant role in future e^+e^- experiments. In the SLAC SLC proposal, the linear accelerator will be upgraded to provide 50 GeV e^- bunches and 50 GeV e^+ bunches which are brought into collision by a two-arm transport system located at the end of the accelerator structure. Linear machines accelerate polarized beams without loss of polarization, and techniques for producing the intense, short polarized beams suitable for injection have already been demonstrated in tests. The charge to this study group has been to study the physics of polarized beams, how to integrate polarization into the general schemes of SLC project, and how best to exploit the capabilities of polarization in the experimental studies of the electroweak interactions. In this report, we discuss the present status of polarized beam work at SLAC, transport and depolarization of the beams, polarization monitoring schemes, and physics considerations connected with polarization.

II. STATUS OF POLARIZED BEAMS AT SLAC

The present status of polarized beam work at SLAC will be described here. Considerable experience in producing and accelerating polarized electrons exists from previous work, and current activities related to SLC requirements for polarized beams continue. Production and acceleration of polarized electrons has not been included as topics to be studied by the workshop because the subjects are closely connected with and integrated into the design parameters of the SLC. Polarized electrons are produced by a laser-driven photoemission source using gallium-arsenide or some related semiconductor material as a cathode. Such techniques require expertise in ultra-high vacuum techniques, high voltage guns and optics, and laser devices. The design of a suitable device requires close coordination with accelerator physicists to provide compatibility with the injecter section. This work has been in progress for some time under the leadership of C. K. Sinclair who has had experience with similar devices in the past.

A. The Polarized Electron Gun

Figure 1 shows a sketch of the polarized electron source for the collider. The cathode matherial, gallium arsenide, is illuminated with circularly polarized light from a laser. Electrons in the valence band of the gallium arsenide crystal are pumped into the conduction band, and subsequently photoemitted with a probability which depends on the nature of the surface. Properly cesiated surfaces (i.e., surfaces with monolayers of cesium and oxygen) can have photoemission probabilities of several percent. Circular polarization of the laser pump light leads to photoemitted electrons with spins aligned along their direction of motion. Reversing the sign of the laser circular polarization reverses the spin direction of the electrons. The reversal of circular polarization is easily achieved and leads to electron spin reversals with virtually no influence on other beam parameters. Successive beam pulses of opposite spin are readily delivered, and systematic errors associated with the spin-dependent measurements can be largely cancelled.

The laser which illuminates the GaAs cathode is a modified version of the laser oscillator employed in the SHIVA laser fusion work at LLL.

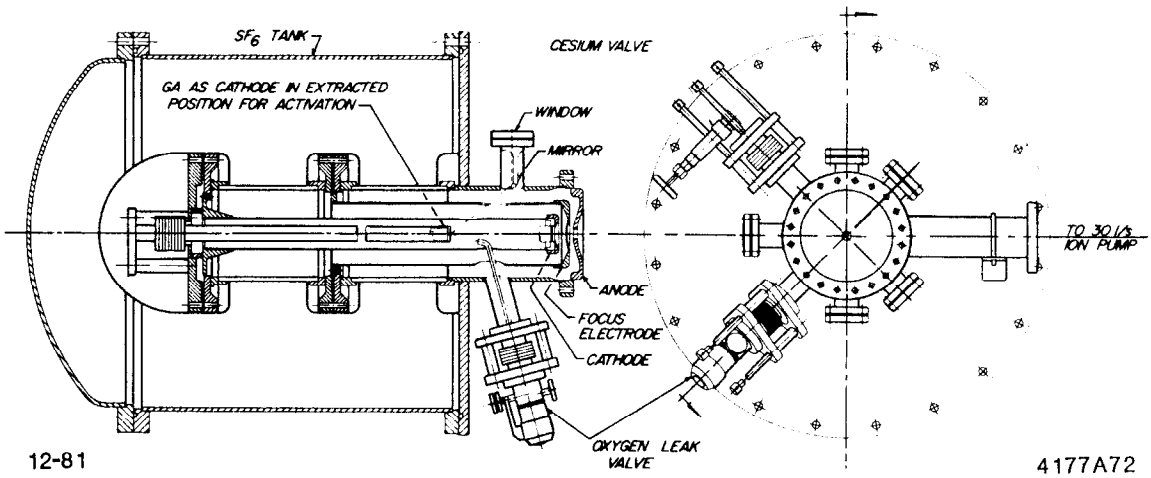

Fig. 1. The high current polarized electron gun for the SLC. The gallium arsenide cathode is shown in the extracted position where it is activated with cesium and oxygen. In the normal position, polarized electrons are photoemitted from the cathode with a polarized laser beam, not shown.

Modifications include operating at a high rep rate (180 Hz), and operation at the correct wavelength to deliver maximum electron beam polarization. The laser operates nominally at 1.06 μm, while the proper wavelenth for high polarization is about 0.75 μm. To obtain the proper wavelength, the laser fundamental is first doubled. This doubled light is then used to pump a dye laser, tuned to operate at the desired wavelength. The laser is both Q-switched and actively mode-locked to the 48th subharmonic of the linac rf. The mode-locking provides pulses of variable width, accurately phased to the linac rf, so the electron pulses can be adjusted to occur at the proper time. Individual mode-locked pulses are selected from the laser output pulse train to provide the two beam bunches required for the collider operation.

Electron injection into the linac for SLC operation is done by prebunching the beam from an electron gun at a subharmonic of the 2856 MHz linac frequency. Currently this frequency is 178.5 MHz, though in the final version it will be either 119 MHz or 238 MHz. This subharmonic bunching allows the gun to deliver the required 5×10^{10} electrons over a period of about 1 nsec, i.e., a peak gun current of about 8A. Allowing for beam losses at injection and early in the linac, we have designed the polarized gun for the SLC to deliver a space-charge limited current of 15A from a 1-cm diameter cathode at 200 kV. The actual cathode diameter is 1.5 cm, so an additional factor of two in beam current is available in principle. By varying the size of the illuminated area on the photocathode, we expect to be able to deliver space-charge limited beams of any peak current below the maximum. It is desirable to operate in the space-charge limited regime to obtain independence of beam current on laser intensity, i.e., pulse-to-pulse stability.

Polarization values of 40% to 45% have been obtained from GaAs cathodes. These values are determined primarily by the band structure of GaAs and the angular momentum selection rules which apply to circularly polarized photons which pump electrons from the valence band to the conduction band.

There is a program underway to develop materials which will deliver higher electron polarization. Several different avenues are being pursued, including the application of uniaxial stress to GaAs, the use of

ternary chalcopyrites, and the use of multilayer hererostructures. Each of these techniques is demonstrably capable of giving higher electron polarization, and so technical, rather than fundamental, problems remain to be solved. Long term, there is high likelihood for success from one or another of these approaches.

Currently, the gun and the laser are both operational. The gun has not been installed on the collider injector system yet, due to an inadequate vacuum in this area, but is operational in a lab. The laser is operational also, although at reduced rep rate and to date not at the proper wavelength. Work is actively underway to increase the rep rate, and to shift the operating wavelength to the correct value. Currently a rep rate of 100 Hz has been obtained, and operation in a frequency doubled mode is standard.

B. The Damping Ring

Two small rings located after the first sector of the linac serve to reduce the beam emittance through radiation damping. The electron beam passes through one of these rings and is stored in it for a duration equal to the time between machine pulses, 5.6 msec. For polarization work, preservation of beam polarization through the damping ring requires particular manipulation of the spin, and care in the damping ring design to avoid depolarization. The design energy of the ring is 1.21 GeV. To preserve the spin in such a ring, the spin vector must be oriented normal to the plane of the ring, and machine spin resonances must be avoided. To orient the spin properly, a superconducting solenoid is placed on the incoming beam line at an appropriate location. Longitudinal spin in the first linac sector is precessed to transverse (32.8 degrees of bending accomplish this) then rotated to perpendicular in the solenoid (6.34 Tesla-meters are required). Extracted beams leave with the spin normal to the damping ring plane. Two more superconducting solenoids, each capable of 6.34 Tesla-meter integral field strength, separated by 32.8^{o} of bend and by 32.8^{o} bend from the linac, serve to orient the final spin in any arbitrary direction in the linac. Currents in the last two solenoids can be adjusted, and by these means the spin direction at the interaction point of the experiments can be controlled. The experimental program requires longitudinal spin (transversely polarized electrons

annihilating an unpolarized positrons yields no observable spin-related effects) at the interaction point. The second and third solenoids permit the correct orientation in the experiment to be achieved.

C. Spin Motion and Depolarization in the Transport Arms

As the beam passes through the linac, transport arms and final focus systems of the SLC the electron spin vector will rapidly precess and, at 50 GeV/c, is expected to make about 30 revolutions before the beam reaches the experimental interaction point. Previous experiments have successfully transported polarized electrons through the linac and indicate that essentially no loss of polarization occurs in the acceleration process. Depolarization will occur, however, in the transport arms and final focus due to the finite energy spread in the beam and to quantum fluctuations that lead to emission of synchrontron radiation. Additional depolarization is expected to occur during the beam-beam interaction.

First estimates indicate that polarization at the interaction point during the beam-beam collision can be expected to be 80% of that produced by the electron gun. The results of a model calculation of the spin projections at the interaction region are shown in Fig. 2. Notice that the peaks and zeros of the polarization seen in this figure can be arbitrarily shifted in energy by appropriately adjusting the solenoids at the output of the damping ring.

In order to allow more exact calculations of polarization transport in the SLC, the ray tracing program TURTLE has been modified to include spin precession. Spin motion can be conveniently written in terms of laboratory fields as[1]

$$\frac{d\theta_s}{dt} = \frac{1}{\gamma}\left(\frac{ge}{2m}\right)\left\{\gamma\left[\vec{B}_\perp - \vec{v}\times\vec{E}\right] + \vec{B}_\parallel\right\} - (\gamma - 1)\frac{e\vec{B}_\perp}{m\gamma} \quad , \tag{1}$$

where g is the electron gyromagnetic ratio and γ is the usual Lorentz boost factor. Since $\gamma \approx 10^5$ for 50 GeV electrons, then ignoring electric fields and purely solenoidal magnetic elements, Eq. (1) becomes

$$\frac{d\theta_s}{dt} = \left[1 + \gamma\left(\frac{g-2}{2}\right)\right]\frac{e\vec{B}_\perp}{m\gamma} \tag{2}$$

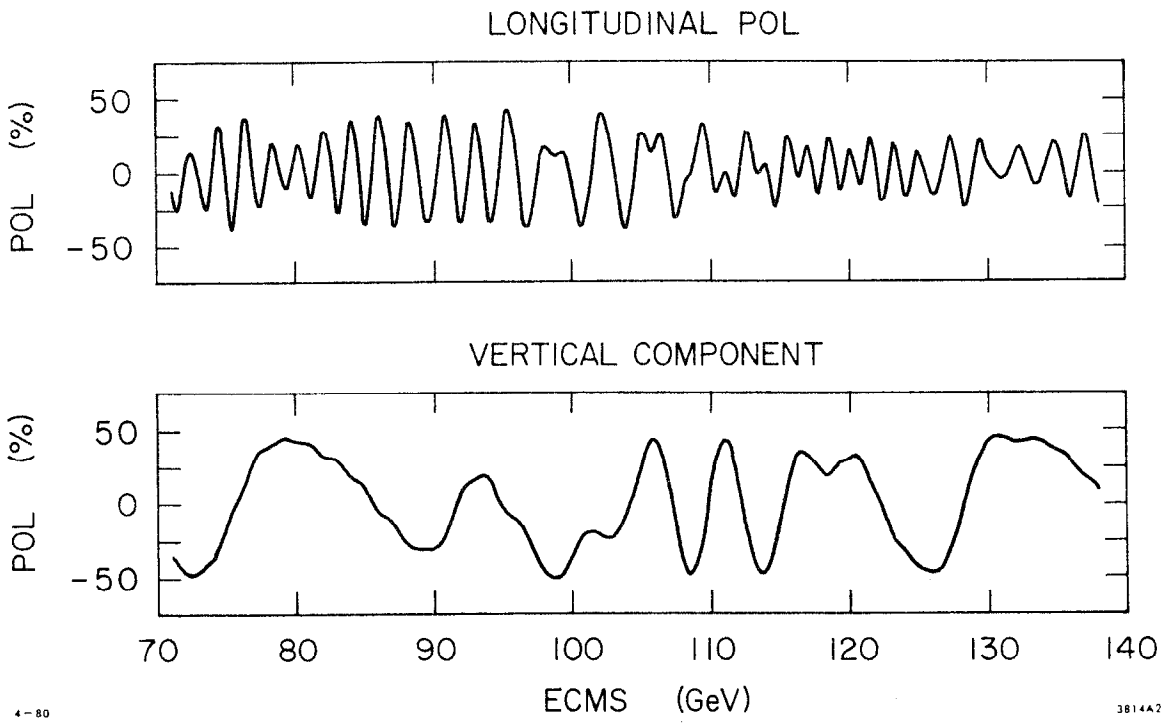

Fig. 2. Two spin components in the interaction region are shown for a wide range of energies, for longitudinal spin (50% polarized) in the linac. This calculation uses a beam transport system which approximates the vertical and horizontal bends of the collider north arc, and includes depolarization due to the finite energy spread of the beam.

The spin rotation of an electron passing through a uniform magnetic field is then given in terms of the momentum rotation $\Delta\vec{\theta}_p$ as

$$\Delta\vec{\theta}_s = \left[1 + \gamma\left(\frac{g-2}{2}\right)\right] \Delta\vec{\theta}_p \quad . \tag{3}$$

Equation (3) represents an approximation to the actual spin motion which, for the magnetic elements and narrow beams in the SLC, is extremely accurate. Notice that, for 50 GeV/c electrons, the factor $\gamma \frac{g-2}{2} \approx 114$.

Calculation of the spin motion in several of the currently conceived final focus systems confirm that essentially no loss of polarization occurs. Similar calculations for the transport arms will be carried out as detailed designs become available.

III. POLARIZATION MONITORING

Accurate knowledge of beam polarization is extremely important to all polarization measurements. Measurement of beam polarization is straightforward by techniques already used in experiments. The polarization working group has been considering two polarization monitors, described below, one using Møller scattering, and one using Compton scattering.

A. The Møller Polarimeter

The Møller polarimeter is based on the measurement of beam polarization through the spin-dependent components of elastic electron-electron scattering, a well-known QED process. At high energies, near 90^{o} in the CMS, there is a significant difference in scattering cross sections for longitudinal spins which are parallel versus anti-parallel. The asymmetry

$$A_M = \frac{\sigma_p - \sigma_a}{\sigma_p + \sigma_a} \tag{4}$$

where σ_p (σ_a) refers to the differential cross section for parallel (anti-parallel) spin alignment, reaches a value close to 7/9. For a beam of fractional polarization P_e, the measured experimental asymmetry is related to A_M by

$$A_{exp} = P_e A_M \tag{5}$$

The experimental asymmetry is proportional to P_e. Polarized target electrons can be obtained by magnetizing a foil of magnetically permeable material such as Supermendur. The material is easy to saturate magnetically, and a fraction f of the electrons align their spins along the field lines inside the material. The material may not be oriented with the spins parallel to the incident beam, but at an angle θ. Thus, the expression for the asymmetry becomes

$$A_{exp} = f \cos\theta P_e A_M \tag{6}$$

The uncertainty on the coefficient f is small (less than a percent) so that errors on A_{exp} (and therefore P_e) are dominated by other effects, mostly scattering of electrons off nuclei in the target material.

Counting rates in a simple Møller detector (to be described) are relatively high (approximately 10^2 per pulse of 5×10^{10} electrons into a .001 inch thick foil) and sufficient data to measure A_{exp} accurately require only a few minutes of exposure.

Systematic errors limit the precision of the measurements and values of $\Delta P_e/P_e \approx .05$ should be anticipated. The technique of Møller scattering should provide a good monitor of beam polarization at all times during data taking runs.

A technique of coincidence Møller scattering, where both final state electrons are detected, has been considered. The coincidence requirements eliminate the main background to single Møller detection, scattering from the target nuclei. The problems of how to measure these events in the presences of high counting rates and short duty cycle, however, have not been solved at this time.

Single arm Møller events can be isolated from general backgrounds by using two-body kinematic constraints. In a scattering angle versus momentum plot, Møller events stand out above a general background, in part enhanced by the large cross section for this process relative to competing processes. In practice, apertures which define a lab angle θ, and a spectrometer which disperses momentum, followed by a suitable electron-sensitive hodoscope serve as the basic monitor. Figure 3 shows a sketch of such a device designed to operate near the e^- beam dump. This choice of location permits continual operation while the beam is being delivered to an experiment and does not interfere with normal data taking procedures.

The final focus optics and the spent beam extraction optics causes additional spin rotation from the interaction point to the location of the polarization analyzer. The degree of spin rotation after the interaction is dependent on the beam energy as well as the final focus design, not yet fixed. To compensate for this variable, the Møller polarimeter contains a bend magnet to bring the spin to longitudinal orientation at the Møller target. After the target a second bend magnet (a compensator) restores the beam to its initial direction to the dump. The field strengths in the rotator-compensator pair can be varied up to 2.3 Tesla-meters, sufficient to rotate the spin orientation up to 90^o. The use of

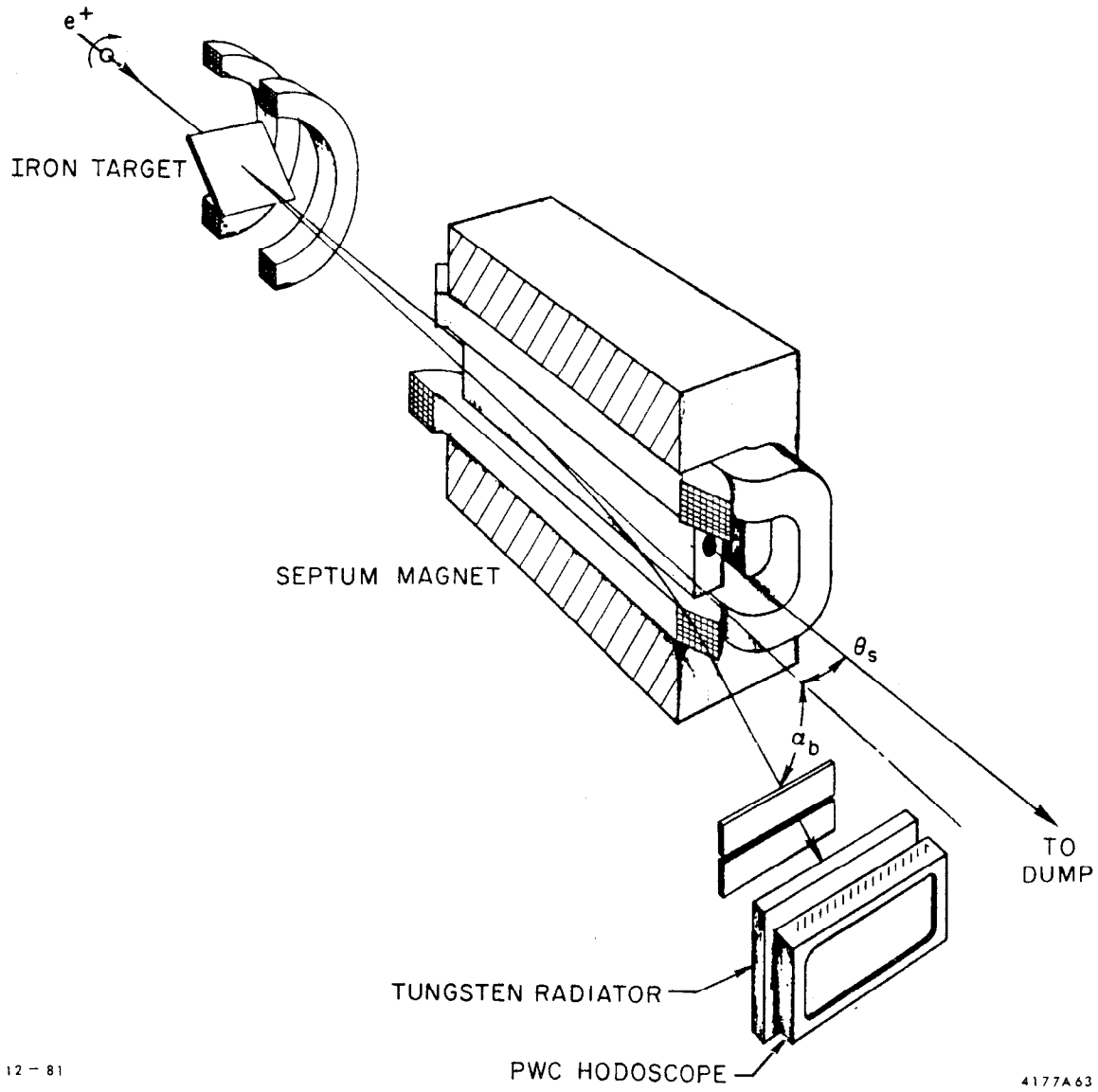

Fig. 3. A Møller spectrometer (not to scale) used in earlier experiments. The iron target is magnetized by biasing coils. Unscattered beam pass through a septum in a dipole magnet. Scattered electrons are dispersed vertically by the magnet, and detected in a hodoscope.

the rotator-compensator magnets allows polarization measurements to be made over a range of energies expected for the SLC. Figures 4 and 5 show two views of the beam dump and beam extraction optics, with the Møller spectrometer and spin compensation magnets located before the dump.

B. The Compton Polarimeter[2]

The polarimeter technique described here uses Compton scattering of circularly polarized laser light. Unlike the SPEAR, PEP and PETRA cases, where the beams are transversely polarized, the SLC beam polarization will be longitudinal and the technique used will be in some ways different. The spin motion goes through many cycles before the collision point and it is highly desirable to make the polarization measurement as close to the interaction point as possible. At such a suitable point a non-interactive measurement of the polarization can in principle be made by utilizing the spin dependence of Compton scattering. Circularly polarized laser light incident upon longitudinally polarized electrons results in different cross sections for right and left circular polarization. The backscattered gamma rays have energies comparable to beam energies due to the Lorentz transformation and the detection problem is a relatively straightforward one of detecting high energy gamma rays.

A discussion of the Compton cross section details may be found in the report of Prescott. The spin dependence of the cross section can be determined by comparing the rates of backscattered photons for right and left laser circular polarization. It is just as viable and even preferable to measure the total energy of the backscattered photons. Energy measurements do not have a rate limited by the 180 Hz SLC repetition rate since many scattered photon per pulse may be accepted into the detector provided only that the detector energy response is linear over the required range. The analyzing power is also somewhat higher for the energy measurement case compared to rate measurements.

The cross section per unit energy for the Compton scattered photons integrated over azimuth ϕ is:

$$\frac{d\sigma}{d\rho} = \frac{d\sigma_0}{d\rho} \pm P_e \, P_\gamma \frac{d\sigma_1}{d\rho}$$

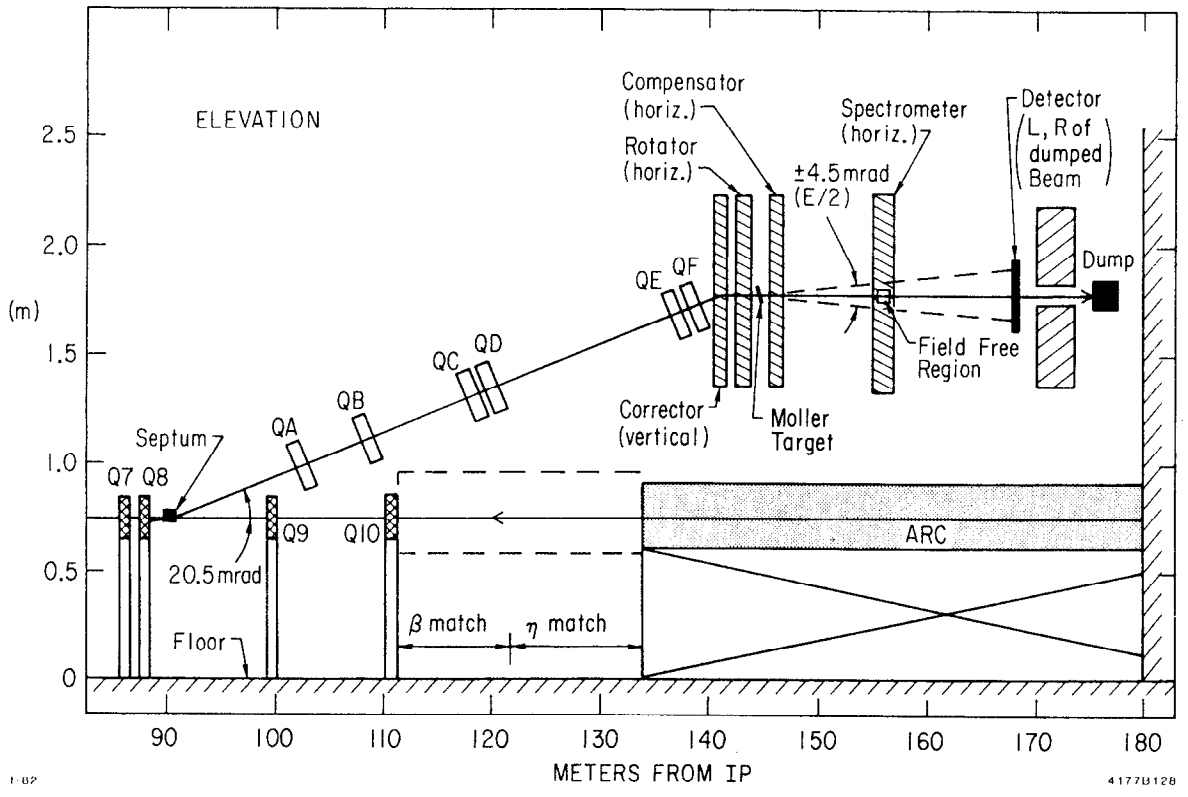

Fig. 4. Elevation view of the beam extraction transport line, beam dump, and Møller polarimeter with its spin compensation magnets.

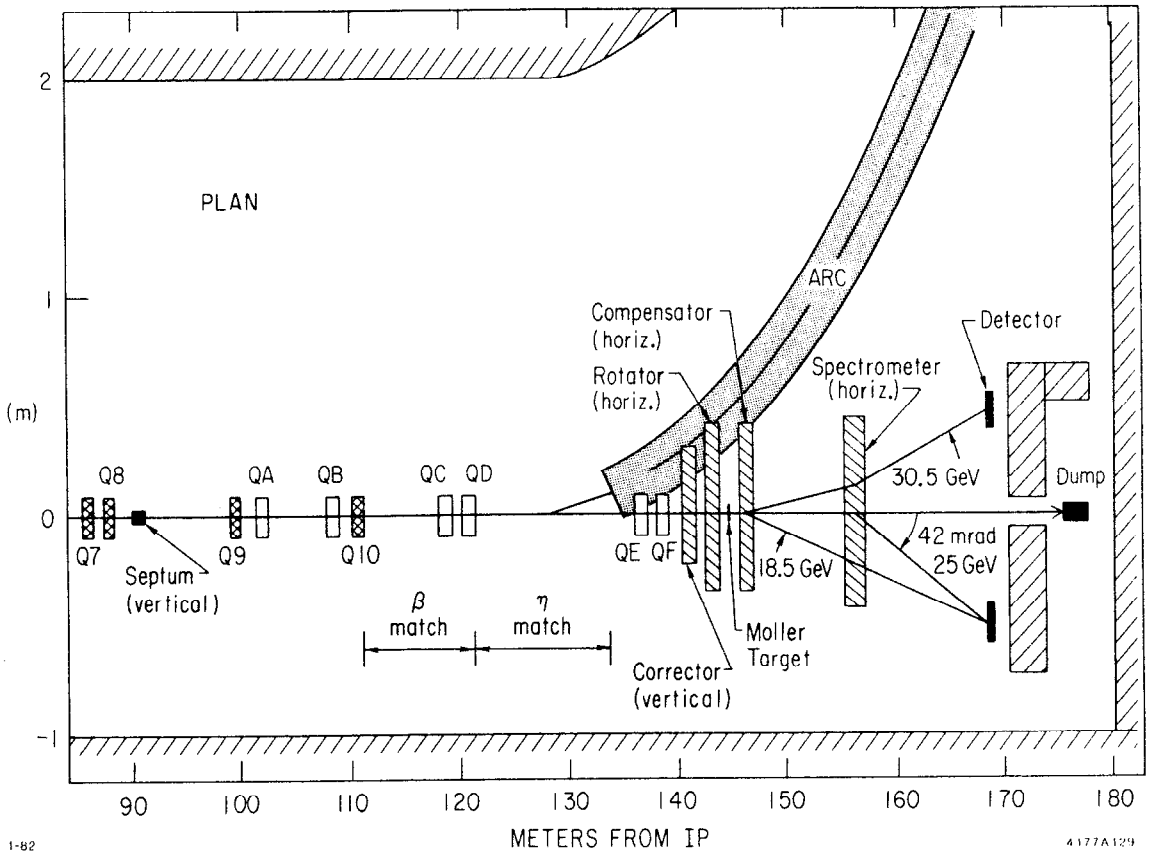

Fig. 5. Plan view of the beam extraction transport line, beam dump, and Møller polarimeter with its spin compensation magnets.

where $\rho \equiv k/k_{max}$, k = scattered photon energy and k_{max} = maximum scattered photon energy; P_e = electron longitudinal polarization and P_γ = photon circular polarization.

The differential and integral cross sections as well as the number and energy asymmetry are tabulated in Table I for the case of a beam energy E_0 = 50 GeV and a photon energy of ε_γ = 2.34 eV. The essential point to note is that a detector with the energy threshold set to accept $0.5 \leq \rho \leq 1.0$ has an effective analyzing power for energy measurements of ~30% and an average cross section of ~150 mb. The scattered photon energies range from 16 GeV to 32 GeV as indicated in Table I.

The location of the interaction point of the laser beam with the SLC electron bunch is dictated by two main requirements. First, the polarization of the beam must be measured close enough to the detector IR point so that the polarization has not been rotated by bends any significant amount. Secondly, the interaction point must be chosen at a point where the backgrounds are low enough so that the measurement can be made.

The SLC beam line will have low field bend magnets centered at Z = 16.9 meters and in all the focussing schemes, there are additional bends for vertical plane deflection. For the superconducting quadrupole case for example there is a 1.29^o bend at Z = 30 meters. The large angle bends have excessive spin rotation and it is necessary to choose a location closer to the IR point. The 1.29^o bend for example corresponds to a spin rotation angle of 146^o. The low field bends on the other hand in one version have been chosen to be 254 gauss and 18 meters in length. This corresponds to a bend angle of 2.75 mr and a spin rotation angle of 18^o for a 50 GeV beam. The interaction point must also be chosen so that it is decoupled from the hard bends and probably also the strong IR quadrupoles. The synchrotron radiation from the soft bend noted above is characterized by a critical energy of 42 KeV while the hard bends have ~1 MeV and the quadrupoles have ~2 KeV. The polarization detector backgrounds must be limited to ≤10 GeV per bunch passage for the detector to work and this can be achieved with synchrotron radiation backgrounds from the soft bends but not the hard bends and probably not the quardupoles. Another significant point is that the disrupted beam also produces too much background for a Compton detector. The disrupted beam radiates

Table I

COMPTON Scattering Parameters
E_0 = 50 GeV ε_γ = 2.34 eV

ρ	θ (mr)	k (GeV)	$\int_\rho^1 \frac{d\sigma_0}{d\rho} d\rho$ (mb)	$\int_\rho^1 \frac{d\sigma_1}{d\rho} d\rho$ (mb)	$\frac{\int_\rho^1 d\sigma_1/d\rho \, d\rho}{\int_\rho^1 d\sigma_0/d\rho \, d\rho}$	$\frac{\int_\rho^1 \rho d\sigma_1/d\rho \, d\rho}{\int_\rho^1 \rho d\sigma_0/d\rho \, d\rho}$
0	--	--	299.1	9.24	0.031	0.167
0.1	0.0512	3.21	264.7	10.35	0.039	0.169
0.2	0.0342	6.42	232.8	13.52	0.058	0.178
0.3	0.0261	9.63	203.4	18.43	0.091	0.196
0.4	0.0209	12.8	176.3	24.60	0.140	0.227
0.5	0.0171	16.1	151.0	31.33	0.207	0.274
0.6	0.0139	19.3	103.1	37.52	0.295	0.341
0.7	0.0118	22.5	103.1	41.47	0.402	0.428
0.8	0.0085	25.7	77.1	40.38	0.524	0.535
0.9	0.0057	28.9	45.3	29.46	0.651	0.653
1.0	0	32.1				

approximately 0.03% of the beam energy into a disruption cone of 2.5 mr for the superconducting quadrupole case. The disrupted beam angular cone is approximately the same as the soft bend angle and consequently the disrupted beam cannot be decoupled from the polarimeter detector by the soft bends. These disrupted beam backgrounds turn out to be much too large for the polarimeter and consequently measurements must be made on the electron beam with the positron beam either absent or separated at the IR collision point. It should also be noted that it is not possible to "escape" the disrupted beam by having the laser beam interaction upstream of the IR point since the backscattered photons (which are heading downstream) will always arrive in time with the backgrounds from the disrupted bunch.

With the above considerations in mind, a proposed location for the laser interaction point is near the end of the downstream low field bend magnet which is located approximately 16 meters from the collider IR point. The downstream rather than the upstream low field bend is proposed to avoid having to transport either the laser beam or the backscattered photon beam through the experimental detector in the IR hall. The center of the low bend provides suitable decoupling from the IR strong quadrupoles since their synchrotron radiation has a divergence characteristic of the undisrupted beam.

The synchrotron radiation from the low field bend specified as B = 254 gauss (for 50 GeV, a deflection of 2.7 mr in 18 meters) gives a synchrotron radiation spectrum with a critical energy of 42 kilovolts and radiation of $\sim 8 \times 10^{-4}$ MeV/meter per electron. The electron beam divergence at 8 meters is approximately 0.2 mr for both horizontal and vertical, and therefore about 0.1 the length of the low field bend will be seen by the Compton detector. Thus assuming that 1.8 meters of the low field bend is seen by the detector and that a SLC bunch contains 5×10^{10} electrons, we find 7.3×10^{7} MeV/bunch from the low field synchrotron radiation. If we assume that the Compton detector can tolerate 10 GeV per bunch then an attenuation of 10^{4} of the synchrotron spectrum is required. This case is very similar to the PEP polarimeter and can be achieved with an absorber in the backscattered beam line of approximately one radiation length of tungsten. Figure 6 shows schematically the proposed location of the laser interaction point.

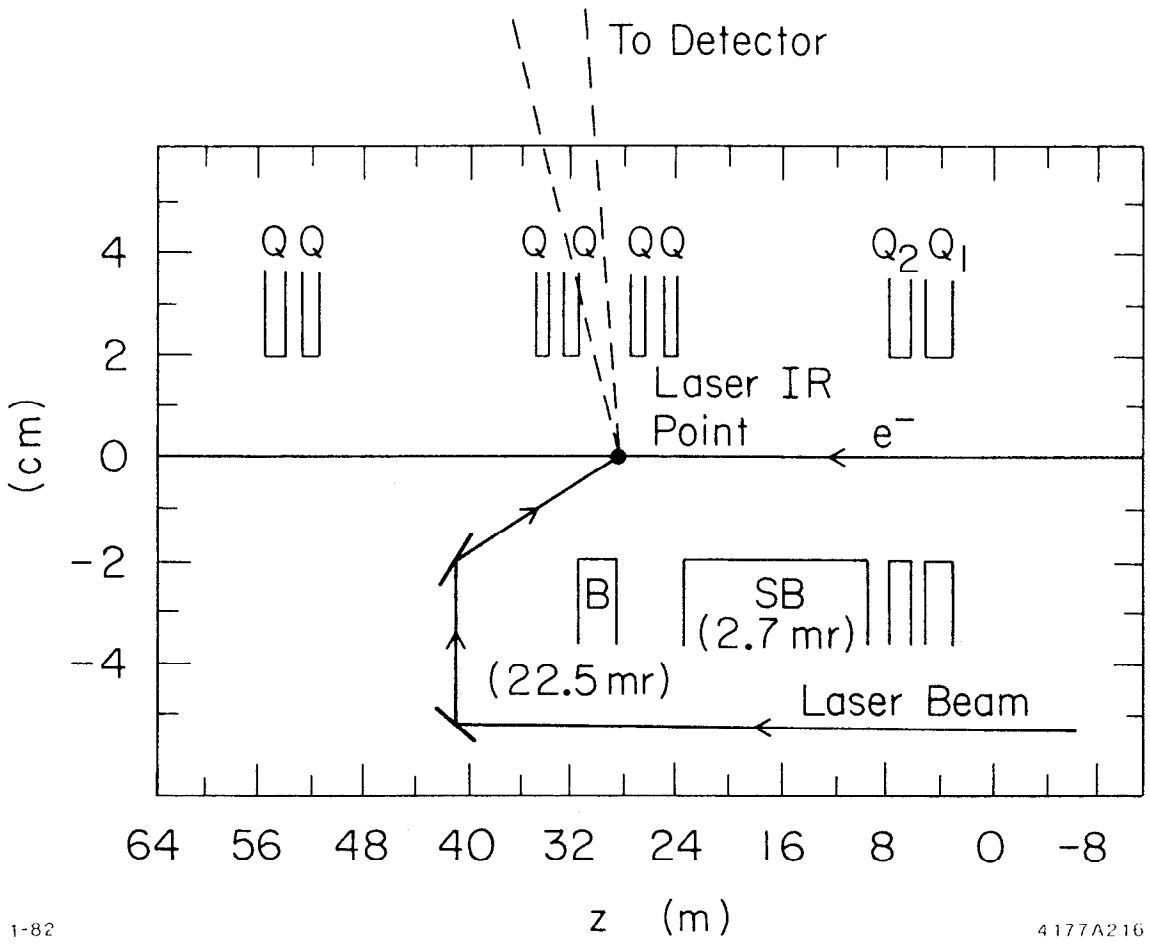

Fig. 6. Layout of beam near the interaction region, showing the laser interaction point. The laser crossing point lies outside the soft bend, near the edge of the first strong bend B to simplify extraction of the backscattered beam. In this position the backscattered photons will have to pass through some part of the quadrupole.

For a horizontal crossing angle the luminosity is given by the expression

$$\mathscr{L} = \frac{2P\ i_b}{\sqrt{2\pi}\ c\ e^2\ \varepsilon_\gamma\ \delta\ \sigma_y}$$

where

P = laser power

i_b = e beam current

ε_γ = laser photon energy in eV

δ = crossing angle

σ_y = vertical e beam size

This expression assumes that the laser has been focussed to a spot size smaller than the vertical e beam height. The beam size at the center of the low field bend is assumed to be $\sigma_y \simeq 0.5$ mm and $\sigma_x \simeq 1.4$ mm. For a crossing angle of $\delta = 2.5$ mr, and $\varepsilon_\gamma = 2.34$ eV

$$\mathscr{L} = 2.6 \times 10^{27}\ \frac{\text{cm}^{-2}\ -\ \text{sec}^{-1}}{\text{watt}\ -\ \text{mA}}$$

The scattered rate is $N = \mathscr{L}\sigma_{comp}$ x[transmission factor]. The transmission factor is determined by absorbers in the backscattered line and will be assumed to be 0.7. With an SLC bunch intensity of 5×10^{10} e/bunch and a 180 Hz repetition rate, the scattered rate is 100 Hz per kilowatt of laser power. It has also been assumed that the full Compton energy spectrum corresponding to $\sigma_{comp} = 300$ mb at 50 GeV is accepted by the detector. This yields an analyzing power of ~17% for total energy measurements.

A 10 kilowatt laser at $\varepsilon_\gamma = 2.34$ eV yields a scattering rate of 1120 Hz which will yield a measurement of the beam polarization to ±0.01 in approximately 5 minutes of running.

The type of laser that has been used for SLAC electron gun studies would be suitable for the polarimeter. This photon source is a Nd:YAG laser which yields 1 Mwatt peak power at 1.17 eV. When frequency doubled to $\varepsilon_\gamma = 2.34$ eV with 1% efficiency, it should be possible to obtain 10 Kwatt pulses 10-20 nsec long at 90-180 Hz repetition rate.

The laser light would be transported from the IR building to the interaction point in an air-filled beam pipe. The optical components in this beam line would comprise several dielectric mirrors and a remotely positioned lens for focussing the laser beam on the electron beam and for providing fine steering adjustment for both horizontal and vertical positions at the interaction point. Circular polarization is provided by a Pockels cell preceded by a linear polarizer. The length of this beam line will probably be 25-50 meters, but this has presented no particular problems for the PEP polarimeter.

There will have to be a special vacuum chamber to allow entry of the laser beam through a quartz window and a suitable chamber modification to permit extraction of the backscattered beam.

The scattered gamma rays range from 16-32 GeV for the conditions described in the previous section. The Compton angular distribution is contained in a cone of approximately $\sim 1/\gamma$ so the determining factor for the size of the scattered cone is the much larger angular extent of the electron beam at the interaction point. The beam angular size at the interaction point is ~0.2 mr so that for a 50 meter path the detector size need only be several centimeters. A lead glass total absorption detector is suitable. It may be desirable to have a gamma-ray converter in front followed by several thin trigger counters if an additional reduction of randoms from synchrotron radiation is required.

IV. PHYSICS WITH POLARIZED BEAMS

A. Charge Asymmetry and Longitudinal Asymmetry Measurements[3,4]

Charge asymmetries are enhanced by the ability to polarize the Z^o with polarized beams. We now consider the advantages of polarized beams for studying muon pair final states. These conclusions apply also to tau-pairs and could possibly be generalized to heavy quark-pairs.

The standard model of weak interactions includes the following left-handed fermion doublets:

$$\begin{vmatrix} \nu_e \\ e \end{vmatrix}_L \quad \begin{vmatrix} \nu_\mu \\ \mu \end{vmatrix}_L \quad \begin{vmatrix} \nu_\tau \\ \tau \end{vmatrix}_L \quad \begin{vmatrix} u \\ d \end{vmatrix}_L \quad \begin{vmatrix} c \\ s \end{vmatrix}_L \quad \begin{vmatrix} t \\ b \end{vmatrix}_L \qquad \begin{matrix} T_3 = +1/2 \\ T_3 = -1/2 \end{matrix}$$

And the following right-handed singlets:

$$e_R \quad \mu_R \quad \tau_R \quad u_R \quad d_R \quad c_R \quad s_R \quad t_R \qquad T_3 = 0$$

The neutral weak couplings of these fermions are given by the formulae:

$$\begin{aligned} g_L &= T_{3_L} - Q \sin^2\theta_w \\ g_R &= T_{3_R} - Q \sin^2\theta_w \quad , \end{aligned} \tag{7}$$

where T_3 is the weak isospin projection, Q is the fermion charge and $\sin^2\theta_w$ is the weak mixing parameter.

A more conventional representation of the coupling is in terms of the vector and axial vector coupling given by:

$$\begin{aligned} v &= (g_R + g_L)/2 \\ a &= (g_R - g_L)/2 \end{aligned} \tag{8}$$

These are evaluated in Table II using the best present determination of the weak mixing parameter — $\sin^2\theta_w = 0.23 \pm 0.009$.[5]

A polarized beam of electrons will allow direct control of the weak isospin projection. The strength of the weak interaction can therefore be significantly varied by changing the electron polarization. It is this aspect of the measurement we will concentrate on when we discuss

Table II

Vector and Axial-Vector Couplings in the Standard Model
Multiplied by 4

Fermion	4 * a Axial Vector	4 * v Vector
ν	-1	+1
e,μ,τ	+1.0	$-1.0 + 4 \sin^2\theta_w = -.08$
u,c,t	-1.0	$1.0 - 8/3 \sin^2\theta_w = .39$
d,s,b,	+1.0	$-1.0 + 4/3 \sin^2\theta_w = -.69$

asymmetry measurements. Many of the experimental aspects of Z^o physics will be dominated by the small value of the leptonic vector coupling, v_e.

The charge asymmetry is defined to be

$$A_{ch}(\theta) \equiv \frac{d\sigma/d\Omega(\theta)_{\mu^-} - d\sigma/d\Omega(\theta)_{\mu^+}}{d\sigma/d\Omega(\theta)_{\mu^-} + d\sigma/d\Omega(\theta)_{\mu^+}} \tag{9}$$

For a two particle final state the charge asymmetry is identical to the forward-backward asymmetry.

$$A_{CH} = A_{FB} \equiv \frac{d\sigma/d\Omega(\theta) - d\sigma/d\Omega(\pi - \theta)}{d\sigma/d\Omega(\theta) + d\sigma/d\Omega(\pi - \theta)} \Bigg|_{\mu^-} \tag{10}$$

If we evaluate this expression on the Z^o we can write it as

$$A_{CH} = \frac{2\cos\theta}{1 + \cos^2\theta} \left(\frac{2 v_f a_f}{v_f^2 + a_f^2} \right) \left[\frac{\frac{2 v_e a_e}{v_e^2 + a_e^2} + P_e}{1 + P_e \frac{2 v_e a_e}{v_e^2 + a_e^2}} \right] \tag{11}$$

This is written for the case where the electron beam is polarized (P_e) and the positron beam unpolarized. We can rewrite this form as

$$A_{CH} = P_f \left[\frac{P(Z^o) + P_e}{1 + P_e P(Z^o)} \right] f(\theta) \tag{12}$$

where $P_f = 2 v_f a_f / v_f^2 + a_f^2$ is the natural polarization of a fermion f coming from unpolarized Z^o's due to the inequality $g_L \neq g_R$, $P(Z^o) = 2 v_e a_e / v_e^2 + a_e^2$ is the polarization of the Z^o for unpolarized beams, and $f(\theta) = 2 \cos\theta / 1 + \cos^2\theta$ is the angular dependence. If both beams were unpolarized, a measurement of this asymmetry would determine the quantity

$$P_f = \frac{2 v_f/a_f}{1 + (v_f/a_f)^2} \quad ,$$

and hence the ratio v_f/a_f, assuming the electron parameters v_e/a_e are known. In practice this asymmetry is made more difficult to measure by the small value of v_e. Polarized beams can help in this asymmetry measurement because they increase the size of the second term (in the bracket). Figure 7 shows A_{CH} integrated over all θ for unpolarized and longitudinally polarized electron beams. Figure 8 indicates the statistical precision obtained with a $30 pb^{-1}$ measurement spanning the Z^o peak with unpolarized beams. An indication of the sensitivity to $\sin^2\theta_w$ is shown by the calculated asymmetries with $\sin^2\theta_w = 0.20$, 0.23, and 0.25.

With a polarized beam the variation in the cross section with spin flip of the beam can be measured. We define the longitudinal asymmetry as

$$A_L(\theta) = \frac{d\sigma/d\Omega(\theta, P_e = +) - d\sigma/d\Omega(\theta, P_e = -)}{d\sigma/d\Omega(\theta, P_e = +) + d\sigma/d\Omega(\theta, P_e = -)} \qquad (13)$$

where θ is direction of μ^- with respect to the initial electron beam. This can be evaluated at the Z^o peak to give

$$A_L(\theta) = P_e \frac{\left[\frac{2 v_e/a_e}{1 + (v_e/a_e)^2}\right](1 + \cos^2\theta) + \left[\frac{2 v_f/a_f}{1 + (v_f/a_f)^2}\right] 2\cos\theta}{(1 + \cos^2\theta) + \left[\frac{2 v_e/a_e}{1 + (v_e/a_e)^2}\right]\left[\frac{2 v_f/a_f}{1 + (v_f/a_f)^2}\right] 2\cos\theta} \qquad (14)$$

If one integrates over any interval symmetric about 90^o, the asymmetry depends only on the electron couplings:

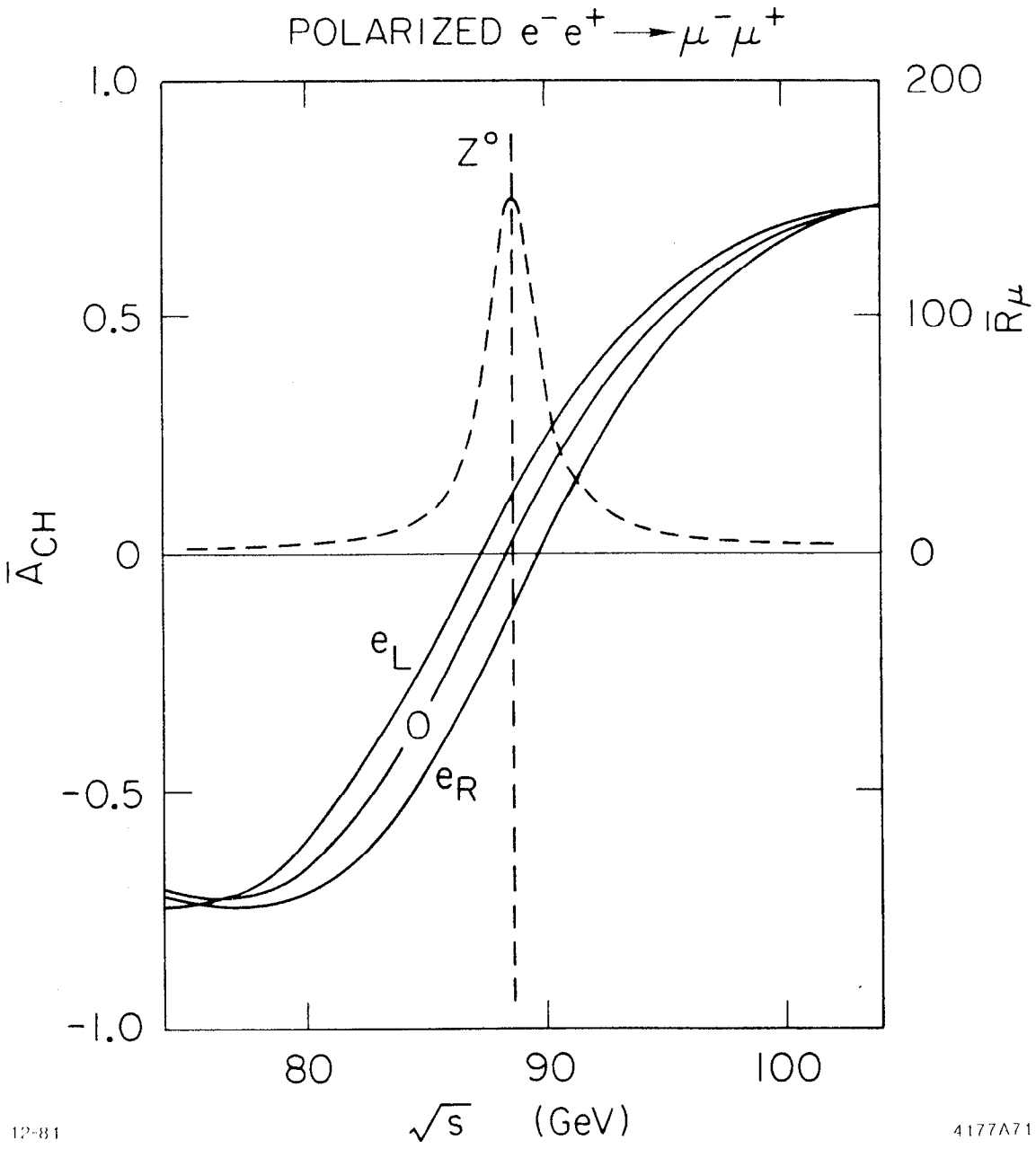

Fig. 7. The charge asymmetry versus C.M.S. energy $\sqrt{s}$ is shown for polarized and unpolarized beams, according to the predictions of the standard model, for $\sin^2\theta_W = .23$. The ratio $R_\mu = \sigma(\mu^-\mu^+)/\sigma_{pt}$ is also shown with the position of the Z^o peak indicated by the dashed line. Radiative corrections are not included.

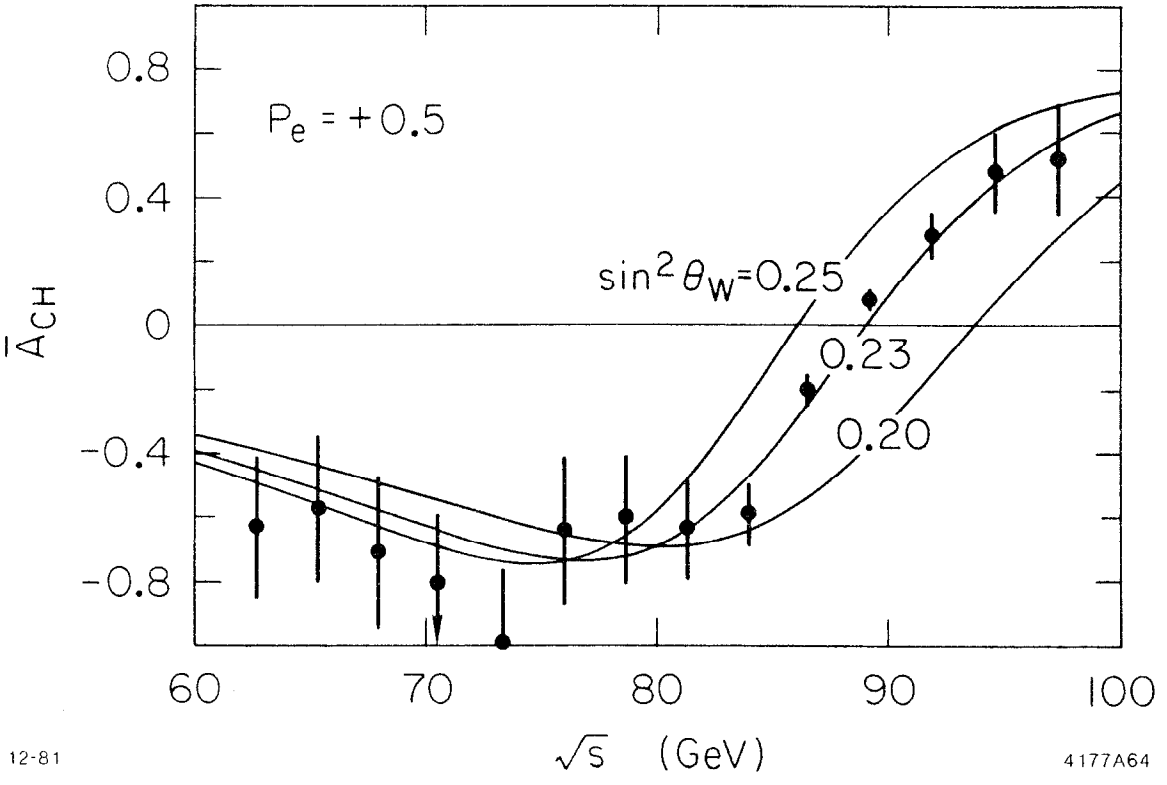

Fig. 8. The charge asymmetry averaged over solid angle for unpolarized beams, for $\sin^2\theta_w$ = .20, .23 and .25. The points and statistical errors correspond to a hypothetical run with an exposure of 2 pb^{-1} per point.

$$\bar{A}_L = P_e \left[\frac{2\, v_e/a_e}{1 + (v_e/a_e)^2} \right] \tag{15}$$

This is just the variation in the total cross section with electron spin flip. That is, it is the variation in Z^o production with spin flip. It has been pointed out that this total cross section longitudinal asymmetry, which can be up to 16%, may be the best measure of v_e/a_e for the electron.[6]

The energy dependence near the peak is shown in Fig. 9, for A_L integrated only over the forward hemisphere. Notice that it shows little variation with energy at the Z^o peak.

1. Statistical Errors

From the definition of the charge asymmetry we can rewrite

$$A_{CH} = \frac{N^- - N^+}{N^- + N^+} \tag{16}$$

Where N^+ is the number of positive muons, and N^- is the number of negative muons in the forward hemisphere.

For small asymmetries the error is dominated by the numerator and we can write

$$\Delta A_{CH} \cong \frac{1}{\sqrt{N^+ + N^-}} \tag{17}$$

In a similar fashion we can write for the longitudinal asymmetry

$$\Delta A_L = \frac{1}{\sqrt{M^+ + M^-}} \tag{18}$$

Now M^+ is the number of negative muons in the <u>forward</u> hemisphere for positive electron polarization and M^- the number of negative muons in the forward hemisphere for negative electron polarization.

Close examination of Eq. (14) shows that $A_L(\theta)$ is largest in the forward direction, and smallest in the backward direction. Measurements of $\bar{A}_L$ are optimized by integrating over a forward cone which is close to 90^o opening angle. Therefore, the discussion of errors on $\bar{A}_L$, which follows, has taken the forward hemisphere as the optimum solid angle.

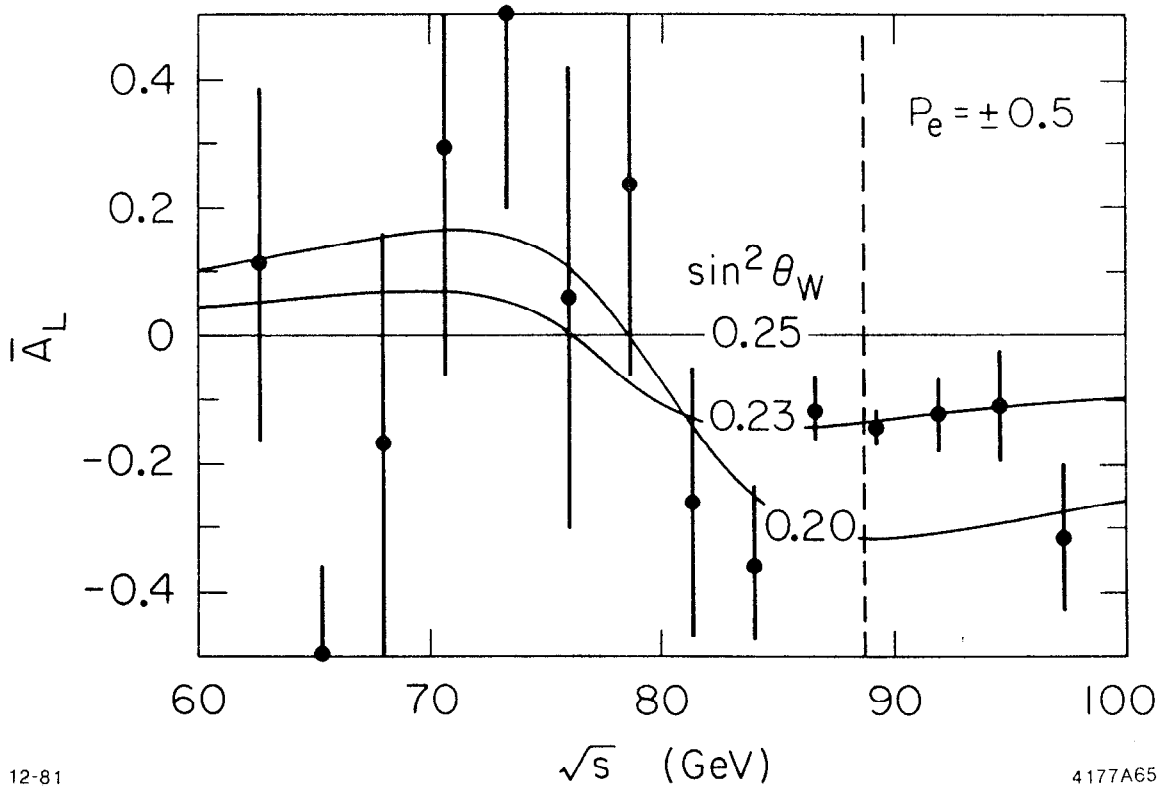

Fig. 9. The longitudinal asymmetry averaged over 4π solid angle for $\mu^-\mu^+$ final states and beam polarization 50%, for $\sin^2\theta_W$ = .20, .23, and .25. The points and errors correspond to a hypothetical run with an exposure of 2 pb^{-1} per point.

The error in the determination of the model parameters will be directly related to the error in the asymmetry. So we will write quite generally

$$\Delta \sin^2\theta_w = \frac{K}{\sqrt{N^+ + N^-}}$$
$$\Delta (v_\mu/a_\mu) = \frac{K'}{\sqrt{N^+ + N^-}} \qquad (19)$$

The values of K and K' will be different for measurements of A_{CH} or A_L, of course. There are four coefficients to consider, K_{CH}, K'_{CH}, K_L, and K'_L.

In the standard model $\sin^2\theta_w$ is the only parameter. It enters in both v_e/a_e and v_μ/a_μ. The measured asymmetries depend on both of these ratios of couplings. A measurement of A_{CH} and A_L will determine $\sin^2\theta_w$ and its associated error indicated by Eq. (19). However, the important measurement is not simply a determination of $\sin^2\theta_w$ but rather a measurement of each coupling (v_μ/a_μ). This is a test of the universality that is implied in the standard model. We therefore also consider the measurement error in extracting v_μ/a_μ, assuming that v_e/a_e is known from the interferences near the Z^o peak or from the spin flip asymmetry of the total cross section. These errors are given in Eq. (19).

Using Eqs. (11) and (14) the constants K and K' can be easily calculated. Assume that the SLC is running with 50% electron polarization and an equal number of left- and right-handed runs (+ and - polarization). The statistical errors for a particular polarization will reflect this mix of runs, since the precision one can obtain with -0.5 polarization is somewhat higher than with 0.5 polarization.

The following comparisons for polarized beam running are notable:

	K_{CH}	K'_{CH}
$P_e = -0.5$	0.233	1.10
$P_e = 0.0$	0.481	4.22
Increase in sensitivity with polarized beam	4.26	14.72

Thus for a measurement of the final state ratio (v_μ/a_μ), a polarized beam of 50% polarization is worth a factor of ~10 in unpolarized luminosity.

Tables III and IV give values of these parameters for a wider range of P_e.

Table III

$\bar{A}_{CH}$, Integrated Over Forward Hemisphere
$\sin^2\theta_w = .230$

P_e	$\bar{A}_{CH}$	K_{CH}	K'_{CH}
-1.0	.119	.171	.670
-0.5	.073	.233	1.10
0.0	.019	.481	4.22
0.5	-.044	.899	1.81
1.0	-.119	.172	.671

Table IV

$\bar{A}_L$, Integrated Over Forward Hemisphere
$\sin^2\theta_w = .230$

P_e	$A_L(2\pi)$	K_L	K'_L
±1.0	-.271	.079	.717
±0.5	-.136	.158	1.45
±0.0	0	--	--

Of course, without polarization A_L cannot even be measured. It is A_L that may prove to be the important measure since it is less sensitive to background effects, detector asymmetries, radiative corrections, and energy variations near the Z^o. As will be seen in the next section, A_L measurements will also give somewhat greater sensitivity to model parameters.

Using the cannonical 10^6 Z^o's produced at the SLC in the first year and taking a 3% branching ratio of $Z^o \to \mu^+\mu^-$, we obtain

$$\Delta \sin^2\theta_w = 0.0058*K$$

$$\Delta (v_\mu/a_\mu) = 0.0058*K'$$

If we now insert the average K and K' values at 50% polarization, equally split between $+P_e$ and $-P_e$, we obtain the following statistical limits in the parameter errors:

(i) From A_{CH} measurements:

$$\Delta \sin^2\theta_w \geq .0019$$

$$\Delta (v_\mu/a_\mu) \geq .008$$

(ii) From A_L measurements:

$$\Delta \sin^2\theta_w \geq .0009$$

$$\Delta (v_\mu/a_\mu) \geq .008$$

2. Beam Polarization Error in A_L

Since the longitudinal asymmetry is directly proportional to the beam polarization we can ask how much an error in the measurement of the polarization itself contributes to A_L and therefore to $\Delta \sin^2\theta_w$. It is clear from the Eq. (14) that the percentage error in the polarization must not exceed that required for $\Delta \sin^2\theta_w$ and $\Delta (v_\mu/a_\mu)$. Therefore, an error of .0002 in $\sin^2\theta_w$ requires at least a 1% absolute determination of P_e if $P_e = 0.5$. This is close to the limit of accuracy of a polarimeter and may be the limiting parameter for an A_L measurement.

3. Solid Angle Considerations

All of the proceeding calculations assumed that the muon detector measuring the asymmetries had 4π solid angle coverage. Since the asymmetries and the production cross sections tend to be maximum in the forward direction it is important to be able to quantify the effects of forward angle cuts in detector.

The K and K' constants allow us to simply display the effects of solid angle cuts in a real detector. The value of K and K' will reflect both the reduction of observed events and the lack of sensitivity when one measures asymmetries away from 0^o.

This solid angle effect is shown in Figs. 10 and 11 for both A_{CH} and A_L measurements. The curves are shown calculated for two types of detectors: one is a central detector with acceptance for all $|\cos\theta| < |\cos\theta_{cut}|$. The other is for a purely forward detector with acceptance $|\cos\theta| > |\cos\theta_{cut}|$. The central detector gives the smallest errors, of course. However, even for a cut at 25° ($\cos\theta_{cut} = .9$) the detector would only have to run 30% longer for the same sensitivity. We would conclude then that nominal forward holes in central detectors will not appreciably compromise their ability to do asymmetry measurements.

The forward detector indicated also has some interesting properties. It compensates for the loss of events by the increased sensitivity in the forward direction. As can be seen for A_L measurements, 40° is the cross over angle of equal sensitivity (and running time) for forward and central detectors at $P_e = -0.5$.

4. Systematic Errors in Charge Asymmetries

The ability to eliminate detector biases in a measurement such as charge asymmetries is a most important aspect of polarized beam measurements. To illustrate the advantages of spin reversal, consider a detector which has unequal detection efficiencies for μ^- and μ^+. For example, a detector has a magnetic field to determine the sign of the charge, so μ^-'s and μ^+'s produced in a given direction do not track through precisely the same geometry. Edge effects, in particular, may lead to different detection efficiencies for the μ^-'s and μ^+'s. Let the efficiencies for identification be f^+ and f^- for μ^+'s and μ^-'s, respectively. These will be functions of position in the detector, and time. The experimental measurement is then

$$A_{exp} = \frac{f^-N^- - f^+N^+}{f^-N^- + f^+N^+} \tag{20}$$

Assume here f^+ and f^- are averaged over solid angle and time variations. Define $\varepsilon = 1/2(f^+ - f^-)$ and $\bar{f} = 1/2(f^+ + f^-)$. Then one finds that, for $\varepsilon \ll \bar{f}$,

$$A_{exp} \approx A_{CH}(1 + \varepsilon/\bar{f}\, A_{CH}) - \varepsilon/\bar{f} \tag{21}$$

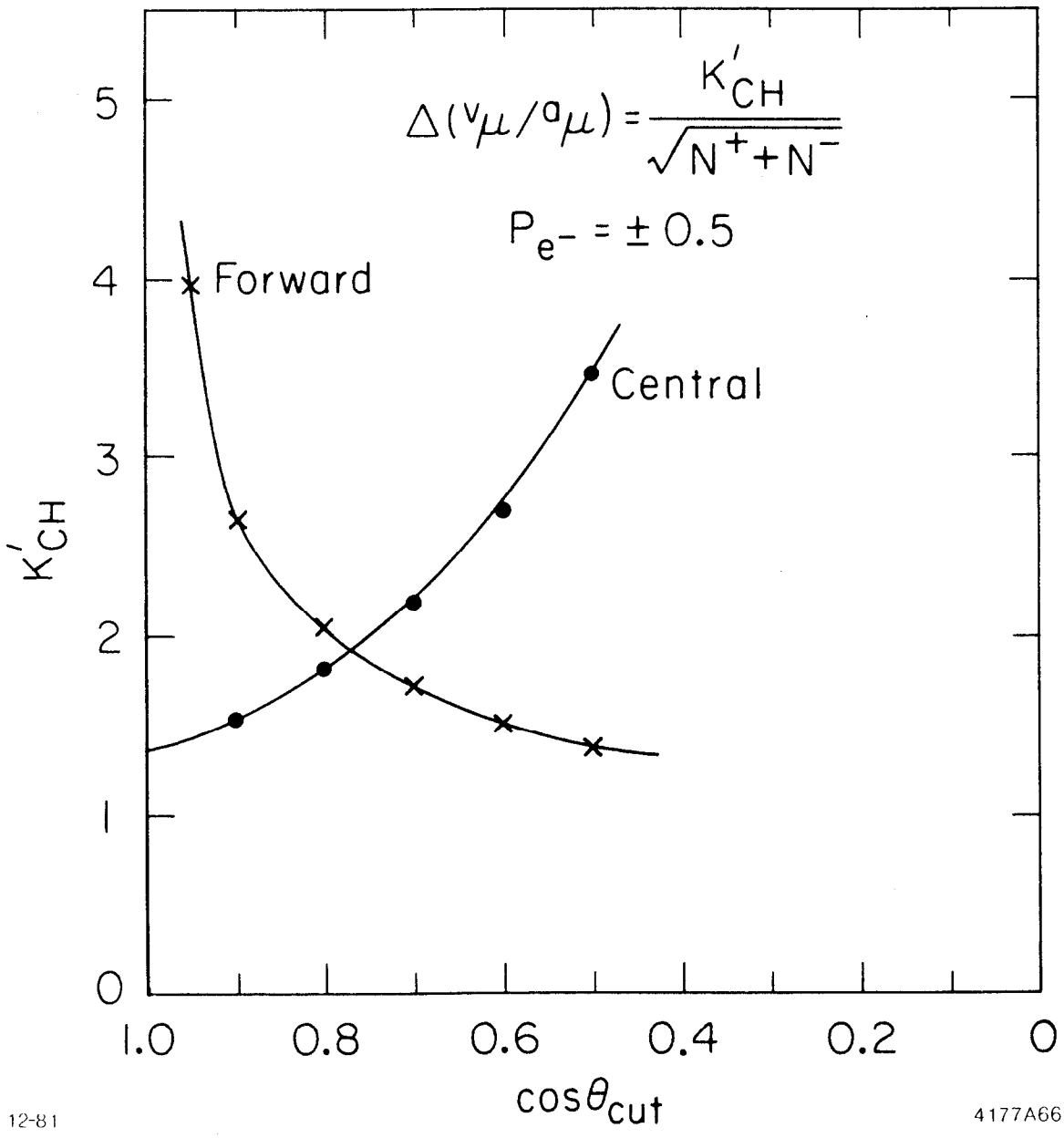

Fig. 10. The solid angle dependence for the coefficient for K'_{CH} for $P_e = -0.5$. The central detector solid angle is integrated from $-\cos\theta_{cut}$ to $+\cos\theta_{cut}$. The forward detector picks up the rest of the solid angle. Sensitivities are equal near $\theta_{cut} = 40^{o}$.

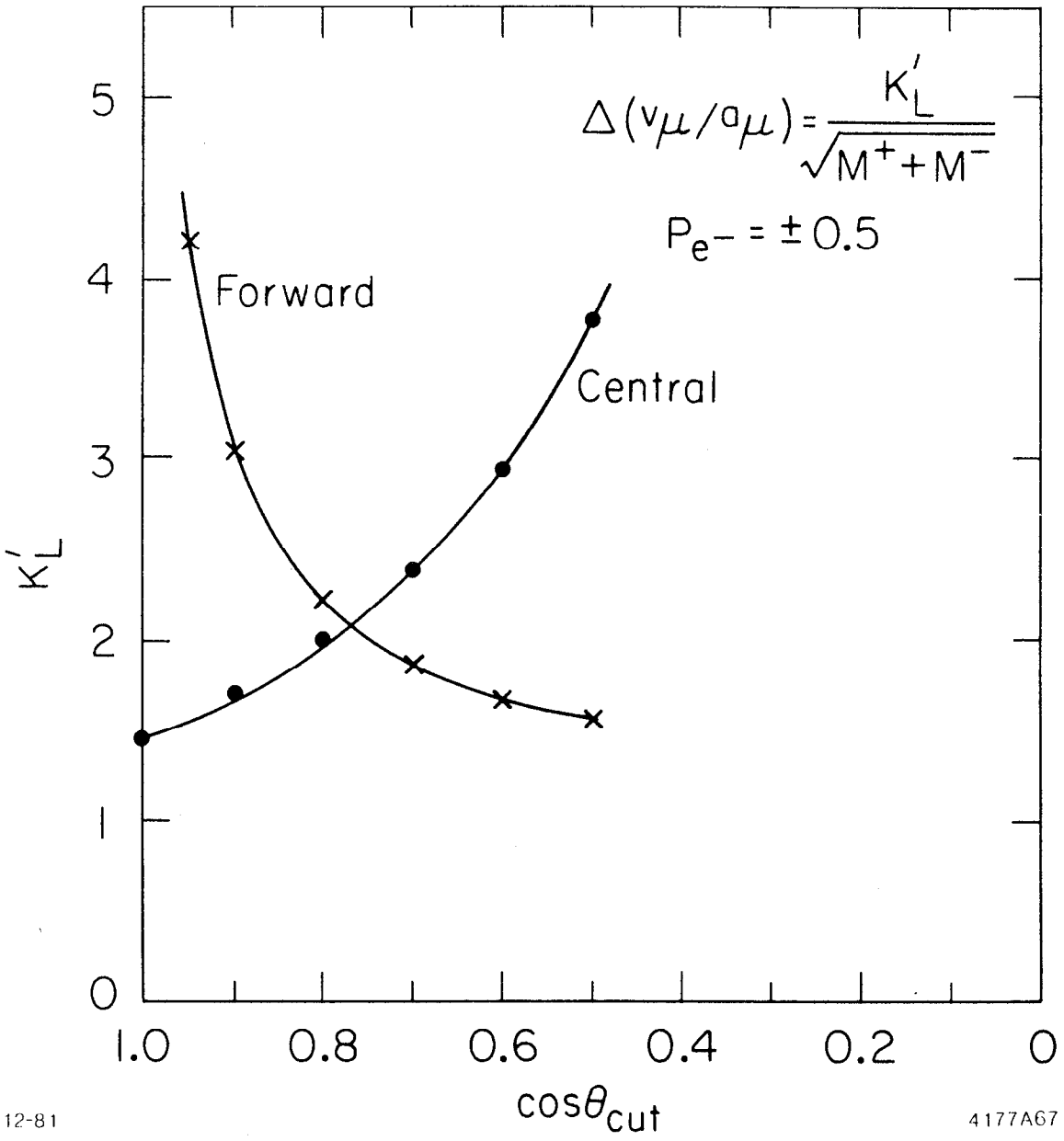

Fig. 11. The solid angle dependence for the coefficient K'_L for $P_e = \pm.50$. The central detector has solid angle coverage $|\cos\theta| < |\cos\theta_{cut}|$ and the forward detector $|\cos\theta| > |\cos\theta_{cut}|$. The detectors have equal sensitivity near $\theta_{cut} = 40^o$.

For small values of A_{CH} small differences in detection efficiencies lead to an error in A_{exp} of approximately $\varepsilon/\bar{f}$. In principle, these systematic errors in A_L can be eliminated by rotating the detector. In practice, such steps are impossible for these very large detectors.

While rotating the detector may not be practical, the detector biases can be eliminated in these polarization experiments. One approach employs flipping the spin of the polarized beam to cancel them to lowest order. Another calls for providing the capability to run the SLC with the positrons and electrons switched to opposite arms of the machine (beam swapping).[7]

In the case of spin flipping, the experimenter can simultaneously measure $A_{exp}(+P_e)$ and $A_{exp}(-P_e)$ by correlating A_{exp} with the sign of the polarization determined prior to each beam pulse by electronic signals sent from the polarized electron source. The subtracted asymmetry is

$$A_{exp}(+P_e) - A_{exp}(-P_e) \tag{22}$$

The subtracted asymmetry is independent of detector inefficiencies in lowest order. The systematic errors on $A_{exp}(+P_e) - A_{exp}(-P_e)$ will be significantly smaller than on $A_{exp}(0)$.

The capability to switch the positron and electron arms leads to the elimination of the effects of detector inefficiencies on the asymmetry measurement. This beam swapping could be done periodically (for example, every one to three months) and would be complemented by the continuous spin flipping.

An alternative way to study systematic errors on A_{CH} comes from a novel use of polarized beams.[7] By suitable selection of + helicity and - helicity beam pulses, the time-averaged polarization of the Z^o can be set to zero (see Eq. (11)). The charge asymmetry A_{CH} is for this sample necessarily zero, and the remaining non-zero value for A_{exp} can be ascribed to detector biases. Thus detector systematic errors can be measured using the beam polarization.

B. Final State Polarization of τ's[8]

In the disintegration of the Z^o the produced quarks and leptons are polarized. This net polarization results from the unequal couplings of the Z^o to right-handed fields, and is of the same character as the longitudinal asymmetry discussed earlier.

While all quarks and leptons may be polarized, only the heavy lepton τ polarization can be measured with a conventional detector. In terms of the differential cross sections, the polarization is

$$P_\tau(\theta) = \frac{n_+ \cdot [\sigma_{++}(\theta) - \sigma_{+-}(\theta)] + n_- \cdot [\sigma_{-+}(\theta) - \sigma_{--}(\theta)]}{n_+ \cdot [\sigma_{++}(\theta) + \sigma_{+-}(\theta)] + n_- \cdot [\sigma_{-+}(\theta) + \sigma_{--}(\theta)]} \qquad (23)$$

where $n_\pm = (1 \pm P_e)/2$ is the normalized flux of electrons of the indicated helicity, P_e is the beam polarization, and $\sigma_{\lambda\lambda'} \cdot (\theta)$ are the helicity dependent differential cross sections. The subscripts refer to the electron and the τ^- helicities resp. the helicities of the positive particles being constrained by these.

The value of the net polarization, arrived at by integrating the numerator and denominator of Eq. (23) over 4π sr, appears in Fig. 12 for several values of $\sin^2\theta_w$. The polarization remains large beyond the Z^o pole region due to the falling single photon annihilation contribution.

The value of $P_\tau(\theta)$ can be expressed, at the Z^o pole, neglecting the electromagnetic interaction, as

$$P_\tau(\theta) = \frac{P(\tau) + P\,\dfrac{2\cos\theta}{1+\cos^2\theta}}{1 + P(\tau)\,P\,\dfrac{2\cos\theta}{1+\cos^2\theta}} \qquad (24)$$

where $P(\tau) = 2\,v_\tau a_\tau/(v_\tau + a_\tau)$ is the intrinsic τ polarization due to the inequality $g_R(\tau) \neq g_L(\tau)$, and $P = P_e + P(Z^o)/1 + P_e\,P(Z^o)$, with $P(Z^o) = 2\,v_e a_e/(v_e^2 + a_e^2)$ being the polarization of the Z^o in the absence of external beam polarization. The overall Z^o polarization, due to both the weak effects and the beam polarization, is given by P. In Eq. (24) the term $P(\tau)$ describes the τ couplings, while the second, angle dependent, term results from angular momentum conservation and vanishes if integrated over all angles. Thus, the net polarization observed in any detector symmetric around 90^o is independent of the beam polarization and equals $P(\tau)$.

Figure 13 shows the variation of $P_\tau(45^o)$ with beam polarization for three values of $\sin^2\theta_w$. For fully polarized beams, the τ becomes highly polarized. However, the sensitivity of the τ polarization to variations

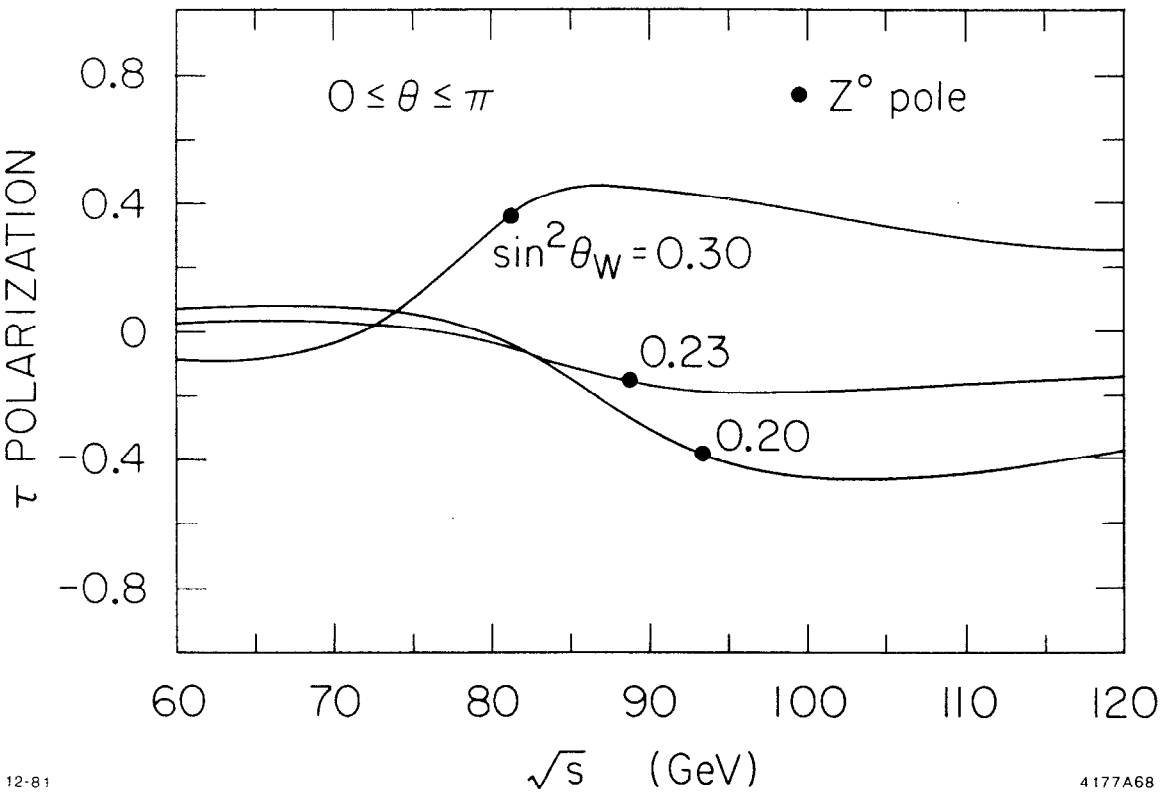

Fig. 12. The τ polarization dependence as a function of center-of-mass energy for $\sin^2\theta_w$ = .20, .23, and .30. The peak of the Z^o is indicated for each case.

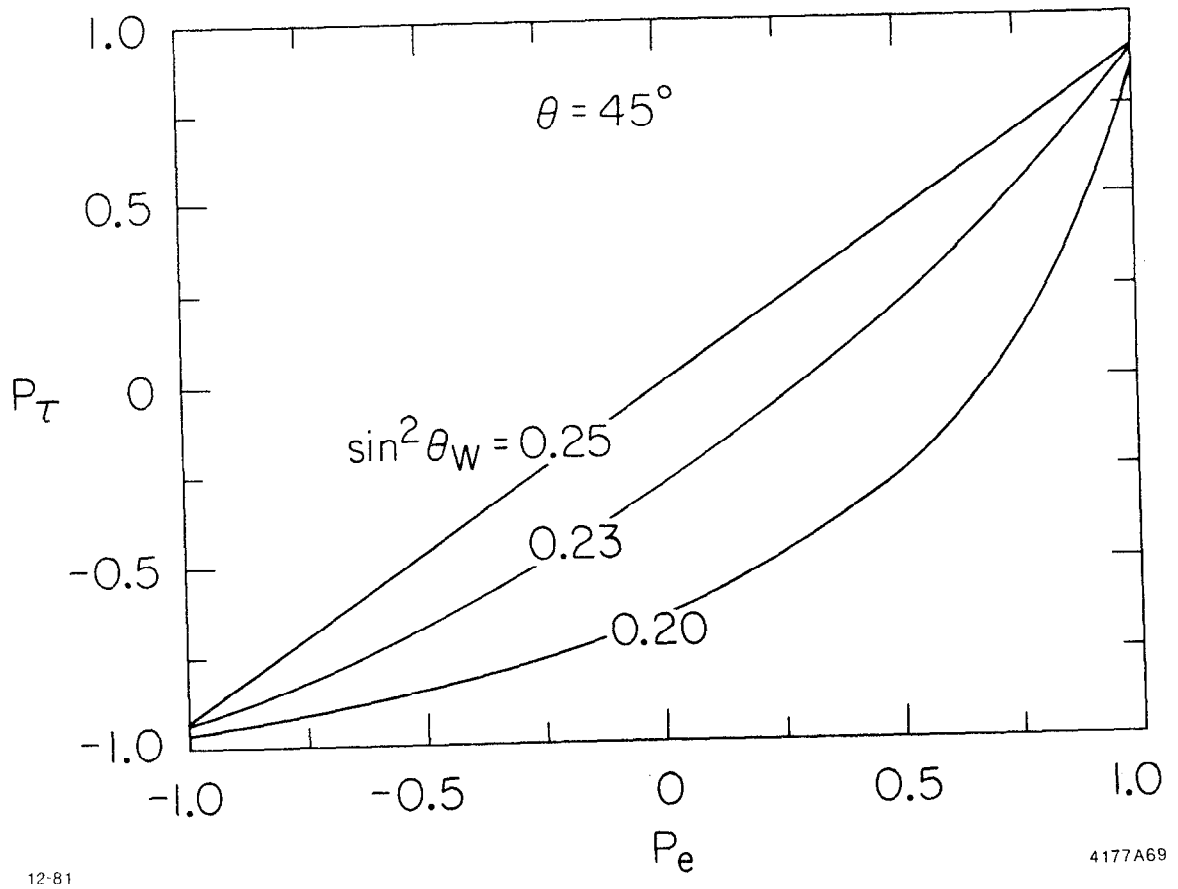

Fig. 13. The variation of τ polarization with beam polarization at $\theta = 45^o$ for $\sin^2\theta_w = .20$, .23, and .25.

of the weak coupling goes to zero in these limits. More formally, $\partial P_\tau / \partial(\sin^2\theta_w)$ becomes small at $P_e = \pm 1$, as seen in Fig. 13. Measurement of τ neutral current couplings is not significantly enhanced with polarized beams.

The beam polarization can be used in studying the charged weak current in the decay $\tau \to \rho\nu$, $\rho \to \pi\pi$, by increasing the degree of polarization of τ's. When the τ lepton decays into a spin one meson and a neutrino, the meson state with helicity opposite its charge is forbidden by angular momentum conservation if the decay is mediated by the conventional V-A current.[9] In the case of the ρ decay, the laboratory momentum distribution of pions will reflect the polarization state of the τ and establish the nature of the current in the semileptonic τ decays. Such an investigation, although possible at existing electron-positron storage rings, has not been done to date due to limited statistics and the magnitude of the effect.

The characteristic momentum distribution of pions in this decay chain could be more easily established for decays of polarized τ's, due to the alignment of the ρ and τ spins. Thus, while the pion momentum spectra in the forward ($\theta < 45^\circ$) and backward ($\theta > 135^\circ$) cones differ for unpolarized beams, as shown in Fig. 14a, the forward-backward difference becomes much more pronounced for polarized electrons as seen in Fig. 14b. These spectra have been calculated using $\sin^2\theta_w = 0.23$, a V-A charged decay current and $P_e = -0.5$. For an ideal detector with 13,000 $\tau \to \rho\nu$ events, the standard deviations of the distributions in Fig. 14b would be measured with a precision of 0.0032, while the standard deviations of the two spectra differ by 0.04 giving more than a 10σ effect. The corresponding difference for unpolarized beam (Fig. 14a) is about factor of 3 smaller.

C. Hadronic Processes[10]

Following the studies on leptonic final states, we would like to consider the strong interactions by looking at the rich but less predictable part of the problem, the hadronic final state. Again we restrict ourselves to unpolarized or single longitudinally polarized electron beams, since for unpolarized positron beams, transverse electron polarization leads to no observable effects.

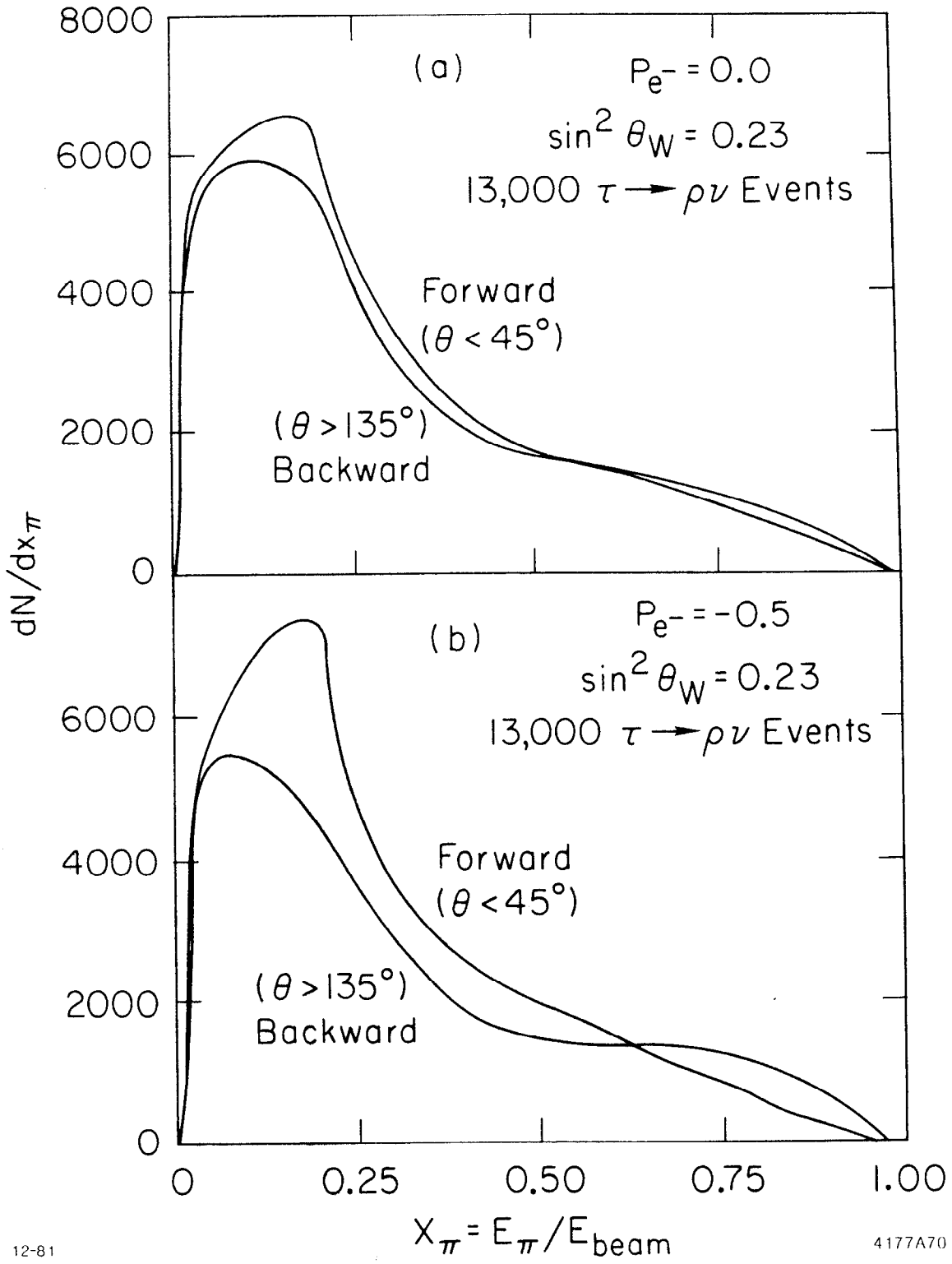

Fig. 14. The momentum spectrum for π's from the processes $\tau \rightarrow \rho\nu$; $\rho \rightarrow \pi\pi$ at the Z^0 peak for unpolarized and polarized beams. The forward-backward asymmetry is enhanced with polarized beams.

We have seen how, in the leptonic case, axial and vector coupling constants can be obtained by using information from unpolarized data and from asymmetry and polarization measurements. In principle, the same method can be applied to $e^+e^- \rightarrow q\bar{q}$ to determine the coupling constants for the different quarks. However, the fragmentation process increases the complexity of the analysis and the error on the measurements.

Asymmetry and polarization at the constituent level are large, but the fragmentation will dilute these effects.[11,12] Different observables have different behavior under the same recombination model.

Aside from the different physics obtained from the study of hadronic final states, these measurements have some advantages compared to leptonic final state experiments such as a large cross section (all hadrons/ μ pairs $\approx$ 25 at Z^o) and larger spin effects.[6] At the constituent level, asymmetries with polarized beams are larger by a considerable factor compared to leptons. However, there are problems connected to the lack of knowledge of the recombination process. They include uncertainties in how to determine the $\bar{q}$ from the q initiated jet, how to tag the initial quark flavor, and how to distinguish gluon jets from quark jets.

Consider the observables at the constituent level where they can be easily computed. Assuming zero quark masses and a null beam polarization, one gets:

$$P_L = - \frac{H_3 \ (1 + \cos^2\theta) + 2 \ H_1 \cos\theta}{2 \ G_1 \ (1 + \cos^2\theta) + 4 \ G_3 \cos\theta} \qquad (25)$$

where θ is the polar angle of the out-going quark and $H_{1,3}$, $G_{1,3}$ are structure functions dependent on the center of mass energy $\sqrt{s}$, the axial and vector coupling constants, the Z^o's masses, widths and the quark flavors. The full expressions of $H_{1,3}$, $G_{1,3}$ are given in the Ref. 13. One gets larger effects by using longitudinally polarized beams.

In the case of a longitudinally polarized electron beam one gets a longitudinal asymmetry

$$A_L = - P_e \frac{H_1 \ (1 + \cos^2\theta) + 2 \ H_3 \cos\theta}{G_1 \ (1 + \cos^2\theta) + 2 \ G_3 \cos\theta} \ . \qquad (26)$$

Connecting these expressions to asymmetries and polarization at the hadron level requires the use of specific models of fragmentation. Details of such studies are reported in the workshop notes[14,15] and in the literature.[13]

Two-jet physics may be possible without the detailed understanding of fragmentation processes. The forward-backward asymmetry for jets is the asymmetry in the polar angle distribution of the jet axis:

$$A_{F-B}^{jet} = \frac{\int_0^1 \frac{d\sigma}{d\Omega}\, d\,(\cos\theta) - \int_{-1}^0 \frac{d\sigma}{d\Omega}\, d\cos\theta}{\int_0^1 \frac{d\sigma}{d\Omega}\, d\cos\theta + \int_{-1}^0 \frac{d\sigma}{d\Omega}\, d\cos\theta} = \frac{3}{4}\frac{G_3}{G_1} \tag{27}$$

Obviously the problem here is to determine the direction of the jet axis, i.e., to distinguish the q from the $\bar{q}$ jet. Two methods have been proposed, one based on the average charge measurement of a jet where the particle detection efficiency introduces large fluctuations, and the other on leading particle identification[16] which appears difficult to use, the effect being attenuated by jet direction and leading particle misidentification. This measurement does not need a polarized beam, but the effect would be enhanced in such a case.

Difficulties of distinguishing q from $\bar{q}$ jets can be avoided in the case of the longitudinal asymmetry of symmetrically charged cross sections. The symmetrically charges cross section can be written the following way:

$$\left.\frac{d\sigma}{d\Omega}\right|_{qq} = \frac{d\sigma}{d\Omega}(\theta,\phi) + \frac{d\sigma}{d\Omega}(\theta-\pi,\ \phi+\pi) \tag{28}$$

Assuming universality between the quark generations one gets:

$$A_L^{jet} = -P_e \frac{N_u H_1^u + N_d H_1^d}{N_u G_1^u + N_d G_1^d} \tag{29}$$

N_u, N_d denote the numbers of u-type and d-type quarks for $m_q < E$. This effect is substantial and different electroweak models can be tested as discussed in the next section.

An interesting result in 3 jet events from $e^+e^- \to q\bar{q}g$ has been pointed out by J. G. Korner et al.,[17] and Fabricius et al..[18] Three-jet events lie in a plane whose normal has a polar angel η to the beam direction. The forward-backward asymmetry in this angle is called the beam-event asymmetry. In massless QCD, the beam-event asymmetry is identically null in order α_s^2. If one includes quark mass correction, the asymmetry for longitudinally polarized beam and/or high $Z^o - \gamma$ mixing is proportional to a factor R depending strongly on the quark mass. The sign of R is a signature of the gauge type of the theory, negative for non-abelian, i.e., with gluon self-coupling QCD type, and positive otherwise.

$$A_{B-e} = P_e \frac{\cos\eta}{1 + 1/2 \sin^2\eta} \tag{30}$$

where P_e is the beam polarization and η is the angle between the normal to the event plan and the e-beam direction. Possible measureable effects have been predicted. For massive quarks and high thrust values the maximum of the effect is found for $\theta_{12} = 120^o$, the angle between the quark and the anti-quark directions. This effect is one of the few sensitive tests of three gluon coupling, i.e., of the nonabelian type of the theory. A similar study for the final state $e^+e^- \to g\bar{g}g$ shows an effect too small to be measured.

D. Longitudinal Asymmetries, A_L, and Tests of Extended Gauge Models[14,15]

It is possible that the structure of the neutral currents could be more complicated than in the standard model. Classes of models have been constructed with more than one neutral boson but presenting the same low energy behavior as the standard model. The longitudinal asymmetry A_L, integrated over the entire solid angle, depends on the factors

$$\frac{v_e/a_e}{1 + (v_e/a_e)^2}$$

in the standard model at the Z^o pole, and is predicted to be small ($A_L \approx -0.16$ for $\sin^2\theta_w = .23$). If additional heavy neutral gauge bosons exist, they also contribute to the production amplitudes and to the value of A_L. Measurements of A_L is a sensitive way to distinguish between

alternative gauge theory models. To illustrate this fact, we will consider two different models.

1. $SU(2) \times U(1) \times \tilde{U}(1)$

This model[19] gives exactly the same predictions as the $SU(2) \times U(1)$ standard model at low momentum transfers in the spacelike region, but has a richer neutral gauge boson structure which may be investigated in the upper SLC energy range. The main characteristics are

(i) All fermions are assumed to be invariant under $\tilde{U}(1)$ and to transform under $SU(2) \times U(1)$ in exactly the same manner as in the standard model.

(ii) The symmetry breaking occurs via the usual scalar weak isodoublet field ϕ_1, which is assumed to be invariant under $U(1)$, and an additional field ϕ_2, which is invariant under $SU(2)$ but transforms nontrivially under $U(1) \times \tilde{U}(1)$.

These assumptions lead to a $W^{\pm}$ boson exchange structure for charged-current interactions similar to the standard model. But the additional Higgs field ϕ_2 provides a mass for an additional neutral gauge boson associated with $U(1)$ and the model has thus two physical neutral bosons Z_1 and Z_2 (plus the photon) which have the interesting properties that

$$M_1 \leq M_{W^{\pm}}/\cos\theta_w \leq M_2 \tag{31}$$

where the mass $M_{W^{\pm}}$ of the charged bosons is given by the Weinberg-mass relation, also valid in this model;

$$M^2_{W^{\pm}} = \pi\, \alpha/\sqrt{2}\, G_F \sin^2\theta_w \quad . \tag{32}$$

This model becomes identical to the standard model whenever one of the two neutral gauge boson masses (or both of them) approaches the standard model value

$$M_{Z^o} = M_{W^{\pm}}/\cos\theta_w \quad . \tag{33}$$

In fact, the deviation of the gauge boson masses from the standard model value M_{Z^o} can be measured by a coefficient $C(\tilde{U}(1))$ which has the following expression:

$$C\left(\tilde{U}(1)\right) = \cos^4\theta_w \left(\frac{M_{Z^o}^2}{M_1^2} - 1\right)\left(1 - \frac{M_{Z^o}^2}{M_2^2}\right) \quad . \tag{34}$$

One verifies readily that $C\left(\tilde{U}(1)\right) \to 0$ when M_1 and/or $M_2 \to M_{Z^o}$. Comparison with experiments place a lower bound on M_1 ($M_1 \gtrsim 30$ GeV) but no bounds outside relation (31) exist for M_2. This model possesses three free parameters, the weak angle θ_w, and M_1 and M_2, the masses of the two neutral bosons. In the following, we will fix the mass of the first observed neutral gauge boson (M_{Z^o} in the standard Model, M_1 in the extended gauge models) to 89 GeV. This value corresponds to $\sin^2\theta_w = 0.230$ in the standard model. To fill the condition (31) in the $SU(2) \times U(1) \times \tilde{U}(1)$ model, we fix, in this model, $\sin^2\theta_w = 0.220$ in agreement with the actual world average of $\sin^2\theta_w = 0.230 \pm .015$.

Figure 15 shows the ratio of the total cross section to the point-like QED cross section of the reaction

$$e^+e^- \to Z^o \to \mu^+\mu^-$$

calculated for a polarization of electron beam of 50% in the standard model and in the $SU(2) \times U(1) \times \tilde{U}(1)$ model. The total luminosity has been normalized to give 10^6 Z^o's in the standard model. The parameters of $SU(2) \times U(1) \times \tilde{U}(1)$ model have been taken to be: $M_1 = 89$ GeV, $\Gamma_1 = 2.3$ GeV, $M_2 = 200$ GeV and $\Gamma_2 = 2.5$ GeV. It is clear from this result that the measurement of the total cross section on the top of the resonance will not bring any light on the type of model which would be the right one.

Figure 16 shows the longitudinal asymmetry A_L calculated in the standard model (S.M.) and in the $SU(2) \times U(1) \times \tilde{U}(1)$ model with the same parameters as given above but by varying the value of the mass M_2 of the second neutral boson.

The results can be summarized by the following remarks:

(i) The value of A_L observed at $\sqrt{s} = 89$ GeV is due to the choice of the values of M_1 and $\sin^2\theta_w = 0.220$. There is no sensitivity to the value of the mass of the second neutral boson unless this mass is close to the first one (M_2 less than 100 GeV).

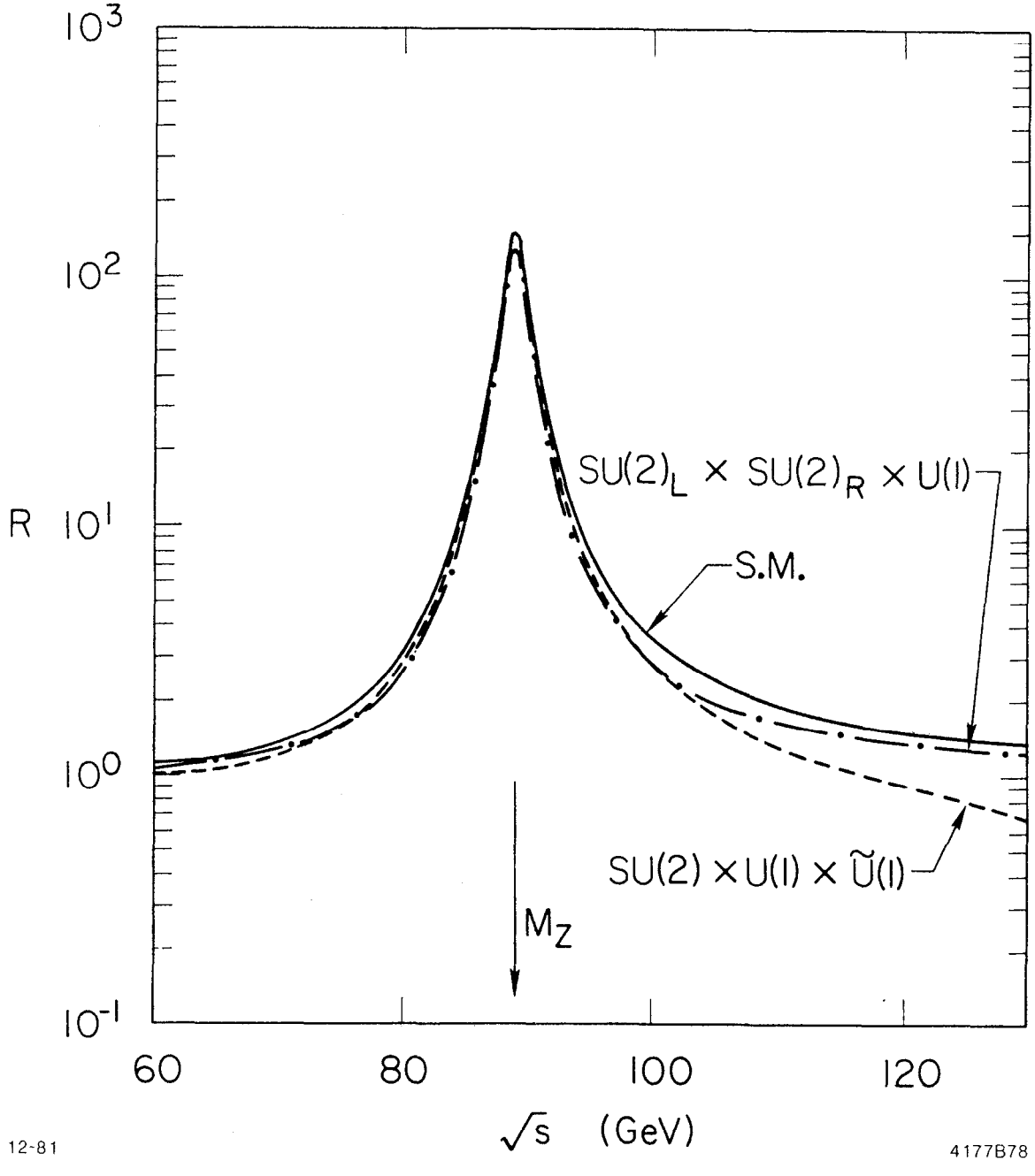

Fig. 15. Ratio to the point-like QED cross section of the cross section of the reaction $e^+e^- \to \mu^+\mu^-$ calculated in the standard model (S.M.) and in the $SU(2) \times U(1) \times \tilde{U}(1)$ and $SU(2)_L \times SU(2)_R \times U(1)$ models. The parameters are given in the text.

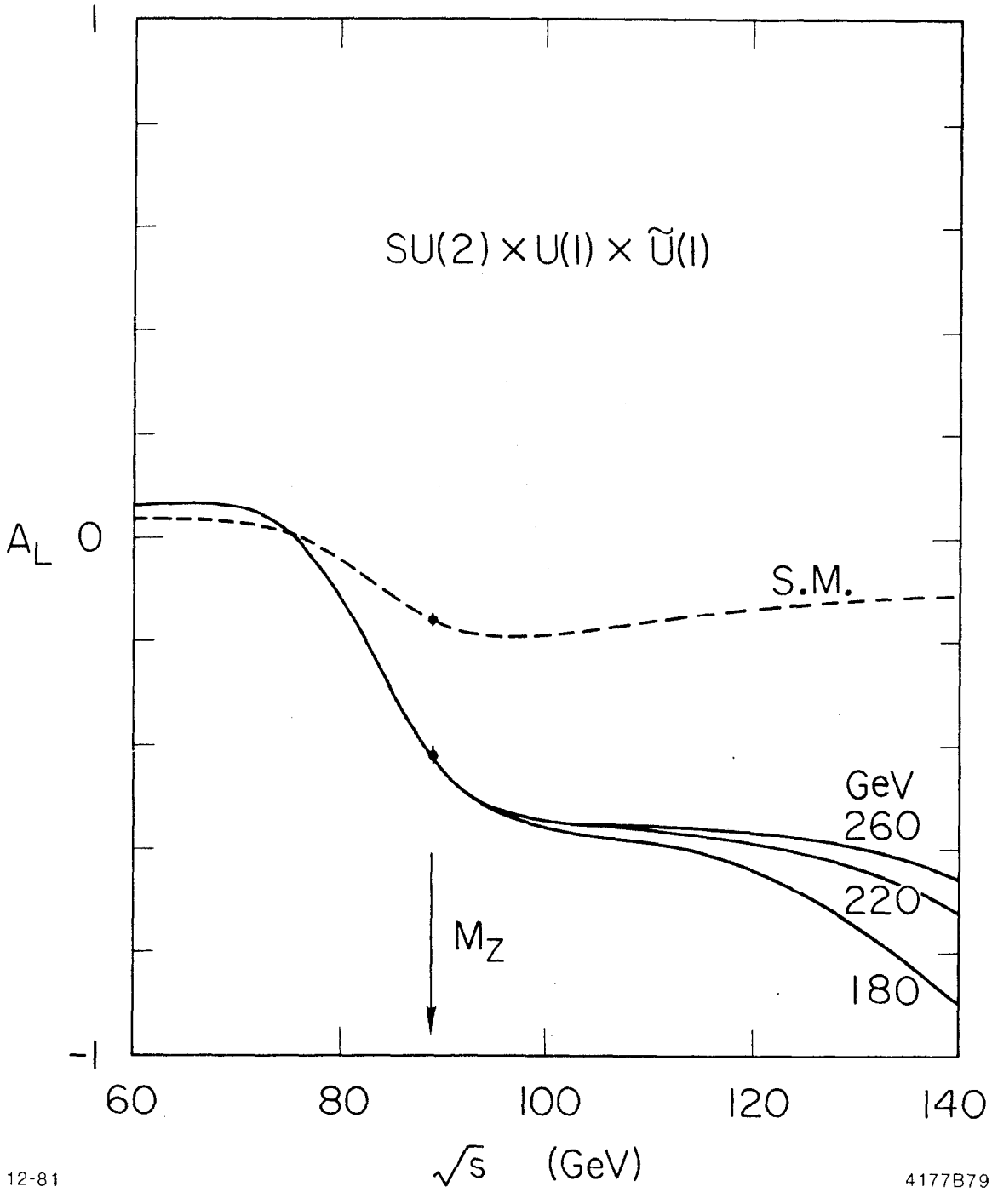

Fig. 16. Longitudinal asymmetry as a function of $\sqrt{s}$ calculated in the standard model (S.M.>) and in the SU(2) × U(1) × $\tilde{U}$(1) model for different values of the mass of the record neutral boson. The other parameters are given in the text. The two data points indicate the statistical accuracy expected for 3×10^4 Z^o decays.

(ii) For $\sin^2\theta_w = 0.230$ and $M_Z = 89$ GeV, the $SU(2) \times U(1) \times \tilde{U}(1)$ model gives exactly the same value for A_L as the standard model. But in this limit, the strengths of couplings of the second boson Z_2 go to zero, although the mass of Z_2 is still a free parameter.

The main point of this model is that the masses of Z_1, Z_2 and $\sin^2\theta_w$ are free parameters, while in the standard model $\sin^2\theta_w$ is the only free parameter. We see then that a change of about 5% in $\sin^2\theta_w$ induces, at this energy and for the parameters listed above, a change of a factor about 2.6 on A_L: for $\sin^2\theta_w = 0.220$, $A_L = -0.42$ and for $\sin^2\theta_w = 0.210$, $A_L = -0.66$. This variable is thus very sensitive to the value of $\sin^2\theta_w$ and will be a fundamental measurement to complement the measurement of the total cross section. Given the position of the (maybe nonunique) Z^o, the longitudinal asymmetry A_L will give with a very high accuracy the values of $\sin^2\theta_w$. A possible discrepancy between these two measurements of $\sin^2\theta_w$ will be a very precise test of the gauge model and could be explained by such type of model as $SU(2) \times U(1) \times \tilde{U}(1)$.

2. $SU(2)_L \times SU(2)_R \times U(1)$

The characteristic of the models based on this group is the basic left-right symmetry, wherein left- and right-handed quarks transform as doublets under different SU(2) factors. A complete study of this type of model, including a comparison with experimental data, has been done by Liede et al.[20] Studies at energies comparable to those which will be reached by SLC have been done by Degrange[21] and Hollik.[13] However, these works do not focus on the special tool given by the measurement of the longitudinal asymmetry which is possible with a polarized electron beam in the SLC. We discuss here the specific model of De Rujula et al.,[22] denoted DGG_ in Ref. 13, which, with a specific choice of the symmetry breaking parameter, has the right low energy behavior.

The main features of this model are:

(i) The $SU(2)_L$ and $SU(2)_R$ groups have a common coupling constant

$$g = e/\sin\theta_w \tag{35}$$

The U(1) coupling denoted g', is related to g by the relation

$$g'/g = \sin\theta_w/\sqrt{\cos 2\theta_w} \tag{36}$$

(ii) To give masses to six of the seven gauge bosons (4 charged W's and 3 neutral bosons, γ, Z_1, Z_2), Higgs fields are introduced with the vacuum expectation values $\lambda_{L,R}$ (contributions to both neutral and charged boson masses, and neutral currents violate parity only if $\lambda_R \neq \lambda_L$), $b_{L,R}$ (contribution only to charged boson masses), k and k' (mixes $W_L^{\pm}$ and $W_R^{\pm}$ and affects the masses of the neutral bosons).

To suppress right-handed charged currents at low energy, a very large mass has to be given to $W_R^{\pm}$ by taking $b_R >> b_L$ and/or $\lambda_R >> \lambda_L$.

The physical parameters of this model are g, g', M_{Z_1}, M_{Z_2}, M_{W_1}, M_{W_2}, $K^2 = k^2 + k'^2$, kk'.

The two parameters g and g' are fixed using the relations (35) and (36) and

$$(kk')^2 = - \frac{M_{W_1}^2 \, M_{W_2}^2}{g^4} \left(1 - C \, M_{W_1}^2\right)\left(1 - C \, M_{W_2}^2\right) \qquad (37)$$

where $C = 8 \, G_F/g^2\sqrt{2}$.

Then, for the neutral sector, we are left with 4 parameters chosen to be $\sin^2\theta_w$, M_{Z_1}, M_{Z_2} and K^2.

In the De Rujula-Georgi-Glashow model, the vacuum expectation $\lambda_L = 0$ and only λ_R is used to give mass to $W_R^{\pm}$. Parity is thus violated in neutral current processes and we have the following condition

$$K^2 = \frac{1}{2g^2}\left\{ M_{Z_1}^2 + M_{Z_2}^2 \pm \left[\left(M_{Z_1}^2 + M_{Z_2}^2\right)^2 - 8 \, M_{Z_1}^2 \, M_{Z_2}^2 \, \frac{1 + r^2}{1 + 2r^2}\right]^{1/2}\right\} \qquad (38)$$

where $r = g'/g$.

From the two possible signs of the root in Eq. (38), the positive one would imply a reduction of parity violating effects in electron-nucleus reactions relative to the standard model and is excluded by the SLAC results.[23] Therefore, in the following, we only consider the negative root denoted DGG_- in Ref. 13.

Since K^2 has to be real, there follows a condition on the masses of the two neutral bosons

$$M_{Z_2}/M_{Z_1} \geq \left(\sqrt{2 + 2r^2} + 1\right)\Big/\sqrt{1 + 2r^2} \quad . \qquad (39)$$

This relation has a consequence that, for $\sin^2\theta_w = 0.230$ and $M_1 = 89$ GeV, M_2 should be equal to or bigger than about 180 GeV.

In the following, we will then fix the mass of the first observed neutral gauge boson (M_{Z^o} in the standard model, M_1 in the $SU(2)_L \times SU(2)_R \times U(1)$ model) to 89 GeV. This value corresponds to $\sin^2\theta_w = 0.230$ in the standard model and will be also used in this extended gauge model.

Figure 15 shows the ratio to the point-like QED cross section of the total cross section calculated for a polarization of electron beam of 50% in the $SU(2)_L \times SU(2)_R \times U(1)$ model. The total luminosity has been normalized as described above.

The parameters of $SU(2)_L \times SU(2)_R \times U(1)$ has been taken to be: $M_1 = 89$ GeV, $\Gamma_1 = 2.3$ GeV, $M_2 = 400$ GeV and $\Gamma_2 = 2.5$ GeV.

In this case, the measurement of the total cross section on the top of the resonance might be able to distinguish between models, but secondary effects like radiative corrections can obscure this measurement.

Figure 17, on the other hand, shows the large effects on the longitudinal asymmetry A_L in this extended gauge model. In Fig. 17(a), this asymmetry has been plotted as a function of $\sqrt{s}$ for different values of the mass M_2 of the second gauge boson. In this case, the effects of the presence of a second gauge boson can be very well measured at $\sqrt{s} = M_1$ and a discrepancy from the standard model value will give a determination of the second mass. Figure 17(b) illustrates this effect by showing, as a function of M_2, the expected value of A_L in the $SU(2)_L \times SU(2)_R \times U(1)$ model. We see that a measurement of A_L at $\sqrt{s} = 89$ GeV can give some bounds on the existence and the mass value of a second neutral gauge boson: if this mass is less than about 350 GeV one should be able to measure a deviation from the Weinberg-Salam model value. For higher values of this mass, the model gives a value of A_L compatible with that obtained in the standard model.

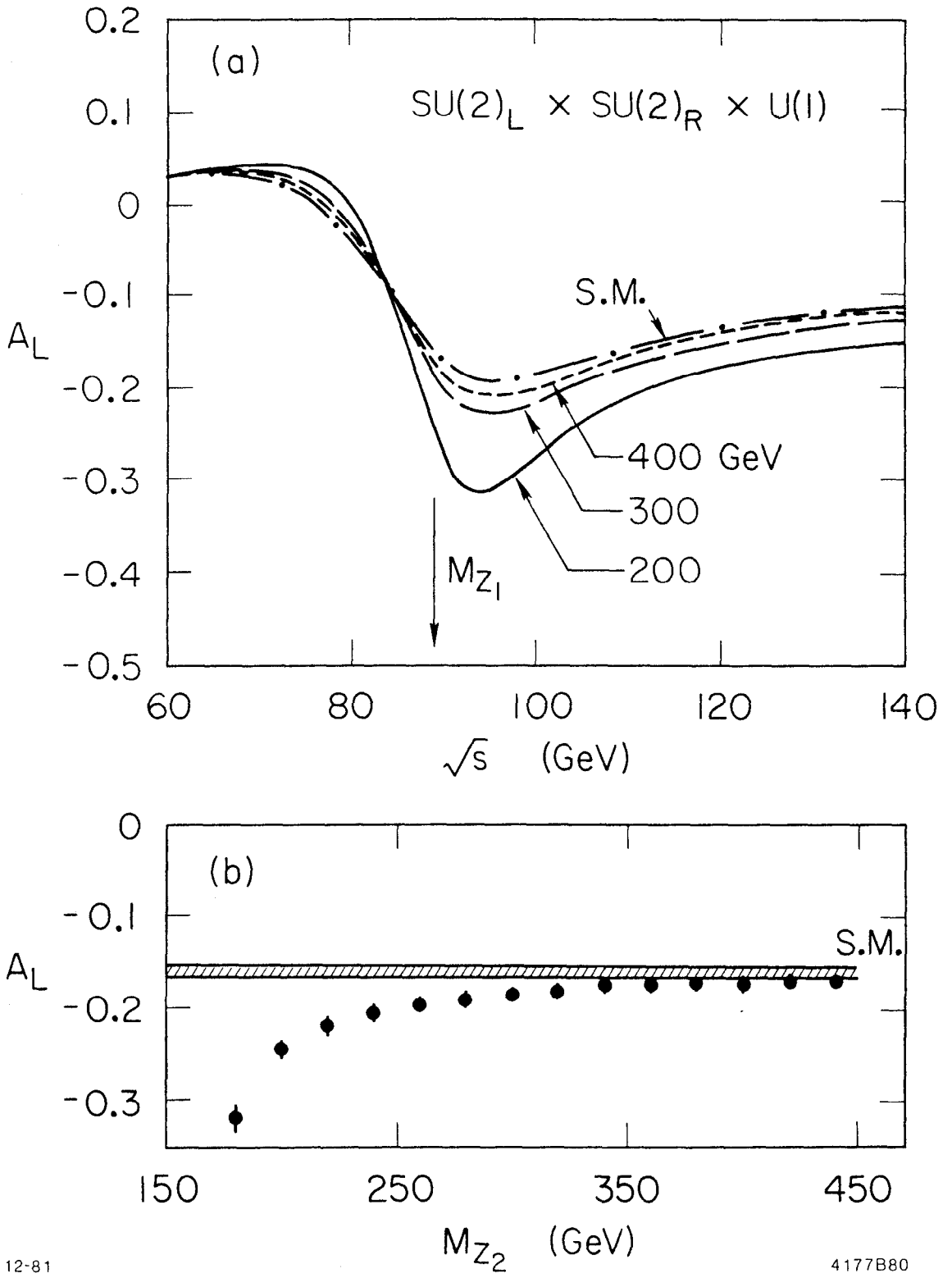

Fig. 17. Longitudinal asymmetry calculated in the standard model (S.M.) and in the $SU(2)_L \times SU(2)_R \times U(1)$ model; (a) as a function of $\sqrt{s}$ and for different values of the mass of the second neutral boson; (b) at $\sqrt{s}$ = 89 GeV, comparison of the A_L value in the standard model and in the $SU(2)_L \times SU(2)_R \times U(1)$ model as a function of the mass of the second neutral boson for 3×10^4 Z^o decays.

REFERENCES

1. W.K.H. Panofsky, Spin Motion in Synchrotron Orbits, SPEAR Note 142 (1972).

2. R. Prepost, SLC Workshop Note No. 70; and C. Y. Prescott, SLAC-TN-73-1, January 1973. A copy of this report can be obtained in SLC-Workshop Note No. 72.

3. H. Ogren, SLC Workshop Note No. 22 (1981).

4. J. Button-Shafer, SLC Workshop Note No. 28 (1981).

5. J. Kim et al., Rev. Mod. Phys. 53, 211 (1981).

6. C. Y. Prescott, SLAC-PUB-2649 (1980).

7. J. E. Brau and G. J. Tarnopolsky, SLC Workshop Note No. 64 (1981).

8. J. E. Brau and G. J. Tarnopolsky, SLC Workshop Note No. 41 (1981).

9. J. E. Brau and G. J. Tarnopolsky, Phys. Rev. D1, (1981).

10. D. Perret-Gallix, SLC Workshop Note No. 44 (1981).

11. J. E. Augustin and F. M. Renard, Nucl. Phys. B162, 341 (1980).

12. A. Bartl et al., Z. Phys. C6, 335 (1980).

13. W. Hollik, Z. Phys. C8, 149 (1981).

14. G. Bonneaud, SLC Workshop Note No. 21 (1981).

15. G. Bonneaud et al., SLC Workshop Note No. 32 (1981).

16. M. Davier and F. Richard, ECFA/LEP 34 (1979).

17. J. Korner et al., Phys. Lett. 94B, 207 (1980).

18. K. Fabricius et al., Phys. Rev. Lett. 45, 867 (1980).

19. E. H. De Groot, G. J. Gounaris and D. Schildknecht, Phys. Lett. 85B, 399 (1979); Z. Physik C5, 127 (1980).

20. I. Liede, J. Maalampi and M. Roos, Nucl. Phys. B146, 157 (1978).

21. B. Degrange, CERN 79-01, Vol. 2, p. 517 (1979).

22. A. De Rujula, H. Georgi and S. L. Glashow, Phys. Rev. D12, 3589 (1975); Ann. of Phys. 109, 242, 258 (1977).

23. C. Y. Prescott et al., Phys. Lett. 77B, 347 (1978).

Positrons for the SLC will be produced by extracting the electron beam two-thirds of the way down the linac and dumping it on a thick target. The positrons produced are focused, accelerated to 200 MeV, and sent back down to the injector region of the linac. This target must dissipate 7 kilowatts of power over a millimeter spot. The resulting shock wave produces stresses near the limit of many materials. In the target pictured here the darkened region is a one-quarter inch diameter by one inch long slug of tungsten-rhenium composite which was exposed to about one million pulses of 24 GeV electrons in a test in End Station A at SLAC.

PHYSICS PARAMETERS

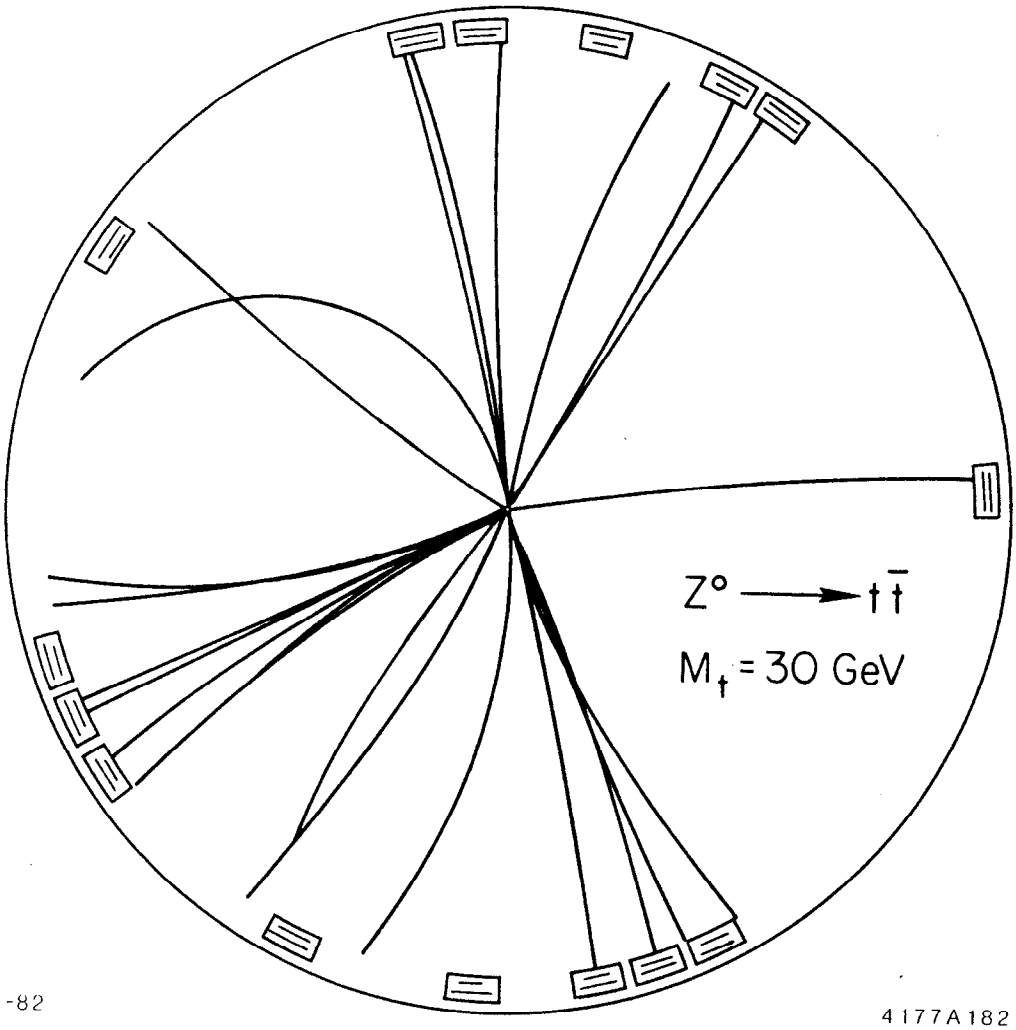

1-82

4177A182

PHYSICS PARAMETERS

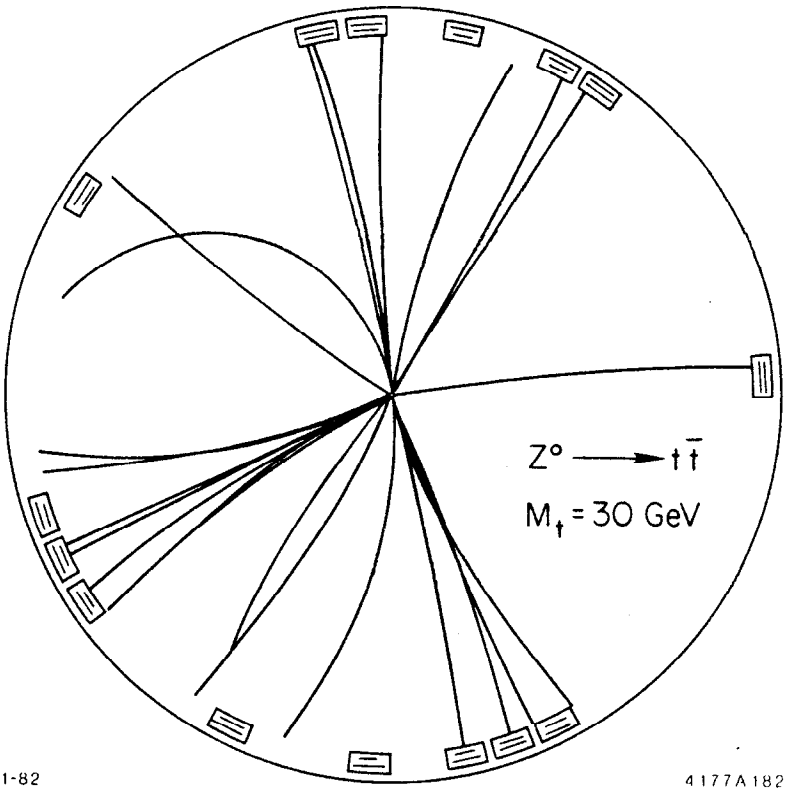

1-82

4177A182

I. INTRODUCTION

This report describes the work of the Parameters Group active during the Stanford Linear Collider Workshop. The purpose of the physicists in this group was to investigate experimental aspects of the electron-positron annihilation mediated by the weak neutral gauge boson. Since their goal was to establish the experimental requirements to be met by detectors, rather than solve the technical problems they raise, a conscious effort was made to avoid technological issues. The interests of the participants are reflected in the three chapters of this report: $Z^o \rightarrow$ HADRONS, $Z^o \rightarrow$ CHARGED LEPTONS, and OTHER PROCESSES. The sections on hadrons review general characteristics of the multi-hadron final states and investigate the parameters of detectors capable of studying the jets of produced particles, with special emphasis on the solid angle, segmentation, and energy and momentum resolution issues. The studies of the charged lepton channels deals with these topics too, but in addition consider the statisical accuracy of the data, the magnitude of the weak effects, and the accuracy of determination of weak parameters in the framework of the SU(2) × U(1) model. Finally, the studies of lower rate processes, such as Higgs particle production and radiative Z^o production, expand the discussion to include the magnitude of background processes and specific detector requirements.

Almost all the work summarized below has been abstracted from SLC Notes written during the Workshop, for which this report should be considered a reading guide: the SLC Notes contain considerably more information, details, and references than presented here.

II. $Z^0 \rightarrow$ HADRONS

A. General Discussion

1. Introduction

The standard model postulates that the Z^0 couples with comparable strength to all quarks. As predicted by the model, neutrino interactions and deep-inelastic electron scattering experiments have provided direct evidence for a neutral weak current coupling to the up and down quarks of stable matter. However, the study of neutral current interactions involving heavier quarks is left to the Z^0 decay experiments, as there appear to be no neutral currents involved in the flavor-changing weak transitions.

The Z^0 is expected to decay into quarks about three quarters of the time. Beyond the issue of the quarks' weak couplings, the abundance of hadronic final states will expand the impact of SLC physics into the realm of quantum chromodynamics (QCD). The $Z^0 \rightarrow$ HADRONS sections of this report discuss the study of the hadron jets from what may be called a QCD-biased vantage point. The difficult problem of the separate measurement of the quarks' weak coupling constants, for which flavor identification is a prerequisite, is not discussed in detail. Experimentally, the understanding of the quark fragmentation process may render this latter problem more tractable.

Extrapolation of Monte Carlo models which successfully describe QCD phenomena at PEP and PETRA energies suggests that the hadronic events comprise 71% $q\bar{q}$, 26% $q\bar{q}g$, and 3% $q\bar{q}gg$, with the notation of q = quark and g = gluon. In addition, rare or new processes, such as Higgs particles or heavy lepton production and decay, may lead to multi-jet events. Because of the high parton energies in these events, the jets are generally strongly collimated and are expected to have high average charge $\langle n_{ch} \rangle$ and photon $\langle n_\gamma \rangle$ multiplicities $\langle n_{ch} \rangle \simeq \langle n_\gamma \rangle \simeq 22$. For the postulated sixth, or top, quark these numbers are expected to be even higher. Since the transverse dimension of the jet is about inversely proportional to the parton momentum, multi-jet topologies will probably be more easily studied at $\sqrt{s} = M_{Z^0}$ than at the present PEP/PETRA regime. Thus, the nature of the quark and gluon fragmentation will be exhaustively studied

at the SLC. All these issues relate to the solid angle coverage and segmentation characteristics of the detector components.

The SLC will achieve its luminosity by reducing the lateral dimensions of the beams to micron sizes. Given these source dimensions, it is natural to consider lifetime measurements of leptons and heavy quark states, and the possibility that the detection of decay vertices may help to identify quark flavors. Detectors of very fine granularity will be required for this study.

It is conceivable that the top quark will not have been discovered before the SLC turn-on time. This possibility has stimulated the study of how to isolate the top-quark events and how to determine the top quark mass.

All the QCD questions mentioned above are discussed in this chapter. After a brief description of the Monte Carlo program parameters, we present in this Section A results on multiplicities and charged particle and photon momentum spectra. These dictate the global detector parameters, namely solid angle and segmentation, discussed below in Section B. Topics related to hadron spectroscopy, such as vertex reconstruction and two-body invariant masses appear in Section C. Issues related to ancestor quark identification are the subject of Section D. The $Z^o \rightarrow$ HADRONS discussion ends in Section E with a study of high energy jets.

2. Event Simulation

The Parameters Group had at its disposal two simulation models for $e^+e^- \rightarrow$ hadrons. Available in the HOWL Monte Carlo software package,[1] the model of Ali et al.,[2] is familiar because of its widespread use at PETRA and PEP. Also available is the TUBES model,[3] developed in the same spirit as the so-called LUND Monte Carlo.[4] Both programs simulate Z^o events with weak couplings determined by the standard SU(2) × U(1) model.[5,6]

The characteristics of the simulated data sample depend on the weak interaction parameters, which govern the quark pair-production process, and on the QCD and quark fragmentation parameters, which control properties of the jets such as particle multiplicity and opening angles. For the weak process, the values $\sin^2\theta_w = 0.23$, $M_{Zo} = 88.6$ GeV and $\Gamma_{Zo} = 2.5$ GeV were used. The beam energy was constant $E_b = M_{Zo}/2$, and no polarization

or radiative effects were considered. Unless otherwise stated, the events contain all six quark flavors, with the top quark mass M_t = 19 GeV. The value chosen for the QCD scale parameter was Λ = 0.35 GeV ($\alpha_s(E_b)$ = 0.16). For all parton flavors the fragmentation average transverse momentum was the same, $\langle p_T \rangle$ = 0.3 GeV/c.

Comparison of the two Monte Carlo programs mentioned above showed some differences — the most important of which are ascribably to differences in the description of heavy quark fragmentation and of couplings to gluons. Since these issues are by no means settled, conclusions which depend critically on the predictions of Monte Carlo models must be treated with considerable caution. The results presented in this chapter were all obtained with the Ali et al.,[2] model.

Projections of typical events on a plane perpendicular to the beams appear in Fig. 1 ($Z^o \to d\bar{d}$), Fig. 2 ($Z^o \to t\bar{t}$), and Fig. 3 ($Z^o \to s\bar{s}g$). The trajectories bend in a 5 kG solenoidal field.

3. Particle Multiplicities, Momentum Spectra

Figure 4 shows the charged and photon multiplicities for $Z^o \to$hadrons.[7] The mean multiplicities are $\langle n_{ch} \rangle$ = 22 and $\langle n_\gamma \rangle$ = 21 with halfwidths in the range of 10 particles. Since most events consist of two jets, the typical particle multiplicity per jet is 22. Figure 5 shows the charged particle density as a function of the cosine of the angle relative to the jet axis for u, d, s, and c quarks and for t quarks. The corresponding photon density distributions are very similar to these. The density distribution for the light quarks is more narrowly collimated than for the t's. For instance, half the multiplicity in a light quark jet is contained in a cone of half-angle 14^o centered around the jet axis, while half the energy is contained in a cone of half-angle 4^o. The corresponding half-angles for t jets are much larger, 39^o and 20^o, respectively.

Figure 6 shows the charged particle momentum spectra. They are characterized by numerous low energy particles and a large dynamic range. Half of the pions have momenta below 1 GeV/c. Figure 7 shows the photon energy spectrum, which exhibits similar structure: half of the photons have energies below 0.3 GeV.

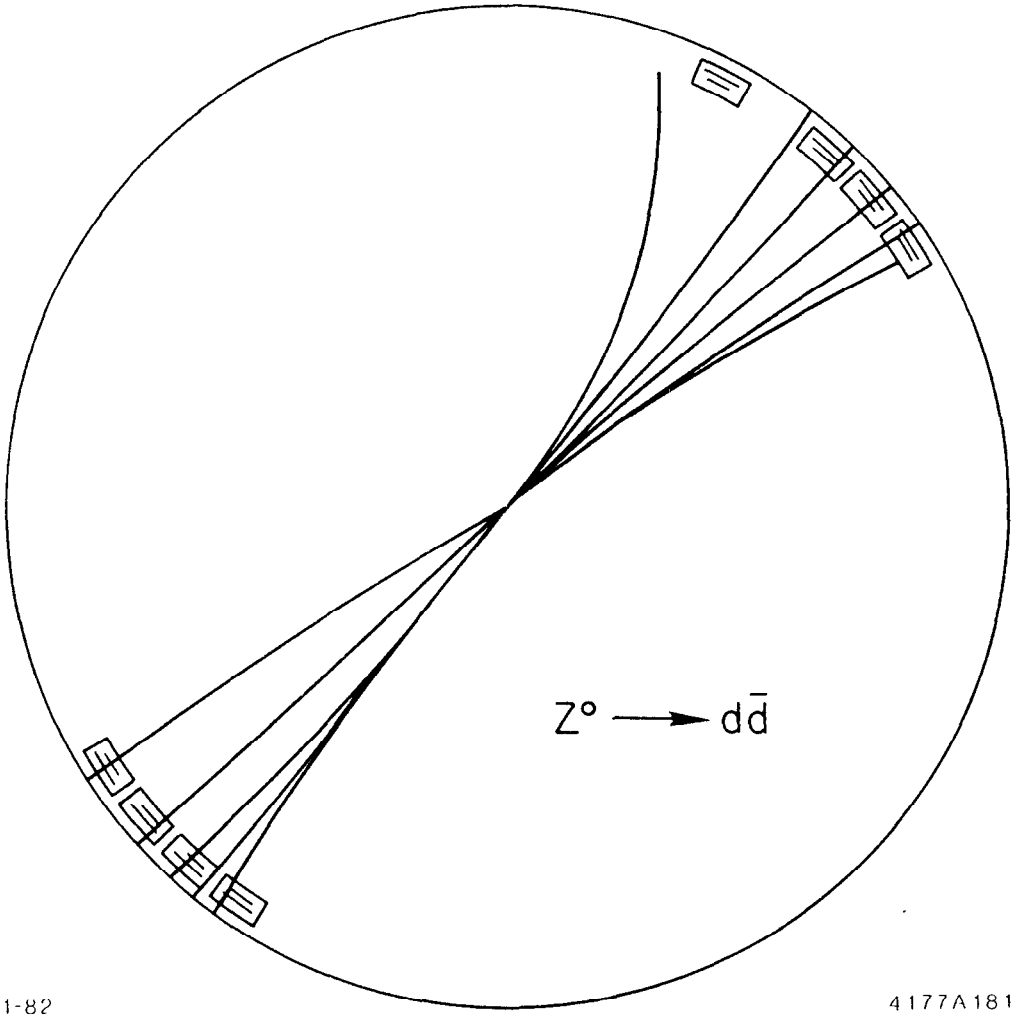

Fig. 1. Projection of the trajectories of charged particles, for an event of the type $Z^0 \rightarrow d\bar{d}$, on a plane perpendicular to the beams. The solenoidal field strength is 5 kG.

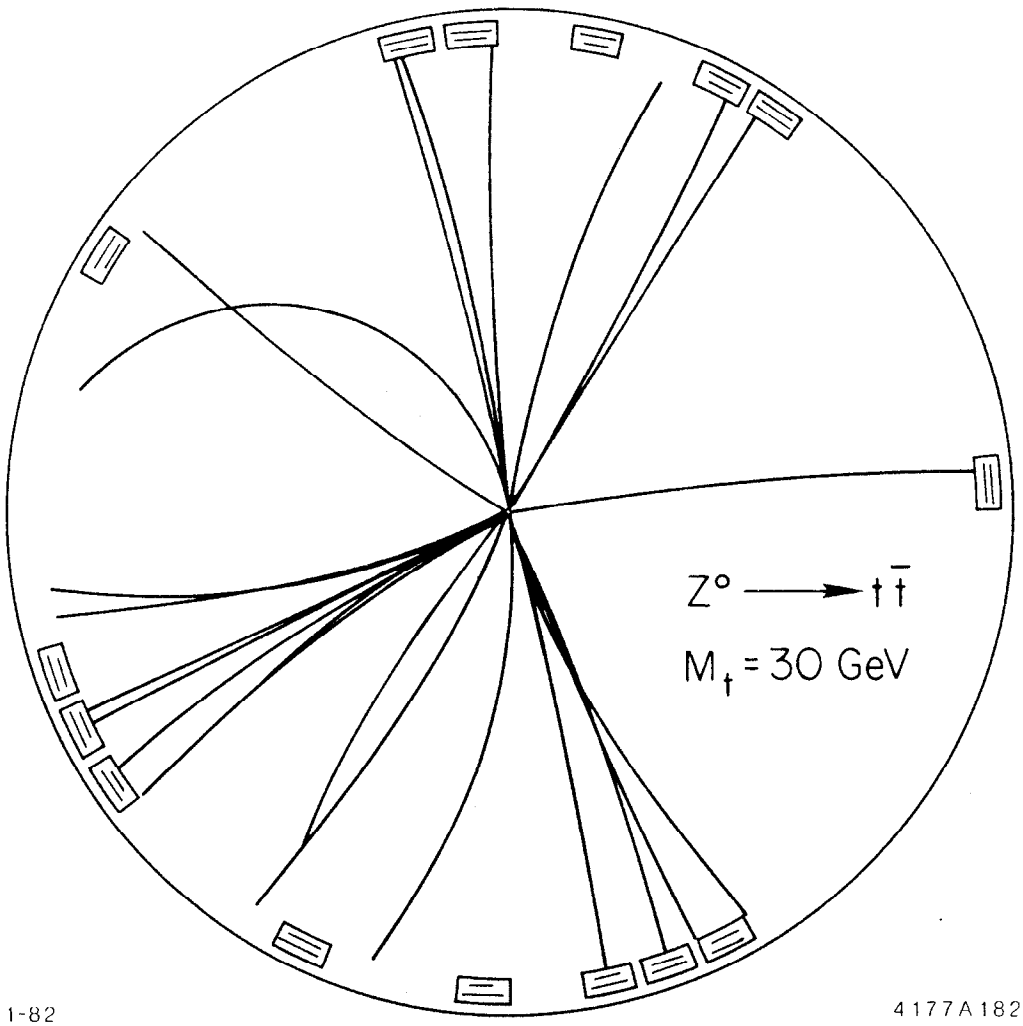

Fig. 2. As Fig. 1, for an event of the type $Z^{o} \rightarrow t\bar{t}$.

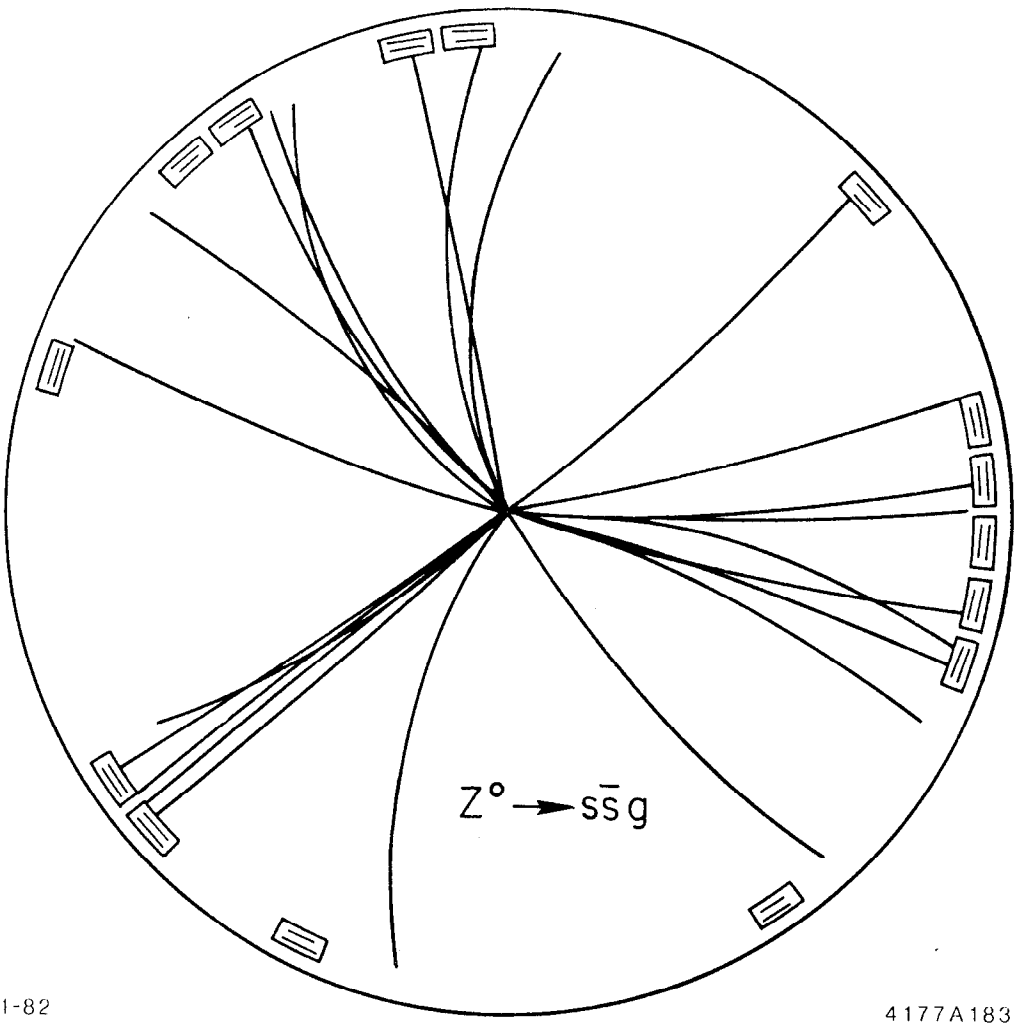

Fig. 3. As Fig. 1, for an event of the type $Z^{o} \rightarrow s\bar{s}g$.

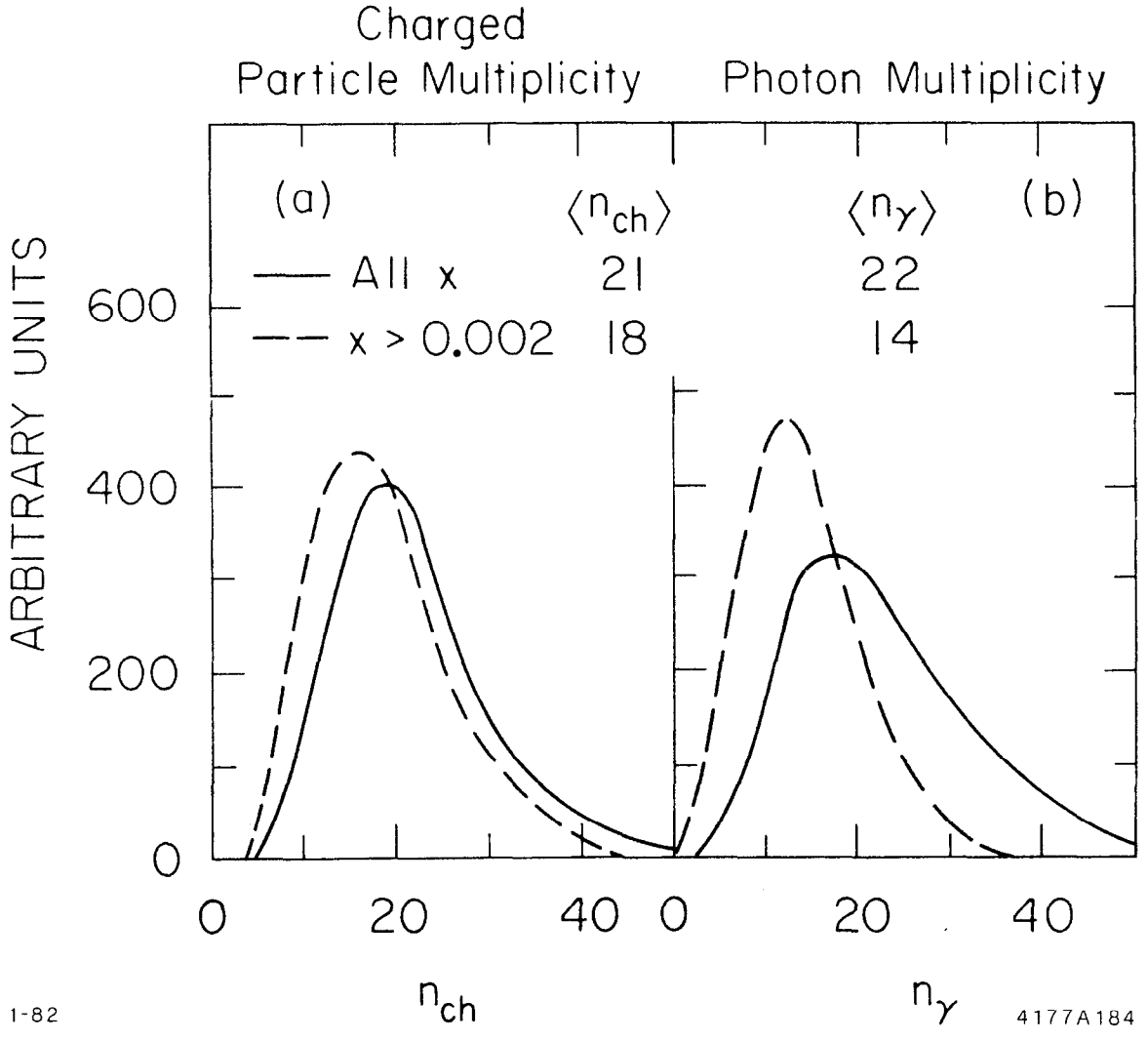

Fig. 4. Distribution of particle multiplicities for the process $e^+e^- \rightarrow Z^0 \rightarrow$ hadrons for (a) charged particles, and (b) photons. The dashed curves refer to particles with $x = p/E_b > 0.002$.

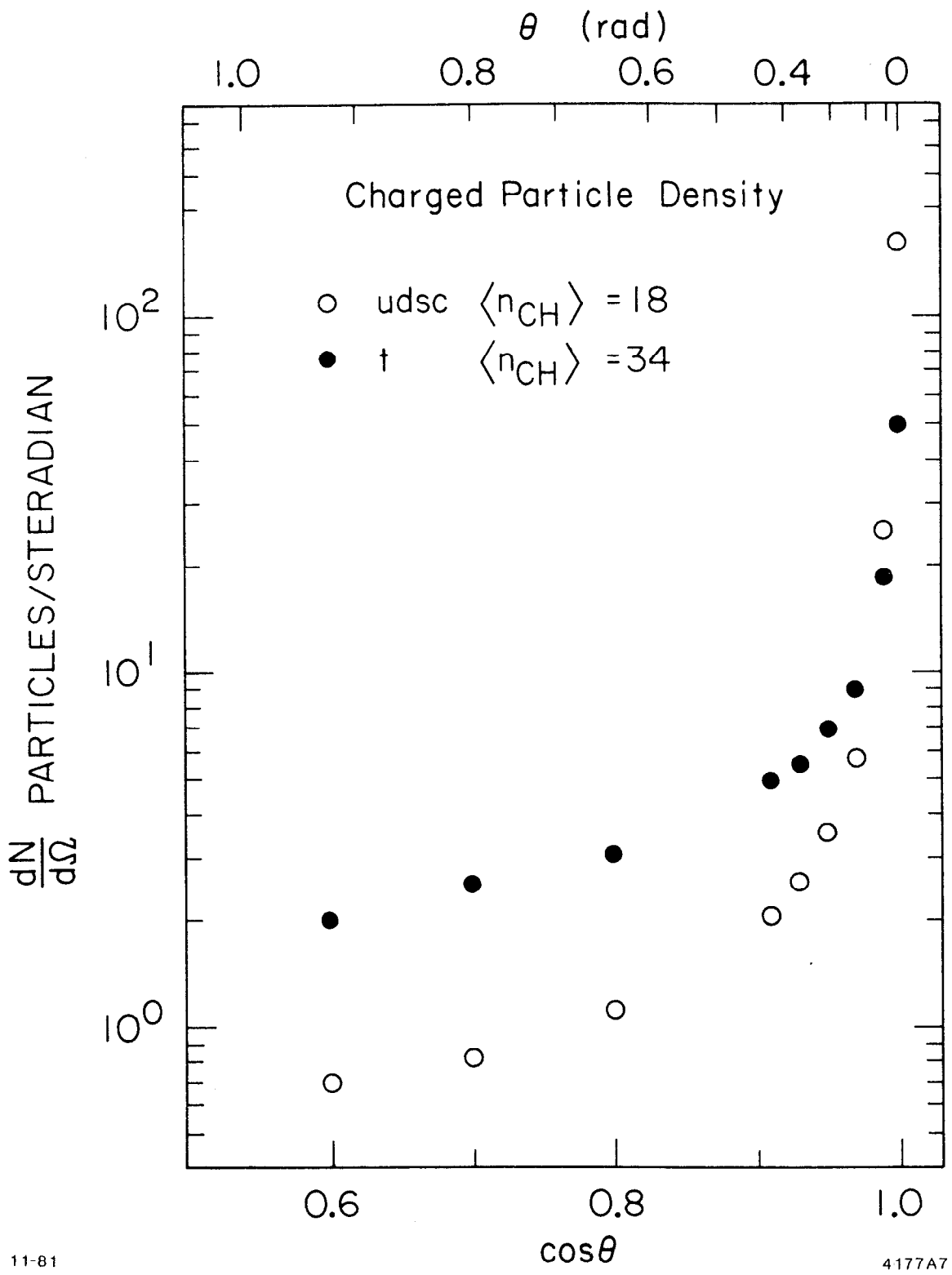

Fig. 5. Charged-particle density as a function of the cosine of the angle relative to the direction of the primordial quarks, separately for the light quarks and for the t quarks.

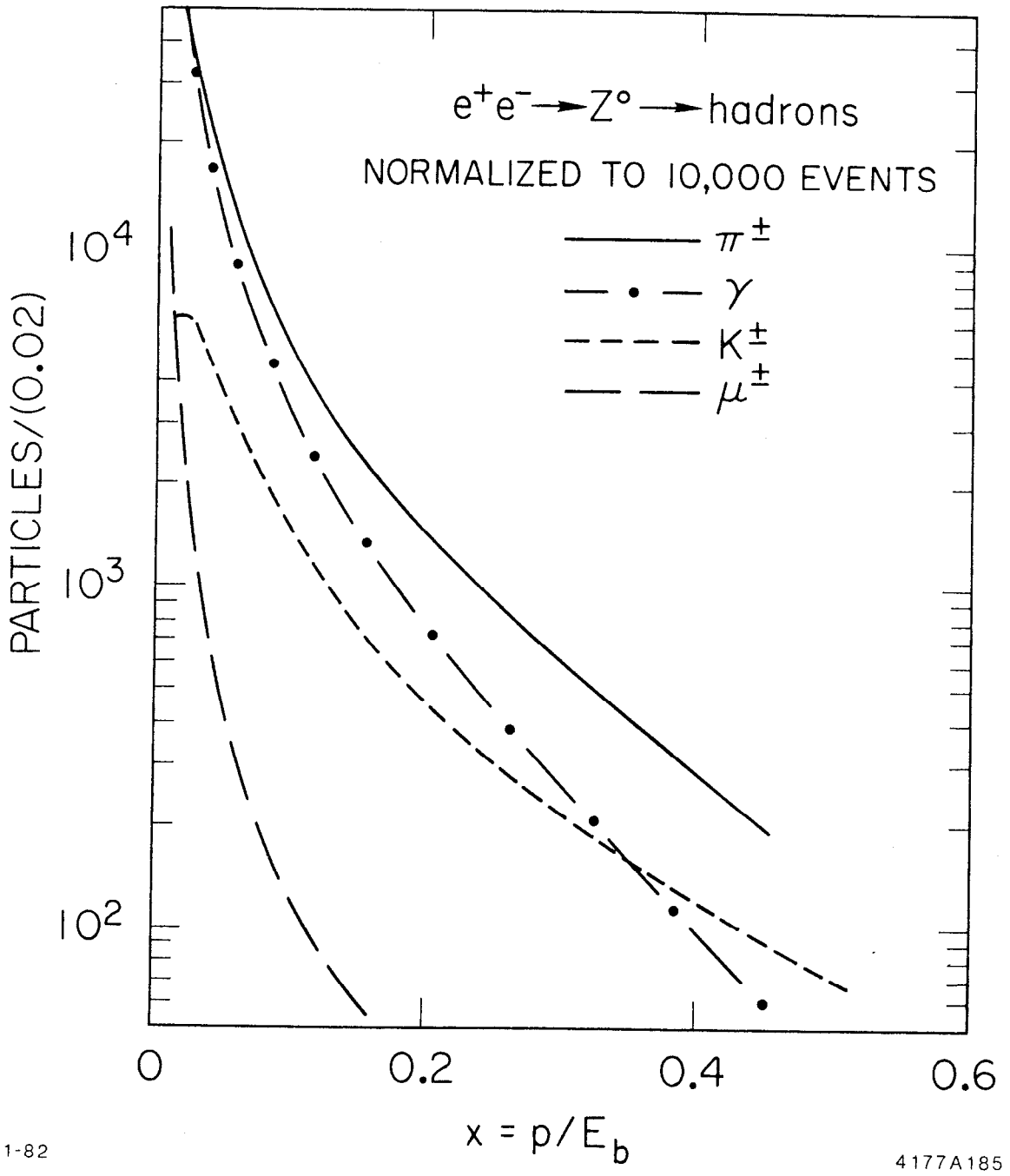

Fig. 6. Momentum distribution of different particle species as a function of $x = p/E_b$, normalized to 10,000 events.

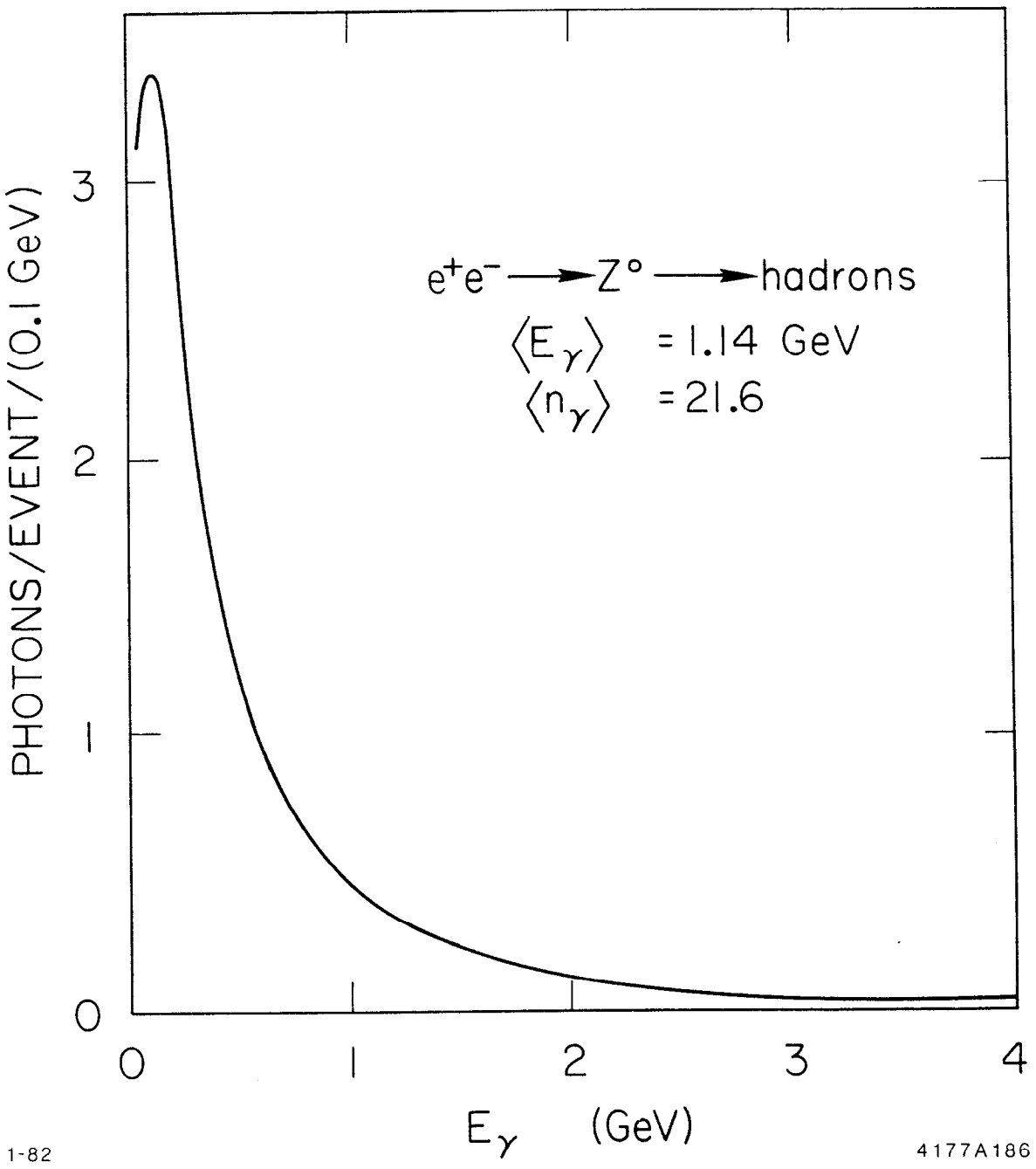

Fig. 7. Photon energy spectrum.

The average particle energies and multiplicities for events from all six quarks and from the t quark only appear in Table I.[8] The t events have multiplicities, lepton yields, and lepton momenta significantly above the average values.

Table I

Average particle momenta, median momenta, and particle multiplicities for hadronic events, including gluon radiative events: (a) all hadronic events, and (b) events from t quark only. The quoted numbers of electrons and muons include electrons from Dalitz pairs and muons from pion and kaon decay, as well as decay products of c, b, and t quarks. The latter amount to 0.2 electron and 0.2 muon (all quarks) and 0.6 electron, 0.6 muon (t quarks only). Decay products of K_s are included in the pions and photons.

(a)	$\langle p \rangle$ (GeV/c)	Median p GeV/c	$\langle n \rangle$	(b)	$\langle p \rangle$ (GeV/c)	Median p GeV/c	$\langle n \rangle$
γ	1.14	0.30	21.8	γ	0.68	0.32	32.6
$e^{\pm}$	1.72	0.40	0.4	$e^{\pm}$	2.30	0.95	1.0
$\mu^{\pm}$	0.90	0.35	1.2	$\mu^{\pm}$	1.20	0.41	2.5
$\pi^{\pm}$	2.45	1.03	16.4	$\pi^{\pm}$	1.42	0.77	26.0
$K^{\pm}$	4.19	2.00	2.8	$K^{\pm}$	2.20	1.36	4.2

B. Global Detector Parameters

1. Solid Angle

For the 2-jet events, the angular distribution of the primordial quarks with respect to the beams is approximately $1 + \cos^2\theta$. The effects of incomplete solid angle coverage can thus be estimated analytically, rather accurately, for the more frequent two-jet topologies, as the jets have limited opening angles around the quarks' momenta. The Monte Carlo calculation of the inefficiency[9] due to imperfect polar angle coverage corroborates this rule-of-thumb. The solid angle issues concerning 3-jet events are further discussed in Section E.2. Because of the particle collimation alluded to before, a detector of limited solid angle may still register complete events part of the time. Figure 8[7] shows the fraction of events for which the ratio of measured energy to center-of-mass energy

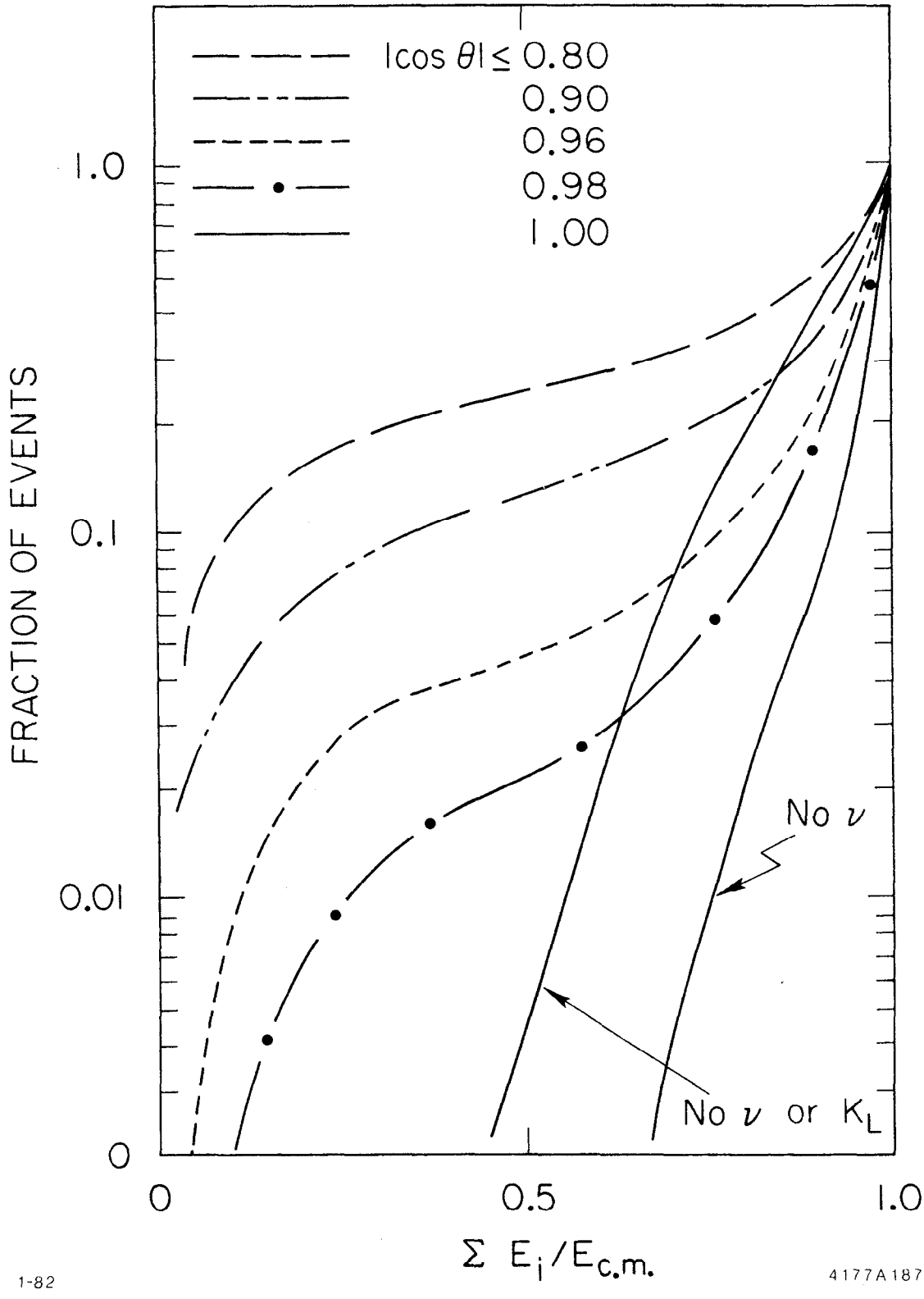

Fig. 8. Fraction of events for which the ratio of measured energy to center-of-mass energy is less than a given abscissa, for detectors of perfect energy resolution and the indicated solid angles. The energy carried away by neutrinos results in a finite energy loss even in the 4π sr case.

is less than a given abscissa, for detectors of increasing solid angle coverage from $\cos\theta = 0.8$ to $\cos\theta = 1.0$. The detector is a perfect calorimeter that misses only the neutrino energy, about 2% of the total energy.

2. Segmentation

The ability to distinguish the many particles composing a jet is limited by both fundamental and practical considerations. Particles in a jet are correlated in energy and space,[10] those carrying high momentum being more closely associated in space. This effect is evident by comparing Fig. 9, which shows the angle of different particles relative to the quark direction, with the same distribution weighted by the fractional momentum $x = p/E_b$ of each particle, Fig. 10.[7] In tracking chambers, charged particles closely correlated in energy and direction may be difficult to resolve. Similarly, in shower counters and calorimeters, the lateral extension of the showers[11] preclude their resolution if separated by a distance comparable to their natural radii. In both tracking chambers and calorimeters, very fine segmentation results in a large number of components and readout channels, and in high costs. Clearly, the segmentation needed for a particular measurement is one of the most critical parameters of a detector.

2.1 Tracking Chamber Segmentation. The power of a drift chamber[12] to resolve the charged particles of a jet depends on the effective confusion distance applicable at the pattern recognition stage of data reduction, where hits from two tracks separated by at least this distance must be recognized as belonging to distinct particles. This distance is not directly related to the cell size, but is more closely related to the inherent precision of the chamber. It is, in fact, that level of accuracy available at the pattern recognition stage of the analysis.

In the most common detector design, namely, a cylindrical tracking chamber immersed in a solenoidal field, the ability of the pattern recognition to separate tracks depends largely on the "x - y" information provided by the axial wires: they give the projected hits on a plane perpendicular to the beams. This follows from both the jet collimation and the poorer space resolution along the "z" axis, usually obtained from off-axis small angle stereo or from charge division. For these chambers a single

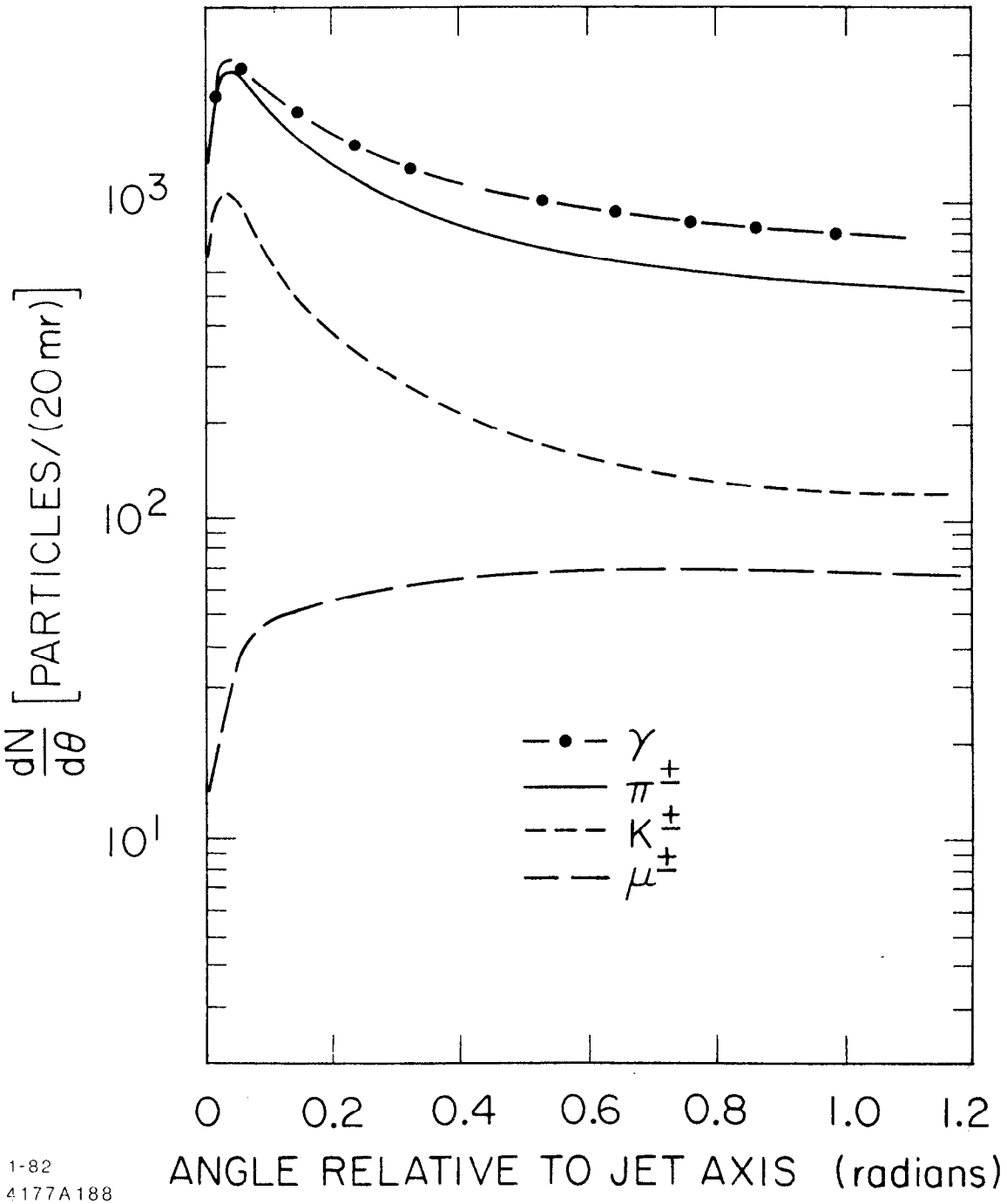

Fig. 9. Distribution of the angle with respect to the jet axis for different particle species.

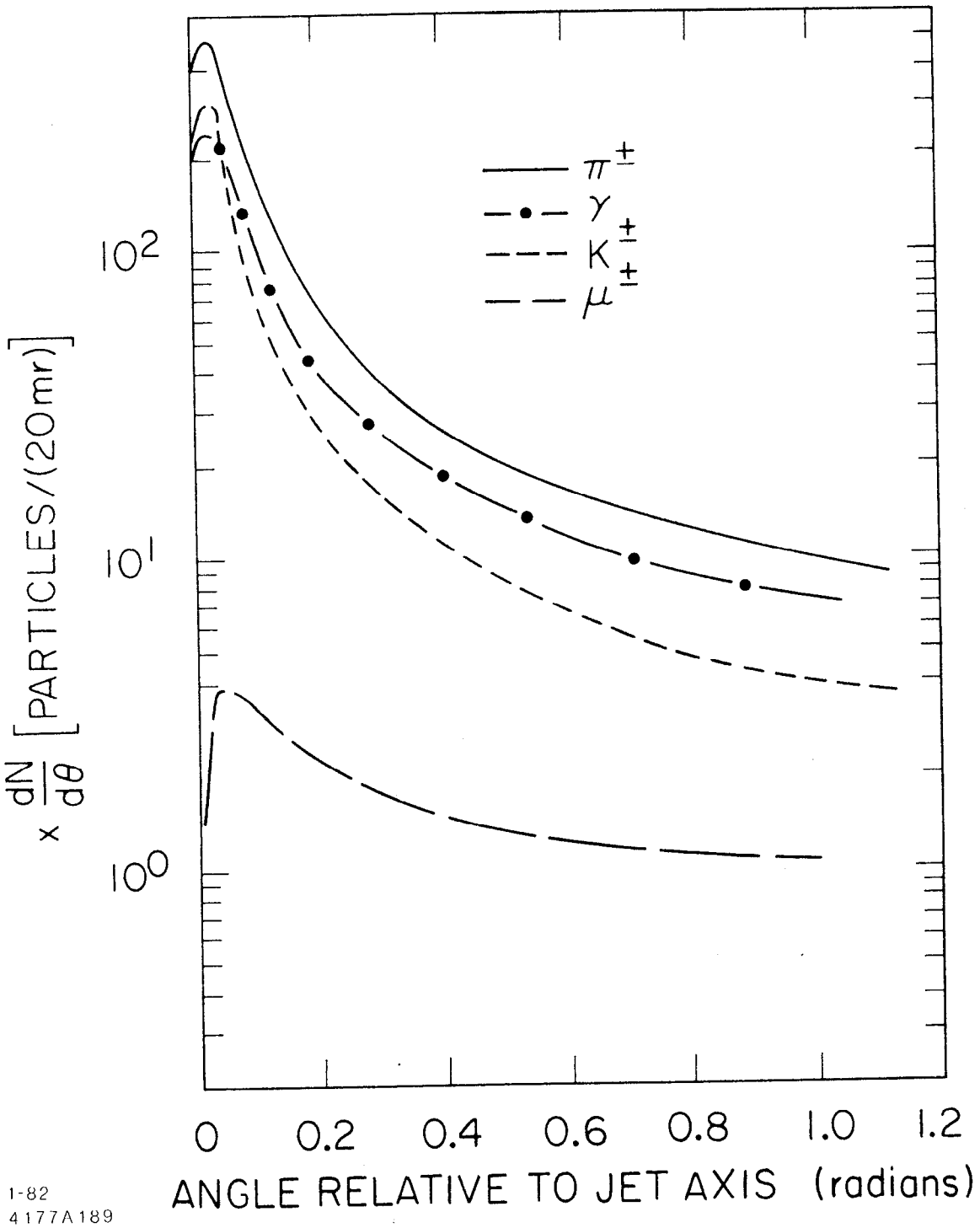

Fig. 10. Distribution of the angle with respect to the jet axis, weighted by the fractional momentum of each particle, for different particle species.

confusion distance in the x - y plane can be used to parameterize the performance. For time-projection chambers (TPC), the confusion distances in x - y and z are nearly the same and both measurements play an important role in the pattern recognition. The efficiency of track finding algorithms has been estimated by use of these ideas. A track is considered reconstructable if separated from all its neighbors by no less than the confusion distance in at least a given number of axial layers[9] or over at least half the radial extent of the detector.[12] Typical results for the latter definition appear in Table II for a cylindrical detector of inner radius 0.3 m, outer radius 1.5 m and magnetic field B = 5 kG. A cut on polar angle has been applied to eliminate solid angle effects. The efficiencies are highest at low momenta and lowest at intermediate momenta (5-15 GeV/c). For low momenta, the correlations to other tracks are less important. At the upper end of the momentum spectrum, the probability of another relatively energetic track nearby is reduced by conservation of energy. Thus, the intermediate momenta pose the greatest problem. Notice that 80% of the tracks are in the lowest two momentum bins: the average reconstruction efficiency would represent too optimistic a view of chamber performance in the medium-momentum range. The reconstruction efficiency decreases by about 1-2% for a reduction of the mean chamber radius of 10 cm. From Table II, high tracking efficiency implies a design confusion distance of about 2.5 mm or better for a drift chamber. The corresponding TPC parameters appear to be 1-2 cm. in x - y and in z, but will be more reliably estimated after gaining experience in the operation of the TPC.

An immediate consequence of the imperfect track reconstruction efficiencies is that the total energy carried by the charged jet components usually cannot be reconstructed. The last part of Table II gives the fraction of two-jet events in which more than 80% of the energy carried by charged particles can be measured. A solid angle cut eliminates the forward and backward cones ($|\cos\theta| > 0.85$) of poor measurements.

Related to the pattern recognition discussion is the issue of curling tracks:[9] particles of sufficiently low momentum may produce helical trajectories, in the solenoidal field, which are fully contained in the chamber volume. These curling tracks confuse the pattern recognition.

Table II

Performance of drift chambers as a function of the confusion distance applicable at the pattern recognition stage of data analysis. Other chamber parameters are R_i = 0.3 m, R_o = 1.5 m, length 3m, B = 5 kG. Tracks are reconstructible if separated from all their neighbors by more than ε_1, in the x - y projection (and ε_2 in the z projection) over at least half of the radial extent of the drift (TCP) chamber. The top part of the table refers only to those tracks that do not go out the ends of the detector. For the two-jet events the jet axis fulfills $|\cos\theta| < 0.85$. No such cuts have been applied to the three-jet events.

Reconstructed Fraction of Tracks

Momentum (GeV/c)	Conventional Drift Chambers			TCP Type
	ε_1 = 1 cm	5 mm	2.5 mm	ε_1 = 2 cm, ε_2 = 2 cm
0 - 2	0.92	0.97	0.99	0.98
2 - 4	0.82	0.94	0.99	0.97
4 - 6	0.76	0.93	0.98	0.95
6 - 8	0.74	0.91	0.98	0.93
8 - 10	0.70	0.88	0.97	0.88
10 - 12	0.74	0.89	0.98	0.91
12 - 14	0.75	0.92	0.98	0.91
14 - 16	0.76	0.89	1.00	0.86
16 - 18	0.87	0.93	0.97	0.88
>18	0.79	0.92	0.97	0.91

Fraction of Events With at Least 80% of the Charged Particle Energy Reconstructed

Event Type	Conventional Drift Chambers			TPC Type
	ε_1 = 1 cm	5 mm	2.5 mm	ε_1 = 2 cm, ε_2 = 2 cm
2-jet	0.50	0.78	0.91	0.83
3-jet	0.44	0.64	0.72	0.69

In a 2 m radius, 4 kG field, detector, the jets produce a curling track every third event. Increasing the magnetic field to 8 kG while reducing the radius to 1.4 m results in one such track every second event. If the photon component of the jet interacts in 10% of a radiation length prior to entering the tracking chamber, the number of curling tracks increases to about 1-2 per event in both configurations.

2.2 Calorimeter Segmentation. While charge and momentum alone suffice to describe the trajectory of a particle, the shower it generates depends, in addition, on its identity and on the specific type of calorimeter used. The design goals of a calorimeter include lepton-hadron separation, as well as energy and direction measurements. Both lateral and longitudinal (depth) segmentations are relevant here. Lateral segmentation determines the angular resolution and affects the pattern recognition. Longitudinal segmentation provides an additional view of the shower development, of consequence for both the particle identification and pattern recognition. Calorimeters made of homogeneous media (lead-glass, NaI) present the so-called tower geometry, with built-in lateral segmentation. Separate function calorimeters, with abrupt density changes at the boundary between the radiator and sampling materials, can be built in strip configuration as well, with consecutive strip layers oriented differently to permit the spatial location of the shower. For both types of systems, the particle identification and pattern recognition problems depend crucially on whether the calorimeter has been preceded by a tracking chamber measuring the positions and momenta of the charged particles. Although the correct analysis of the calorimeter segmentation must consider systems as a whole, useful, albeit partial, results are presented below. The complexities of calorimeter design are beyond the scope of this parametric study.

Particle showers develop around the initial particle direction. In electro-magnetic calorimeters the one-standard-deviation lateral containment distance is given by the Molière radius $r_M = K/\varepsilon$ in radiation lengths units,[11,13] where K, the scattering energy, is about 20 MeV and ε is the critical energy of the radiator. Characteristic values of r_M are 1.6 cm in Pb, 2.3 cm in BGO, and 4.4 cm in NaI. For the purpose of resolving particle overlaps, r_M indicates the limit of the useful segmentation of

an electromagnetic calorimeter. However, a segmentation distance s that assures that the shower energy is distributed in several calorimeter elements yields a spatial resolution $\sigma << s$, since the impact point can be calculated from the centroid of the energy deposition. A model calculation[14] gives $\sigma = cs\ \Delta E/E$ where $c = 0(1)$. The same model gives the single photon reconstruction efficiencies, integrated over photon energy, as a function of the number of elements in tower or strip systems covering 4π sr at a distance of 1.5 m from the interaction point. The results appear in Fig. 11. The inefficiencies are due to a lower energy cut-off of 0.2 GeV and to the effect of particle overlaps which yield a wrong energy measurement.

The ability of reconstruction of jet π^o's depends on the distance of the two photons at the calorimeter and on the overlap with other particles of the jet. The average number of particles whose impact point on a calorimeter is within a given distance from the impact point of the most energetic particle of the jet appears in Fig. 12.[15] Further assumptions are explained in the figure caption. It is seen that, at a 1.5 m radial distance from the interaction point, two of the six most energetic photons of the jet are separated by less than 5 cm when the leading particle is a photon. The invariant mass of photon pairs[16] is shown in Fig. 13 for 0.1 and 1.0 GeV lower energy cut-offs and for different energy and angle resolutions. For the best case resolutions of $0.1\ \sqrt{E}$ and 5 mr, and $E_\gamma > 1$ GeV the signal-to-noise ratio is about 1.

Particle overlaps can invalidate the comparison of momentum and energy, used for electron identification. Table III[16] shows the average number of additional particles in a solid angle of 2 msr, centered around the impact point of an electron or a photon on the front of a 1.5 m radius calorimeter in a 5 kG solenoidal field. It was found that the results are nearly proportional to solid angle up to the quoted values, and that they grow slower beyond 2 msr. Thus, in order to have an extra particle in no more than 10% of the cases for photons above 1 GeV it is necessary to achieve $\Delta\phi \simeq \Delta\theta \simeq 10$ mr.

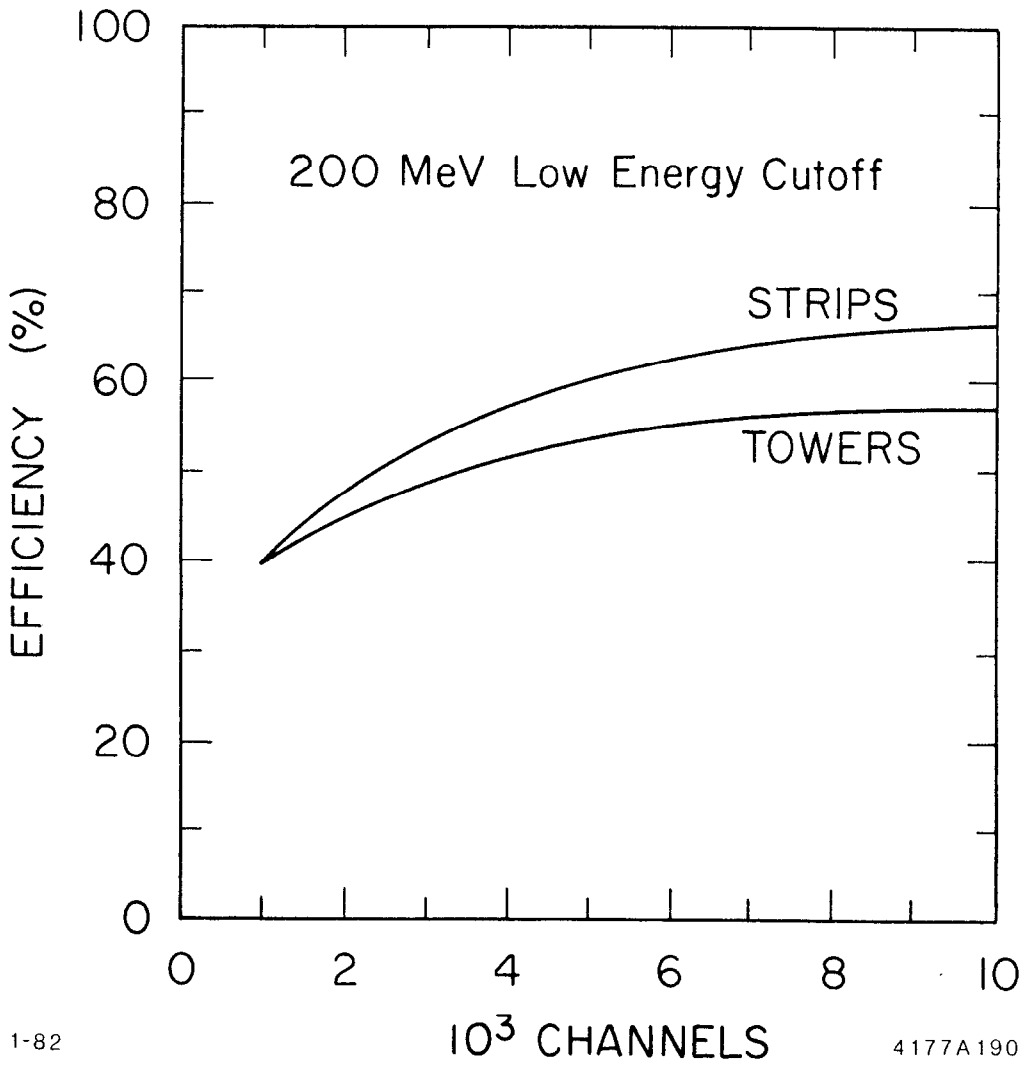

Fig. 11. Single photon reconstruction efficiency, averaged over the photon energy spectrum, as a function of the number of readout channels of strip- or tower-configuration calorimeters.

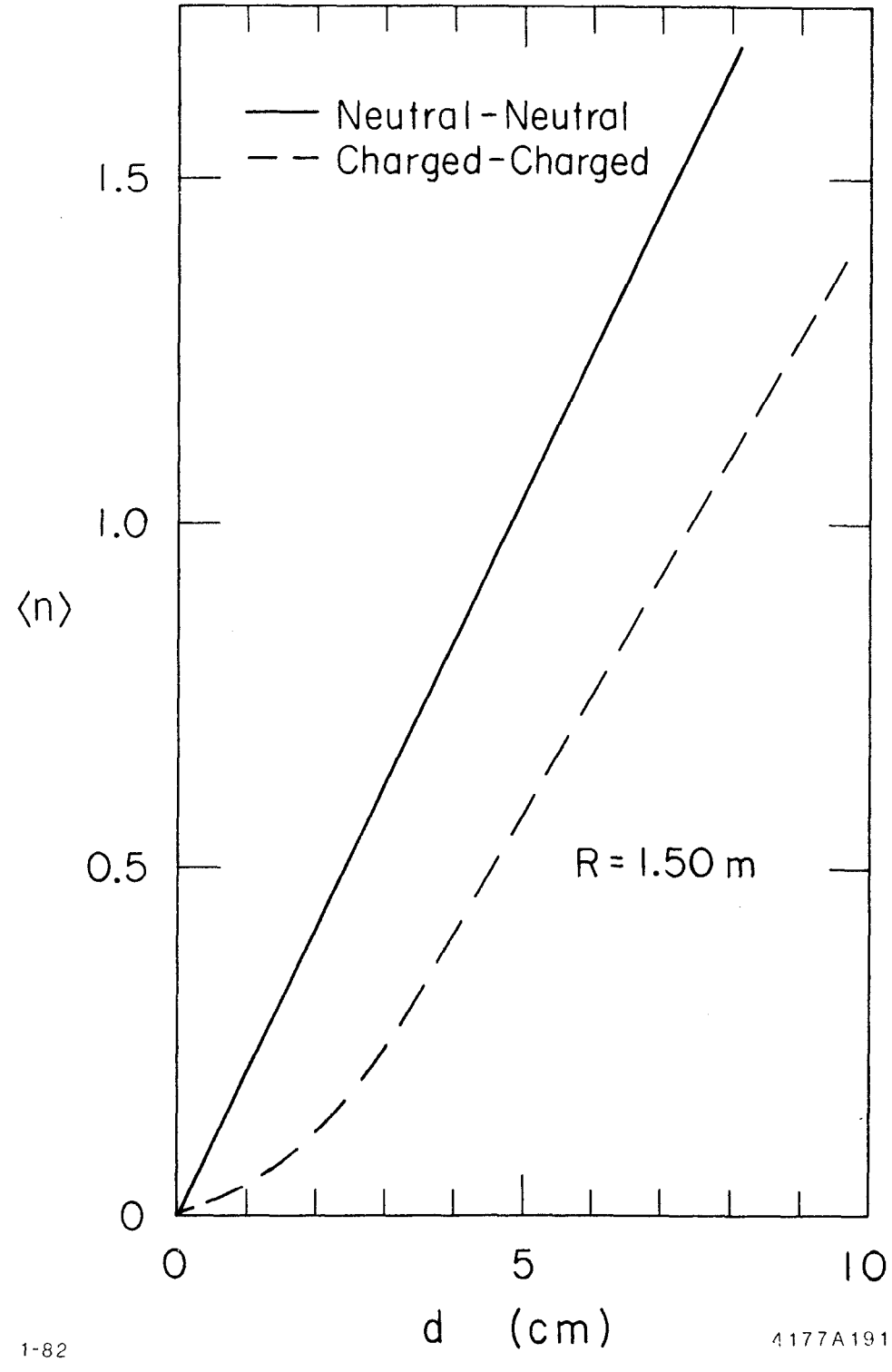

Fig. 12. The average number of particles, chosen from among the five most energetic particles after the leading one, versus the distance of their impact point from the impact point of the jet leading particle on a cylinder of radius 1.5 m and length 3 m. The solid curve is for leading photons and the trailing five most energetic photons. The broken curve is for a leading charged particle and the trailing five most energetic charged particles, in a 5 kG solenoidal field.

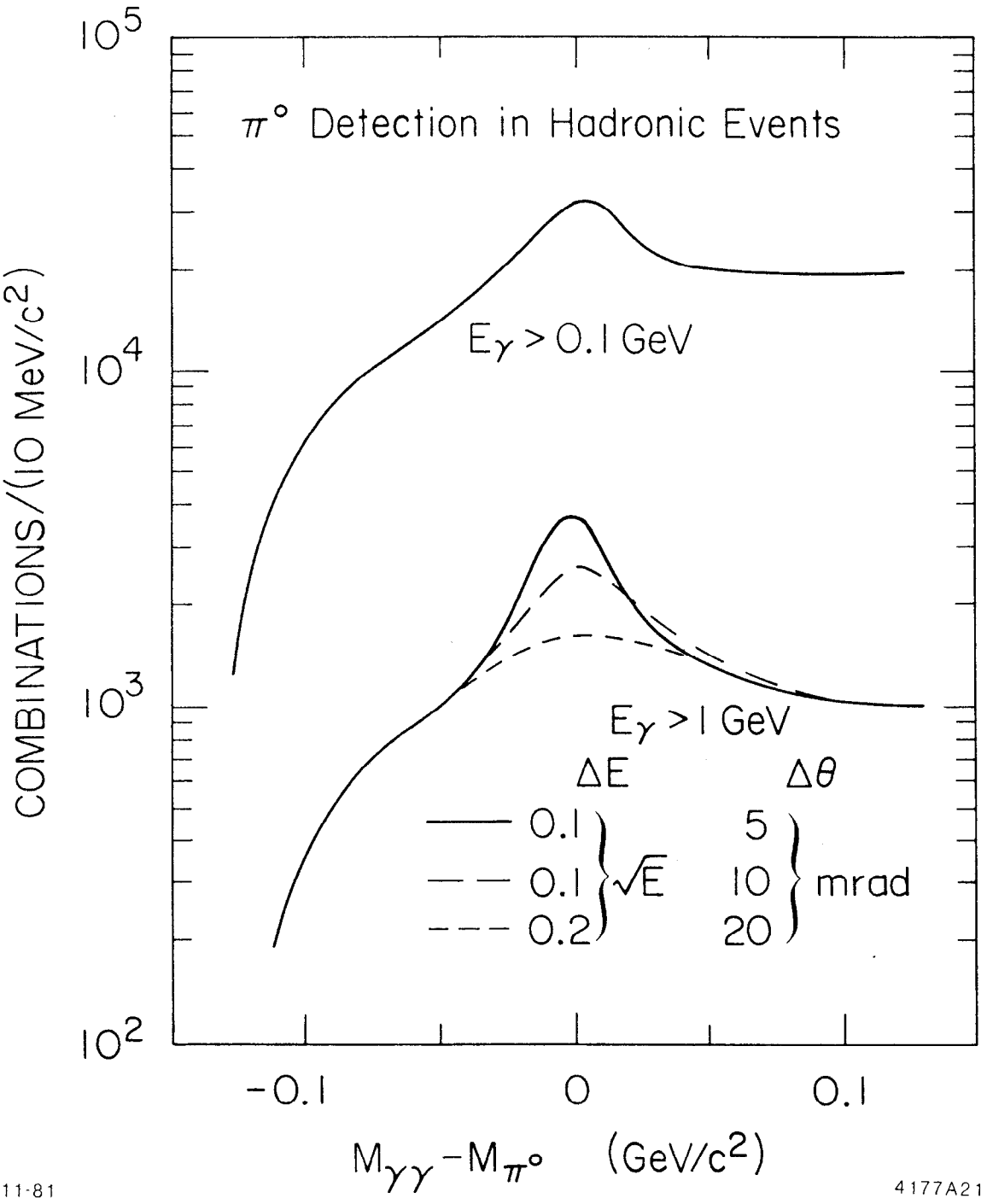

Fig. 13. The invariant mass of detected photon pairs for various lower energy limits, and energy and angle resolutions.

Table III

Average number of extra particles within a cone of half opening angle of 25 mr with respect to the incident electron or photon.

	Initial Particles			
	Electron		Photon	
Confusing Particles	all	E > 1 GeV	all	E > 1 GeV
All	0.17	0.25	0.21	0.59
Electron or Photon	0.08	0.13	0.13	0.39
Electron or Photon $E > 0.1\ E_{initial}$	0.08	0.13	0.13	0.37
Hadrons	0.07	0.11	0.08	0.20

C. Secondary Particle Decays

1. Segmentation of Vertex Detectors

The short-lived Z^o decay products will create secondary vertices close to the interaction region. Typical mean decay lengths of the τ lepton and of charm, and perhaps bottom, states are measured in millimeters. Suitable devices may permit to reconstruct some of these decays and hence tag τ's and heavy quarks, measure lifteimes, and possibly find the initial quark flavor. The SLC offers a promising environment for these studies; since the beam bunch lateral spread is measured in microns, it should be possible to place detectors at radii as small as 1 cm from the interaction point.

The segmentation of vertex detectors should be finer than that of the main tracking chamber. The probability that a D meson decay track, in a $c\bar{c}$ event, will overlap with any other track of the event[17] appears in Fig. 14 as a function of the confusion distance for a cylindrical detector of 1 cm radius coaxial with the beams. This detector could be a solid state device. The two curves in Fig. 14 refer to detectors segmented only in ϕ ("1 - D") or in ϕ and z ("2 - D"). Resolving probabilities of 90% are achieved for "1 - D" ("2 - D") resolution of about 60 μm (200 μm).

The criteria of track reconstruction efficiency used for the tracking chamber have been applied also to a vertex drift chamber[12] of inner and

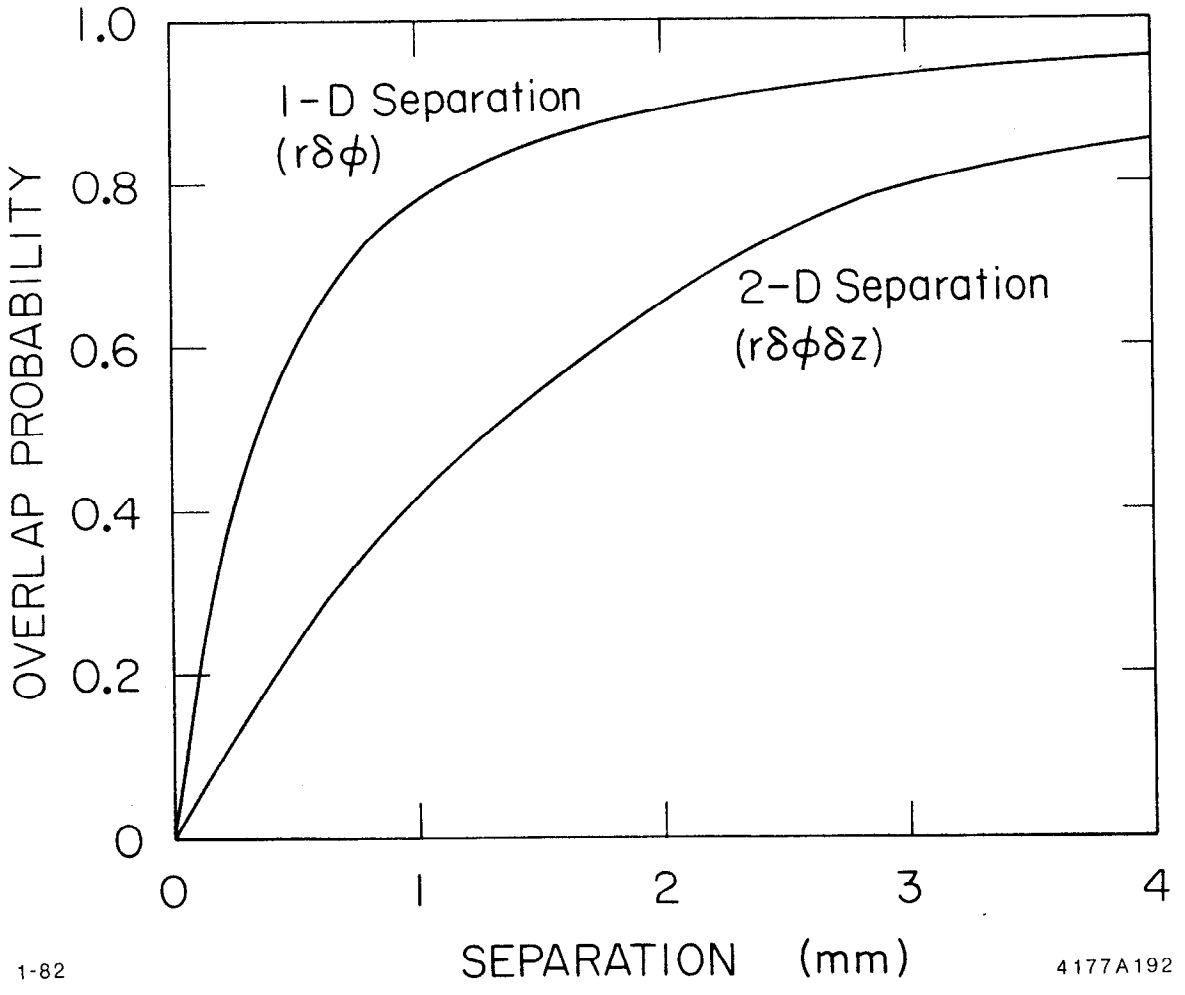

Fig. 14. The probability that a D meson decay track, in a $c\bar{c}$ event, overlaps with any other track of the event as a function of the double hit resolution at 1 cm from the interaction point. The curve labelled "1-D" refers to a cylindrical detector segmented only in azimuth, the "2-D" one is for a detector segmented longitudinally as well.

outer radii of 10 and 30 cm respectively. The efficiencies appear in Table IV. Excluding the lowest momentum bin, the efficiency is about 90% (95%) for 1 mm (.5 mm) confusion distance.

The 90% reconstruction efficiency in the solid state device discussed above corresponds to a resolution of $\delta\phi \simeq 6$ mr. Approximately the same $\delta\phi$ value, for 90% reconstruction efficiency, is given by the ratios of the appropriate confusion distances for the vertex drift chamber (Table IV) and for the tracking chamber (Table II) to the respective chamber mean radius. It thus appears that the required confusion distances scale linearly with radius.

Table IV

Performance of vertex drift chambers as a function of the confusion distance applicable at the pattern recognition stage of data analysis. Other chamber parameters are R_i = 0.1 m, R_o = 0.3 m, length 3 m, B = 5 kG. Tracks are reconstructible if separated from all their neighbors by more than ε_1 in the x - y projection over at least half of the radial extent of the chamber. The table refers to those tracks that do not go out the ends of the detector.

Momentum (GeV/c)	Reconstructed Fraction ε_1 = 2.5 mm	1.0 mm	0.5 mm
0 - 2	0.87	0.97	0.99
2 - 4	0.75	0.91	0.97
4 - 6	0.69	0.88	0.94
6 - 8	0.67	0.86	0.92
8 - 10	0.63	0.85	0.93
10 - 12	0.67	0.83	0.91
12 - 14	0.67	0.88	0.94
14 - 16	0.68	0.85	0.95
16 - 18	0.73	0.95	0.98
> 18	0.75	0.95	0.99

2. Secondary Vertices

Tracks that originate in a secondary vertex do not extrapolate, in general, back to the interaction point: their finite impact parameters signal a decay vertex. The problem of tagging D decays with high resolution devices at small (~1 cm) radii has been considered.[17] The required resolutions for these tags imply that CCD arrays or high resolution bubble chambers will be required to do the measurements. The D's studied come from $c\bar{c}$ events only. The model vertex device consists of two cylinders of charge-coupled devices (CCD), each 200μ thick, placed at radii of 1 and 2 cm. The cylinders are 2 and 4 cm long, respectively. The resolution of the detector planes is the same in both transverse dimensions. Multiple scattering occurs only at the detector material, the multiple scattering in the beam pipe being neglected. Resolved tracks within the fiducial volume of the device are assumed to be tracked with 100% efficiency in the surrounding drift chambers. Figure 15 gives the impact parameter distributions of tracks from D decays and the rest of the tracks. In order to measure these short distances, the experimental resolution must be considerably smaller than the impact parameter. The resolution of each determination depends on the CCD array segmentation and on the given particle multiple scattering. Consider, for each D decay, the track with the largest impact parameter, and express the latter in terms of the estimated measurement error (one standard deviation units). The fraction of D decays with impact parameter larger than the abscissa appears in Fig. 16a, for the different resolutions indicated in the figure. Since some D's miss the detector, or yield no charged tracks in it, the distributions do not normalize at 1. It appears that the effectiveness of the detector is limited by the spatial resolution rather than by multiple scattering. A reasonable choice of parameters is given by a resolution of 10 μm and a thickness of 0.4% radiation lengths (curve E). The selection of largest impact parameter tracks 3 standard deviations or more away from the source gives about 50% of all D's. For the same choice of parameters, Fig. 16b gives the ratio of D decay tracks to all tracks in the event. The 3-σ sample has a signal to noise ratio of about 3:1. This ratio could be improved by the identification of charged kaons from D decay, for instance in a Čerenkov counter. The analysis of the impact

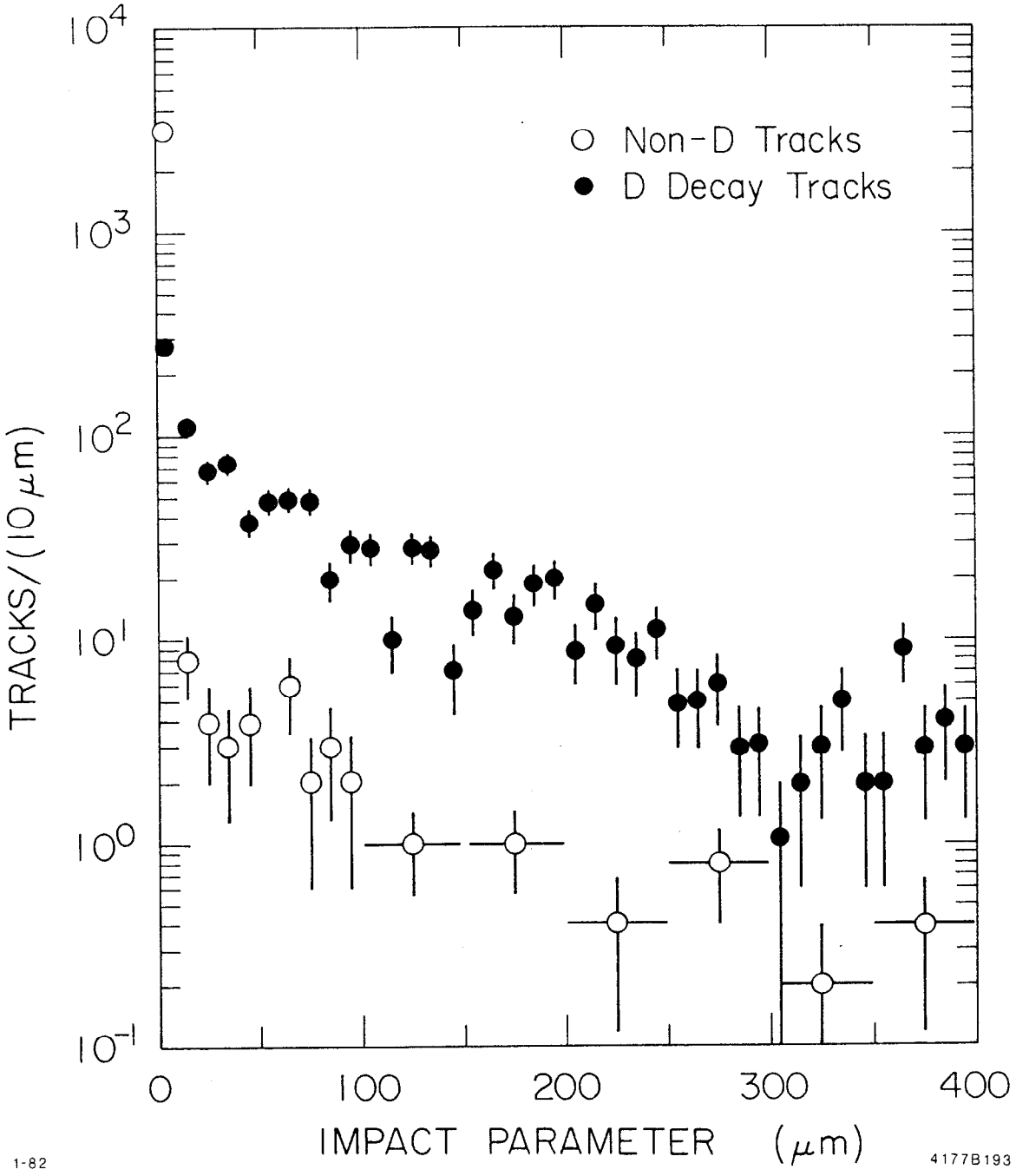

Fig. 15. Distribution of impact parameters of tracks from D decays and of the rest of the tracks, in $c\bar{c}$ events.

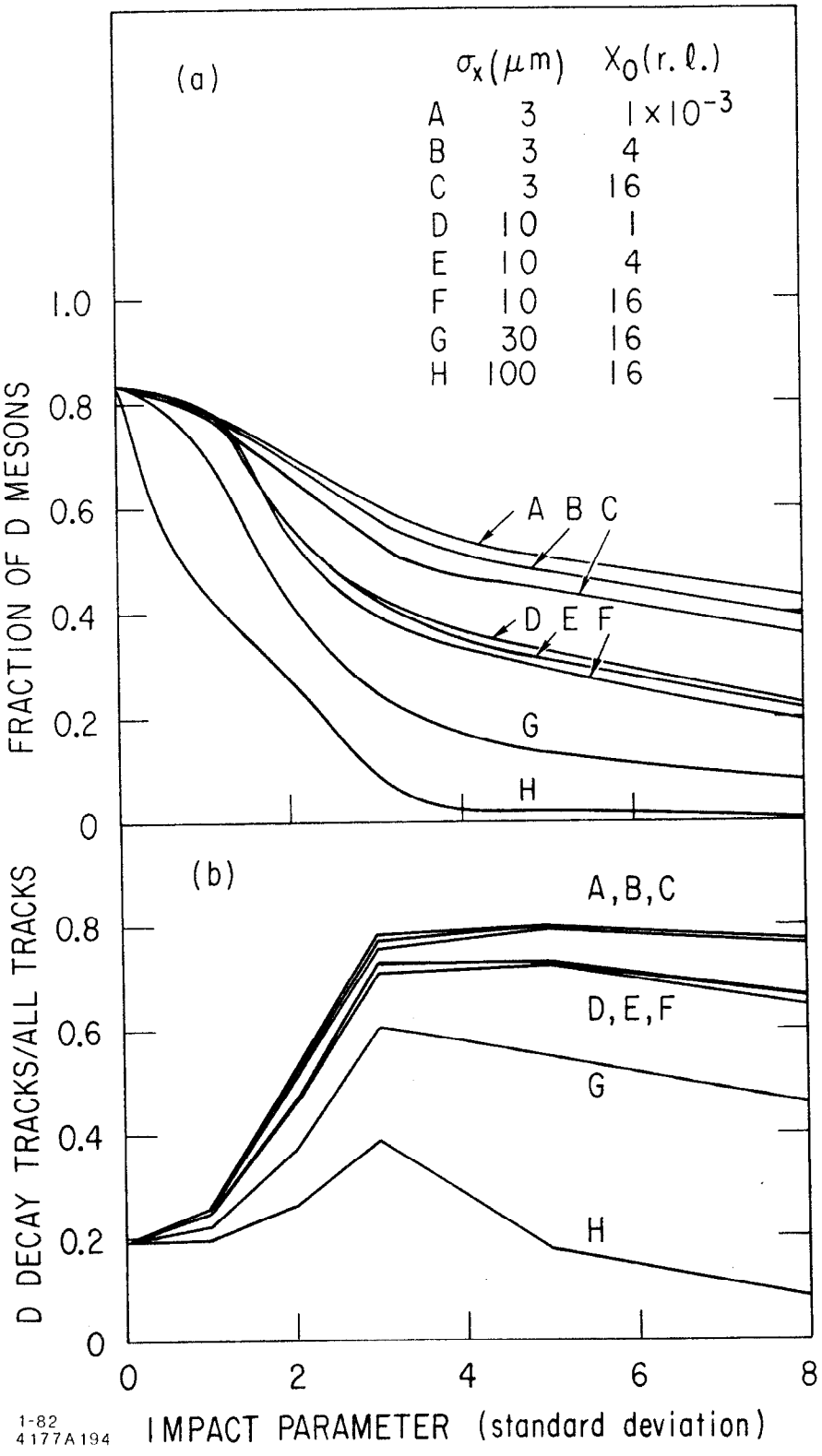

Fig. 16. (a) The fraction of D decays for which the largest impact parameter track is greater than the abscissa. For each entry in the plot, the impact parameter is expressed in terms of the estimated one-standard-deviation error of its determination. (b) The ratio of the number of D decay tracks with impact parameter larger than the abscissa to the number of all tracks fulfilling the same condition.

parameter of identified kaons shows that, with perfect particle identification, and for the resolution selected above, a 5-σ impact parameter cut will select 8% of all D's with negligible background.

The study of D decays tagged by finite impact parameters with respect to the production vertex appears feasible for a high resolution ($\simeq$10 μm) detector placed closely ($\simeq$1 cm) to the source. The actual reconstruction of the decay vertex may yield better discrimination against backgrounds than the single-track impact parameter method. This topic has not been studied yet.

3. Two-Body Invariant Masses

Without the benefit of a vertex tag the reconstruction of D mesons is difficult.[18] Figure 17 shows the two-body invariant mass of identified kaons and identified pions, for a momentum resolution of $\Delta p/p^2 = 0.003$ GeV^{-1} and perfect angular resolution. The various plots refer to the indicated pair total momentum. The largest signal-to-background ratio is about 1:2 in the interval $4 \leq p_{K,\pi} \leq 6$ GeV/c. This ratio does not improve significantly for $\Delta p/p^2 = 0.001$ GeV^{-1} and the signal disappears for $\Delta p/p^2 = 0.01$ GeV^{-1}. In the absence of particle identification there would be no signal regardless of momentum resolution. The identification of $K_s \rightarrow \pi\pi$ is easier. Again for $\Delta p/p^2 = 0.003$ GeV^{-1} but with $\Delta\alpha = 2$ mr, where α is the opening angle, Fig. 18 shows the invariant mass of particle pairs with total momentum above 8 GeV/c. The signal to noise ratio improves by $\simeq$10% for $\Delta p/p^2 = 0.001$ GeV^{-1}, and decreases by a factor of 2 for $\Delta p/p^2 = 0.01$ GeV^{-1}. An angular resolution of $\Delta\alpha = 5$ mr reduces the signal by about a factor of two as well.

D. Ancestor Quark Identification

1. Introduction

The measurement of the coupling constants of different quarks to the Z^o constitutes a stringent test of the models of weak interaction. The weak interaction production of the initial quark pair is as simple as the production of a stable lepton pair. However, the quark fragmentation products do not provide an unequivocal indication of the original quark flavor, thereby hindering the measurement of specific couplings. The same limitations apply to the current e^+e^- experiments: after a

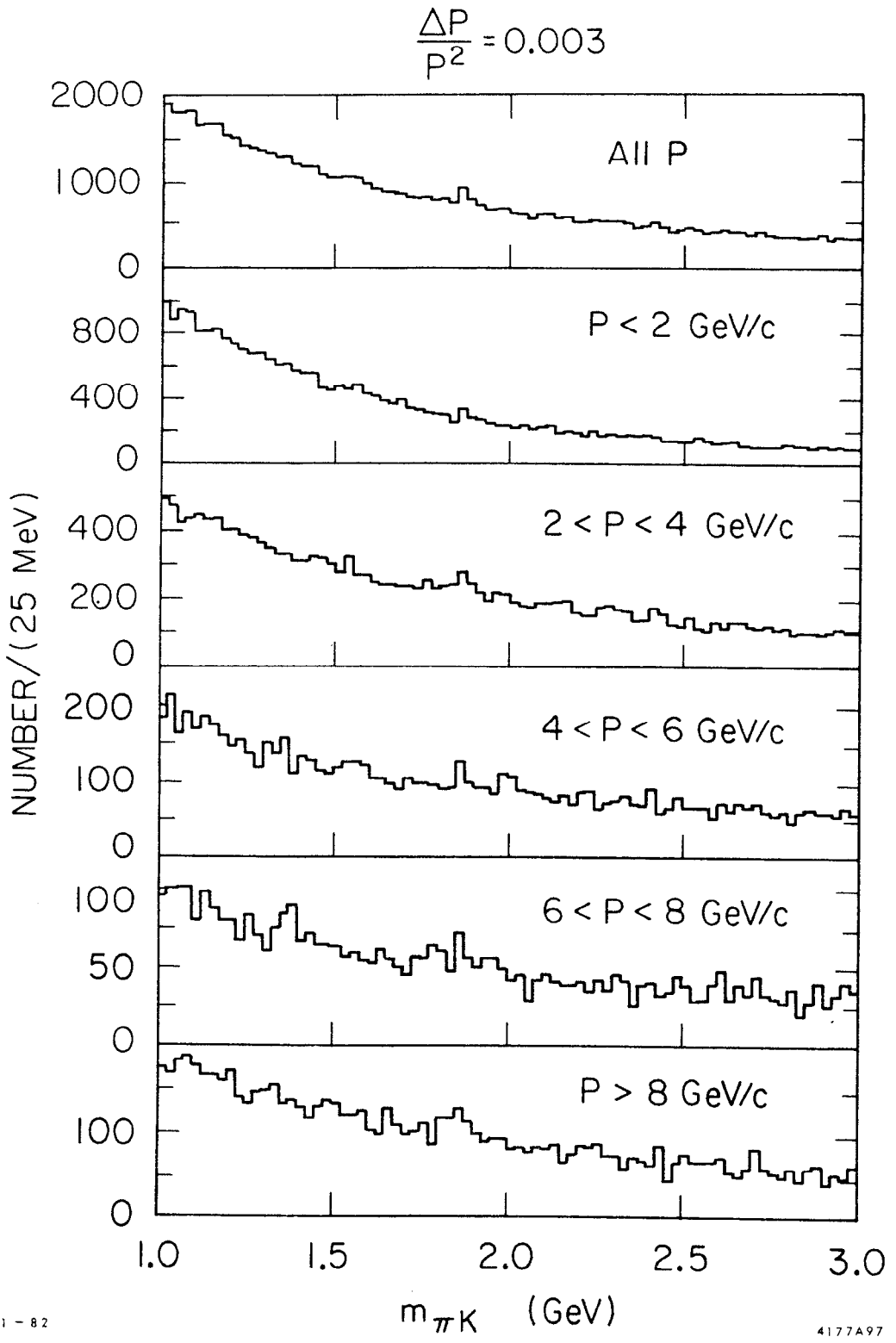

Fig. 17. The invariant mass of all opposite-charge pion-kaon pairs in a jet, for various pair momentum intervals and momentum resolution $\Delta p/p^2 = 0.003$.

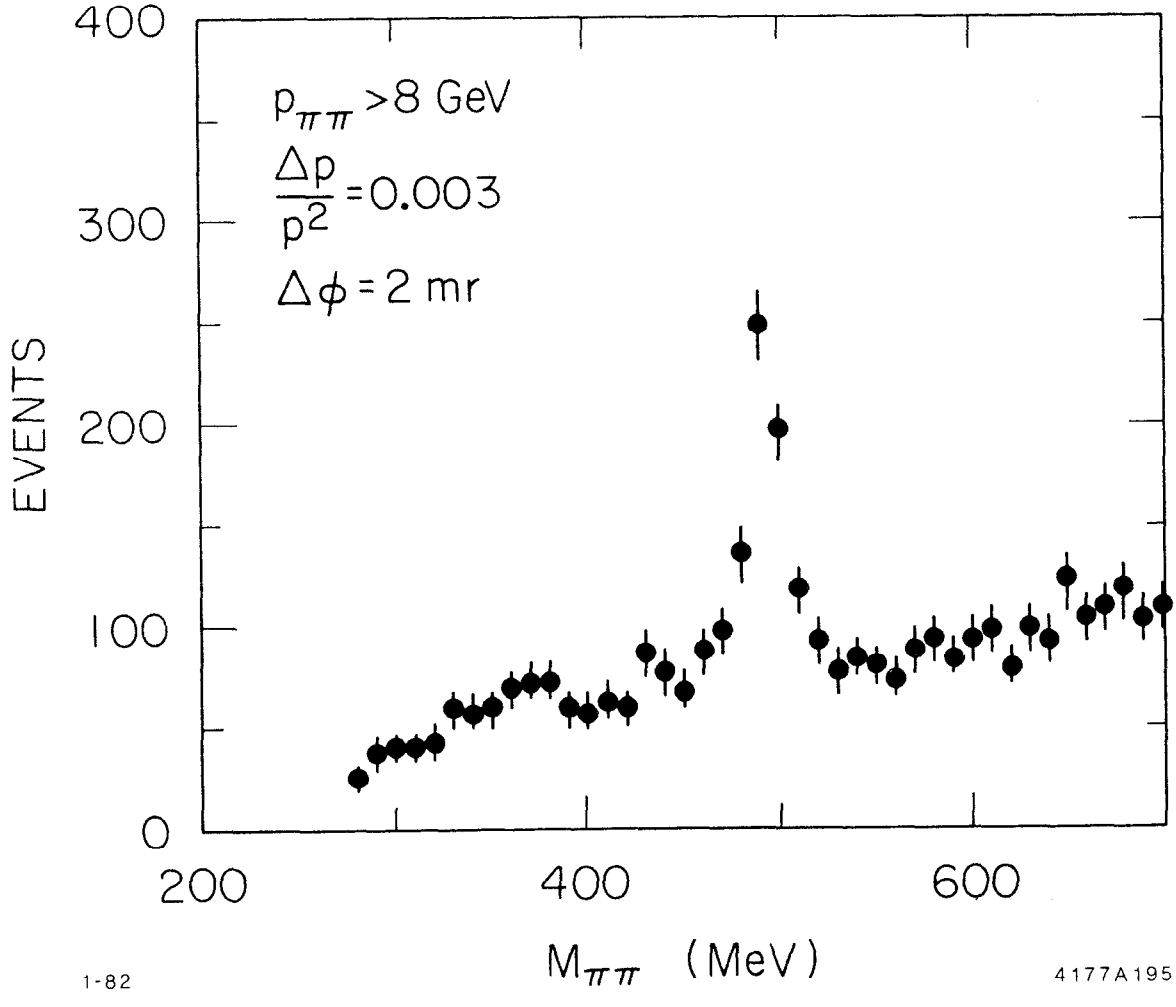

Fig. 18. The invariant mass of all opposite-charge pion pairs, with pair momentum above 8 GeV/c, and the indicated experimental resolutions.

decade of electron-positron experiments, there is no direct experimental proof that, for instance, the up and strange quark couplings to the photon are each proportional to the quark charge. What has been measured, instead, is the ratio R, an average of the squares of the electromagnetic coupling constants. In the case of the more complex coupling structure of the weak neutral current, which in addition to charge depends on the weak isospin and helicity of the quark, there are even more compelling reasons to attempt to identify the primordial quarks of the event.

The fragmentation process appears to dilute the correlation between the quark flavor and the observed particles' identity: the jet leading particle frequencies of occurrence are rather similar for all quark flavors, as shown by Table V,[19] with the exception of kaons-s quark and lepton-heavy quark correlations. The momentum distribution of leading particles, for different quark flavors, do not enhance the ancestor quark identification, save that kaons from s-quark jets contribute dominantly to the higher momenta, as shown in Fig. 19. The average particle composition of jets, for each quark flavor separately, appears in Table VI. Only the top quark results appear different from the almost uniform values of the other flavors. In the following paragraphs these limited correlations found are further explored: a discussion of shape parameters will show that it is possible to isolate a fraction of the t-quark events, with similar conclusions attained by detecting leptons with high transverse momentum with respect to the jet axis. This section closes with a discussion of experimental methods to estimate the top quark mass, and a summary.

2. Shape Parameters

In order to estimate the effectiveness of shape parameter cuts on the data it is necessary to indicate the resolution with which they are measured. The model detector assumed[20] consists of a central tracking chamber with 86% solid angle coverage and $\Delta p/p^2 = 0.005\ GeV^{-1}$. An electromagnetic calorimeter with $\Delta E/E = 15\%/\sqrt{E}$ surrounds the cylindrical chamber in all directions, with a 98% solid angle coverage. Its segmentation is into 5 cm wide strips.

Table V

Leading particle frequency of occurrence, in per cent, as a function of the ancestor parton flavor. The leading particle is the most energetic stable particle of the jet. The kaon entries refer to charged kaons, and to a fraction of the K_S's: if the latter decay within 10 cm of the interaction point, their decay products are included in the photon and pion entries; if the decay occurs between 10 and 50 cm of the interaction point, they are counted as kaons; and if the decay occurs beyond 50 cm, the K_S and its decay products are not included in the table.

	u	d	c	s	t	b	g
γ	23	26	18	20	19	20	24
$e^{\pm}$			2		6	2.5	
$\mu^{\pm}$			2		6	2.5	
$\pi^{\pm}$	50	55	54	41	47	54	53
K	27	19	24	39	22	21	23

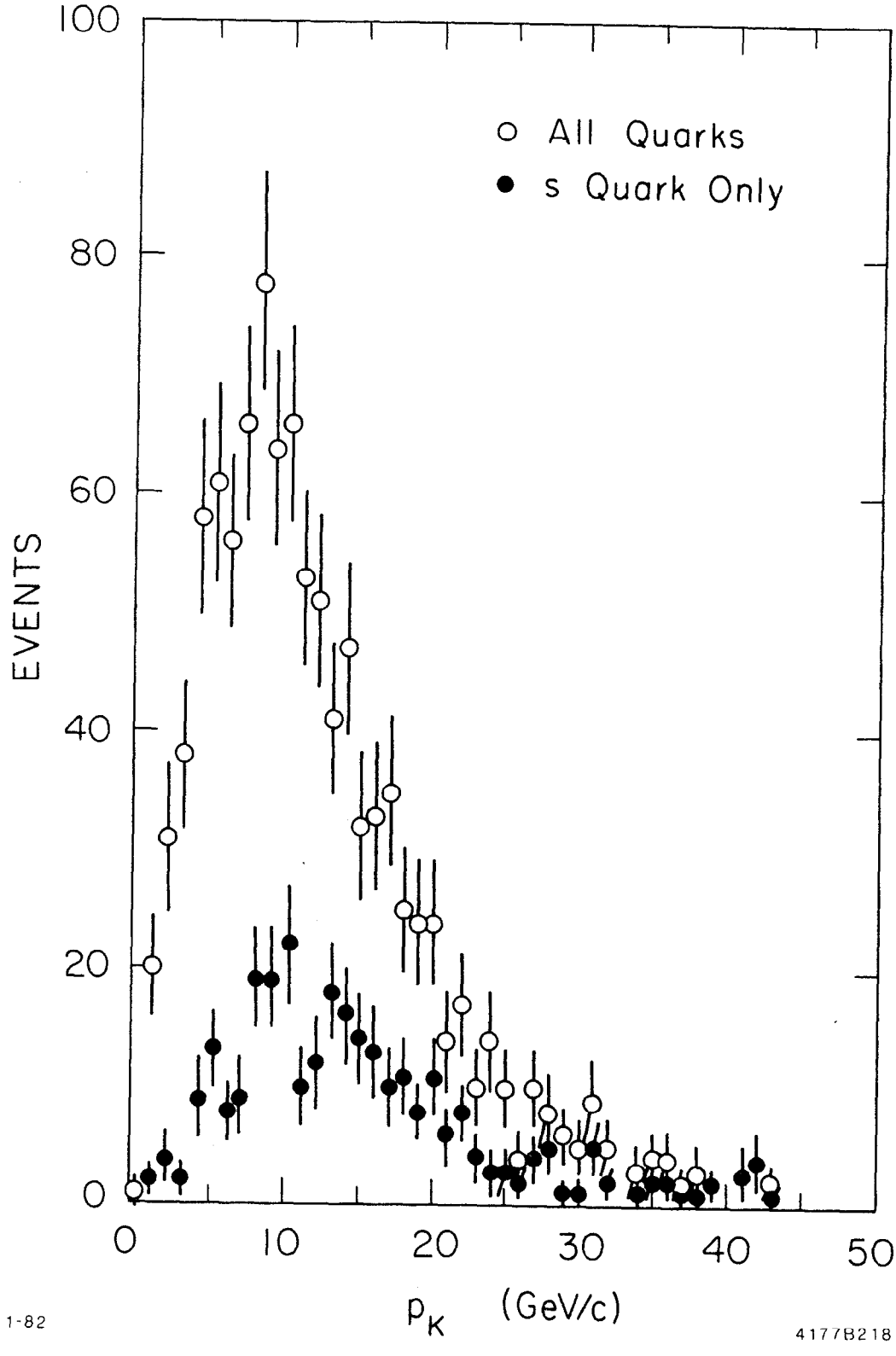

Fig. 19. The momentum distribution of those kaons that are the highest momentum particle of the jet, for all flavors combined (open circles) and for the s quarks only (closed circles).

Table VI

The average particle composition of jets, for each parton separately. The electron entries include Dalitz pairs and weak decays of charm, bottom, and top quarks. Only the latter decays contribute to the muon entries. The kaon entries refer to charged kaons and to K_S decaying in a spherical shell of inner and outer radii 1 and 50 cm, respectively, and thus deemed reconstructible. The number of jets considered is also indicated.

	u	d	c	s	t	b	g
γ	7.2	7.5	7.9	7.4	14.3	8.7	7.5
$e^{\pm}$	0.08	0.1	0.18	0.08	0.5	0.26	0.09
$\mu^{\pm}$	0	0	0.08	0	0.3	0.14	0
$\pi^{\pm}$	5.5	5.6	5.7	5.2	11.6	6.8	5.6
K	1.7	1.5	1.9	2.2	3.3	2.0	1.6
Total Average Multiplicity	14.5	14.7	15.7	15.7	30	17.9	14.8
Number of Jets	504	660	536	752	526	606	568

The sphericity variable[21,22] is a quantitative measure of the degree of collimation of the particles along an internal event axis. The sphericity distribution arising from up, down, charm, strange, and bottom quarks, Fig. 20a, can be compared to that from the top quark, Fig. 20b. Events with gluon emission, $q\bar{q}g$ and $q\bar{q}gg$, also contribute to these graphs. A selection of $t\bar{t}$ events based on sphericity will not achieve a good signal to noise ratio.

The aplanarity variable measures the deviation of the event particles from a plane. The comparison of aplanarity distributions for the two groups of quarks defined above appears in Figs. 21a and 21b. An aplanarity cut alone does not yield a rich sample of $t\bar{t}$ quark events: A cut at aplanarity ≥ 0.04 gives a signal-to-background ratio of 1.6:1. The major background arises from lighter-quark gluon radiative events. However, the latter $q\bar{q}g$ and $q\bar{q}gg$ events can be isolated, with high efficiency, by a cluster analysis[23] and thus eliminated from the sample. Consider then a sample of events which contain only two clusters, and with aplanarity larger than 0.04. The correlated distribution of jet masses appears in Fig. 22a for top quark events and in Fig. 22b for the lighter quarks. In the region above 10 GeV masses, the top quark signal to background ratio is 4:1 with a t tag efficiency of 20%. It should be noticed that the sample of events obtained is kinematically biased by the cluster analysis, aplanarity selection, and mass cuts. Due caution is necessary in the interpretation of top quark jet properties derived from such a sample, which depend on the model assumptions. Nonetheless, the t tag rate obtained by use of this method is several hundred per day for a luminosity of 3×10^{30} $cm^{-2}s^{-1}$.

3. High Transverse Momentum Leptons

Decay leptons carry away, in the rest frame, an energy proprotional to the mass of the parent particle. High momentum leptons have been used successfully to tag the production of heavy quarks in hadron, neutrino, and e^+e^- interactions. It appears that μ's and e's will fulfill their traditional role also in the Z^o experiments.

The distribution of muons[24] as a function of the square of their transverse momentum with respect to the primordial quark momentum

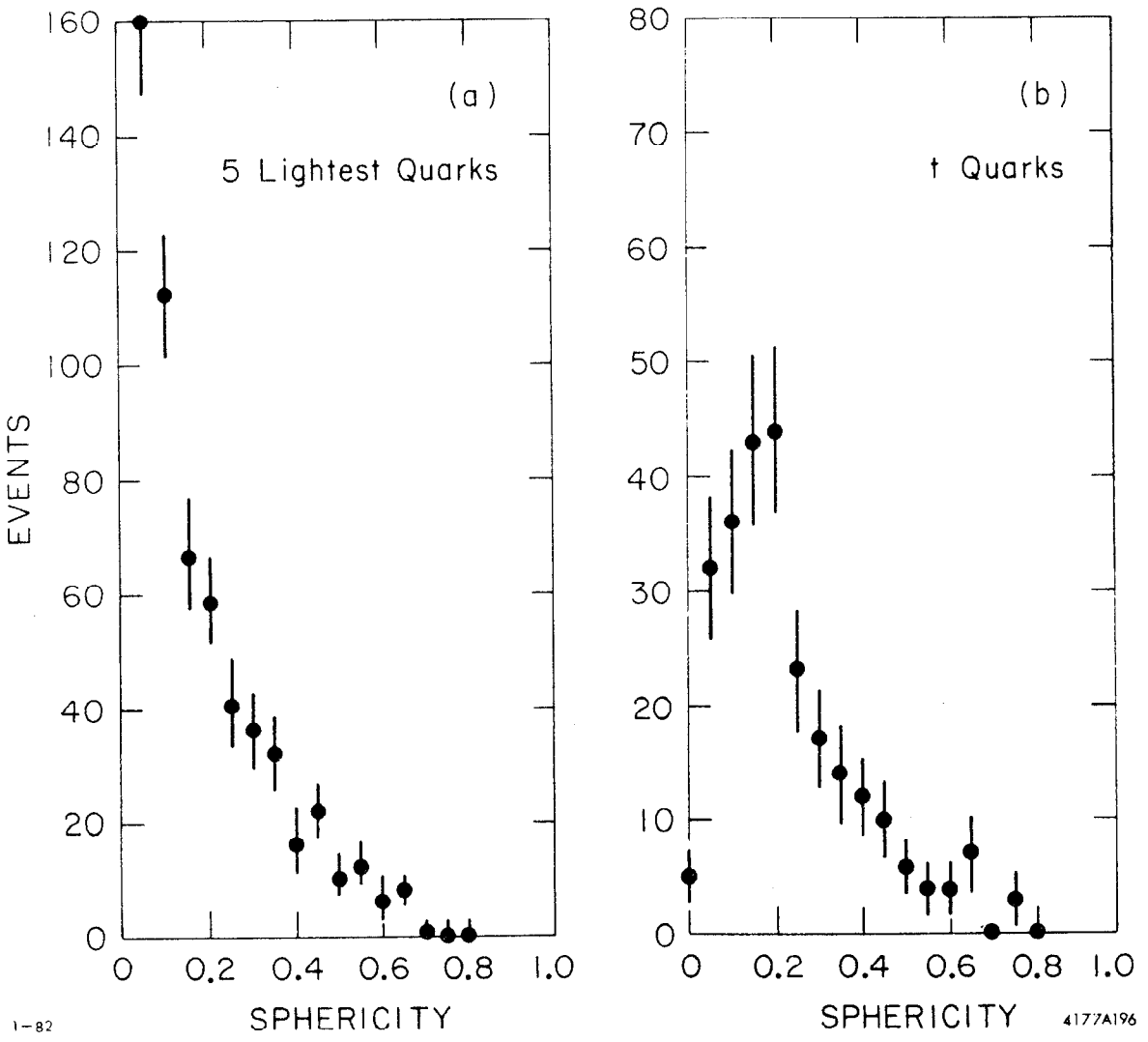

Fig. 20. Sphericity distributions in (a) u, d, c, s, and b quark events; and (b) t quark events. The analysis assumes a detector as specified in the text. The bin width is 0.05. For graph (a), the first bin (not shown) contains 1,136 events.

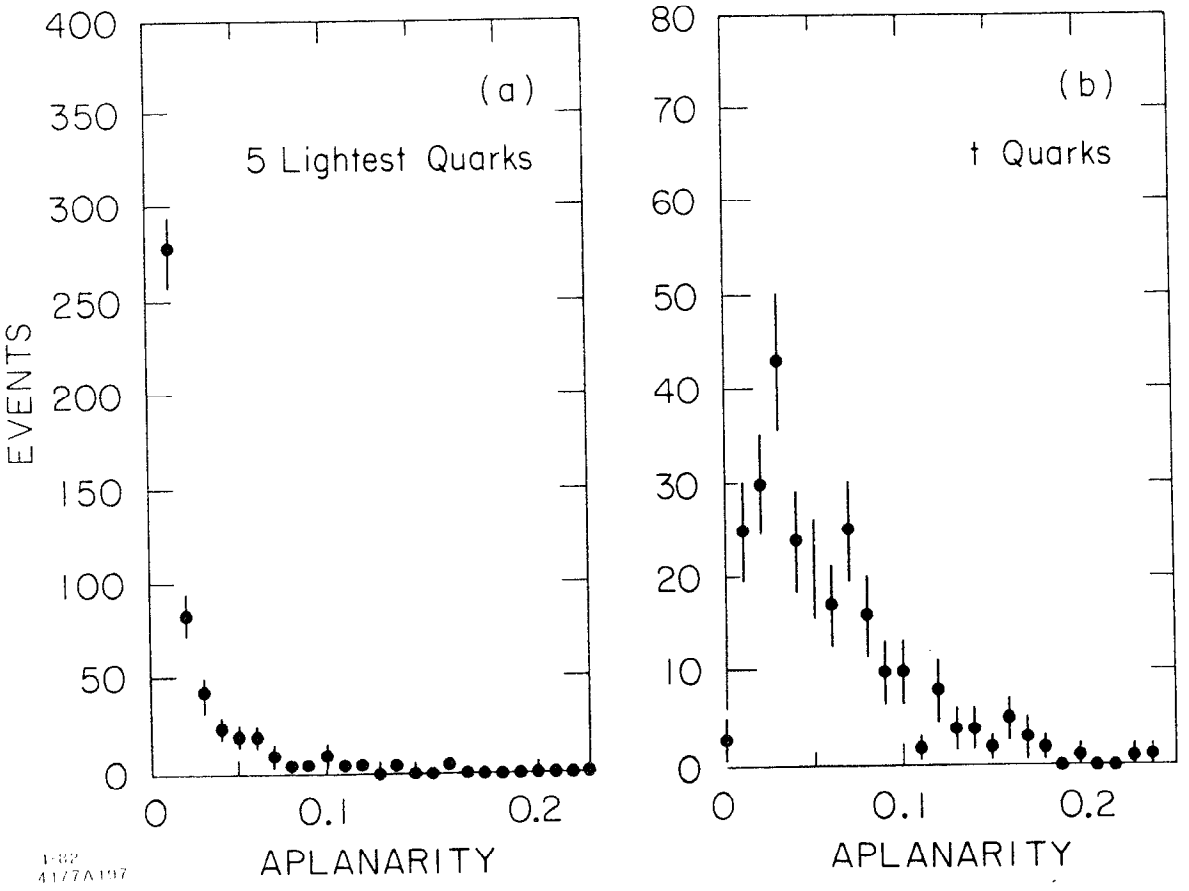

Fig. 21. Aplanarity distributions in (a) u, d, c, s, and b quark events; and (b) t quark events. The analysis assumes a detector as specified in the text. The bin width is 0.01. For graph (a), the first bin (not shown) contains 1,256 events.

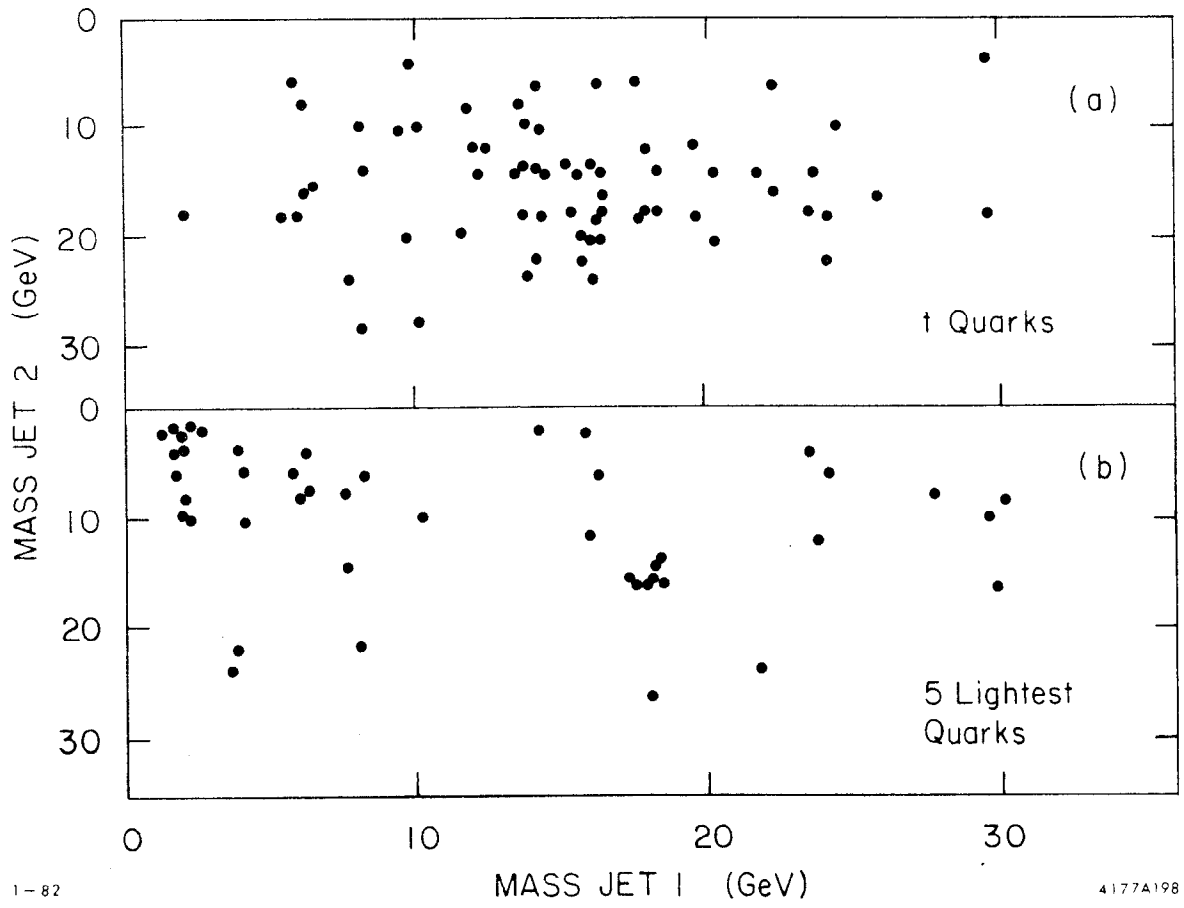

Fig. 22. Scatter plot of the reconstructed invariant masses of jets in two-cluster events with aplanarity greater than 0.04 in (a) t quark events; and (b) u, d, c, s, and b quark events. The detector assumptions are as in the two previous figures.

appears in Fig. 23. Muons arising from t quarks appear clearly separated from the rest. With the information contained in Fig. 24 it is possible to establish cuts and estimate yields of candidate $t\bar{t}$ events: Fig. 24a shows the ratio of the number of muons from t quark jets to all muons, as a function of the $p_\perp$ defined above; Fig. 24b shows the average number of muons, in a $t\bar{t}$ event, to be found above any given value of $p_\perp$ (the curve normalizes at 2.5 muons/$t\bar{t}$ event at $p_\perp \geq 0$). Thus, the selection of muons with $p_\perp \geq 2$ GeV/c results in a sample having 4 $t\bar{t}$ events out of every 5 events; in addition, about a quarter of all $t\bar{t}$ events are thus selected. Given a luminosity $\mathscr{L} = 3 \times 10^{30}$ cm^{-2}s^{-1}, this procedure should yield about 400 $t\bar{t}$ per day in an ideal detector. In this analysis the semileptonic branching ratios not known experimentally have been set to 10%.

The muons providing the t quark tag must be distinguished from the numerous hadrons of the jet. A study of hadron punch-through[25] across an iron absorber, in the framework of $Z^o \rightarrow$ jets, has given the following results: the ratio of muons to pions, for momenta above 1 GeV/c, is about 2-3%; that of muons to kaons is 8-9% in the same momentum range. Based on earlier results[26] on hadron punch-through and muon multiple scattering, it has been determined that a muon identifier consisting of 1 m of iron, preceeded by a tracking chambers measuring the momentum and impact point of the particle studied, and followed by a chamber with spatial resolution of $\Delta x \times \Delta y = 5 \times 5$ mm^2, should identify 96% of muons above the cut-off momentum (1.2 GeV/c) with an improvement of the signal-to-background ratio of about 100. Clearly, if large $p_\perp$ muons are used, the original signal-to-background level would improve greatly. Similarly, the background level could be reduced by the identification ofhadrons prior to the muon filter.

4. The Top Quark Mass

The center-of-mass energy at which the lowest lying $t\bar{t}$ resonance eventually appears will provide the most accurate estimate of the top quark mass. Since it is possible that the postulated sixth quark states will have not been discovered before the SLC operation, the question arises as to how accurate an estimate of the t quark mass is given by the

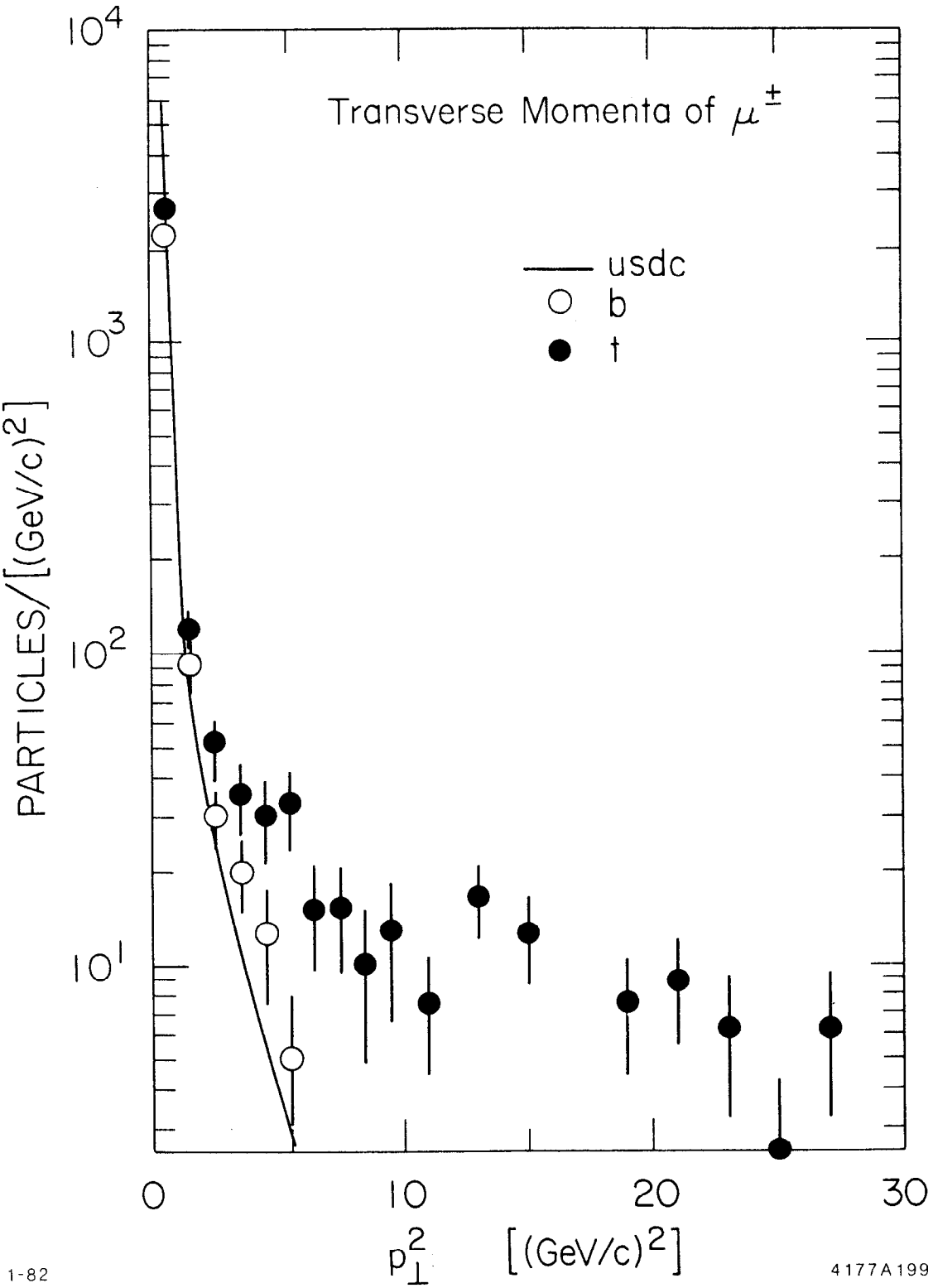

Fig. 23. The distribution of transverse momentum, squared, with respect to the quark direction, for all muons in the event. Contributions from different flavors are indicated in the figure.

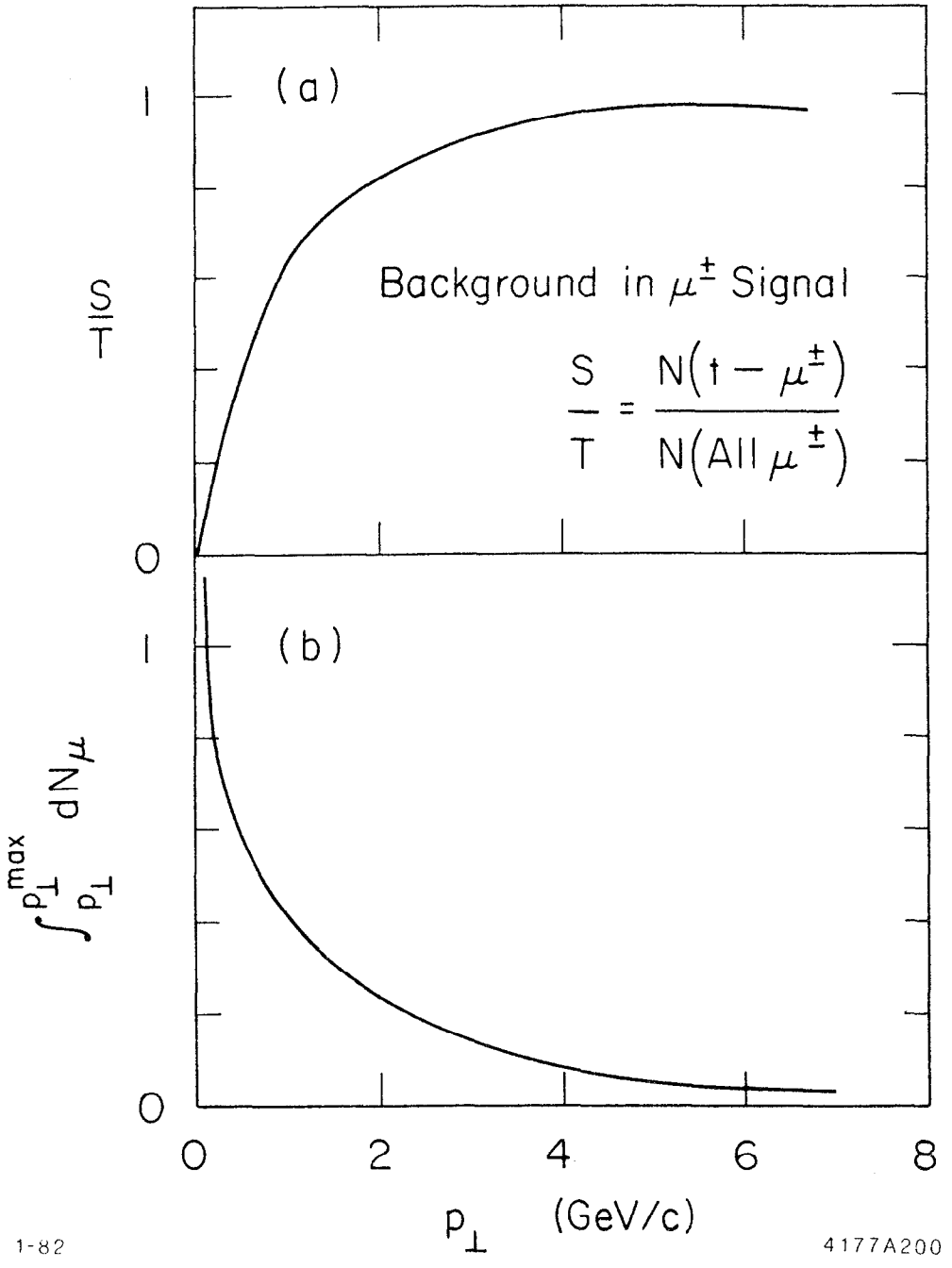

Fig. 24. (a) The ratio of the number of muons from t quark events to all muons, as a function of the muon transverse momentum with respect to the quark direction. (b) The average number of muons, in a $t\bar{t}$ event, to be found above any given value of $p_\perp$. The curve is normalized at 2.5 muon/$t\bar{t}$ event at $p_\perp \geq 0$.

t-jet invariant mass. The jet mass distributions for t quark events, selected by cluster analysis and aplanarity cuts as described earlier, appears in Fig. 25a for M_t = 19 GeV. The mean jet mass is about 16 GeV with a half-width of about 6 GeV. For a mass M_t = 30 GeV, Fig. 25b, the mean jet mass increases to only 19 GeV. Thus, the measured jet invariant mass is not linear in M_t; the nonlinearity becomes most marked for $M_t \geq 20$ GeV. The reason for this behavior is that as M_t increases the events become more spherical and the assignment of the numerous soft particles to the jets becomes somewhat arbitrary: the jets are not distinct clusterings of particles. The determination of M_t from jet masses appears too dependent on Monte Carlo simulations to be of much use.

A more promising method[27] does not depend at all on the Monte Carlo simulation of the fragmentation process, but on the rate of hadron production at the Z^o. It is based on the fact that in the standard electroweak theory the partial width for $Z^o \to t\bar{t}$ is given by

$$\Gamma_t(\beta) = 3(M_{Zo}/24\pi)\left[g_V^2\,\beta(3-\beta^2) + 2g_A^2\,\beta^3\right] \quad . \tag{1}$$

where β is the t velocity in units of the speed of light, and g_A and g_V are the t quark weak axial-vector and vector couplings, function of $\sin^2\theta_w$ only. For $\sin^2\theta_w = 0.22$, $g_A^2 >> g_V^2$ and the threshold factor for $Z^o \to t\bar{t}$ is predominantly cubic in β. Hence the rate for $Z^o \to t\bar{t}$ is strongly modulated by the threshold factor, and the overall rate for $Z^o \to$ hadrons is correspondingly reduced by the t mass effects provided $M_t < M_{Zo}/2$. Figure 26 shows the ratio

$$\rho = \Gamma_t(\beta)/\Gamma_u \tag{2}$$

as a function of the t quark mass. Here Γ_u is the partial width for $Z^o \to u\bar{u}$ (i.e., $Z^o \to$ massless Q = 2/3e quarks). With the present lower bound on M_t of 18.5 GeV, there would be 22% less hadrons from massive $t\bar{t}$ production than from massless t quarks. Since 14% of $Z^o \to$ hadrons is in the $u\bar{u}$ channel, an overall reduction of 3% of the hadronic rate is expected for M_t = 19 GeV as compared to M_t = 0.

Within the standard model ρ can be expressed in terms of the ratio r of the number of hadronic events (N_h) to the number of muon pair events ($N_{\mu\mu}$) produced at the Z^o:

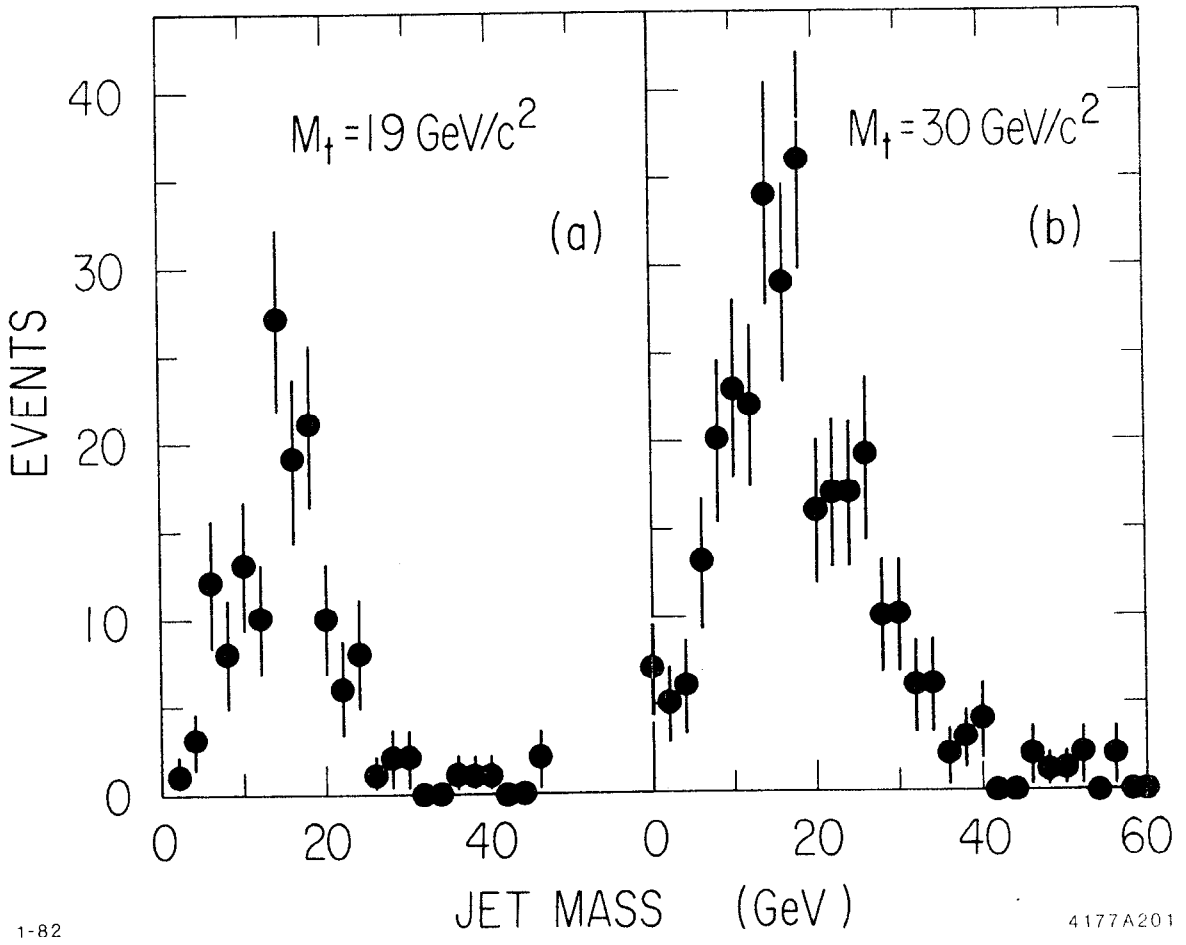

Fig. 25. The reconstructed jet masses for two-cluster events with aplanarity ≥0.04 for (a) top quark mass M_t = 19 GeV/c^2; and (b) M_t = 30 GeV/c^2.

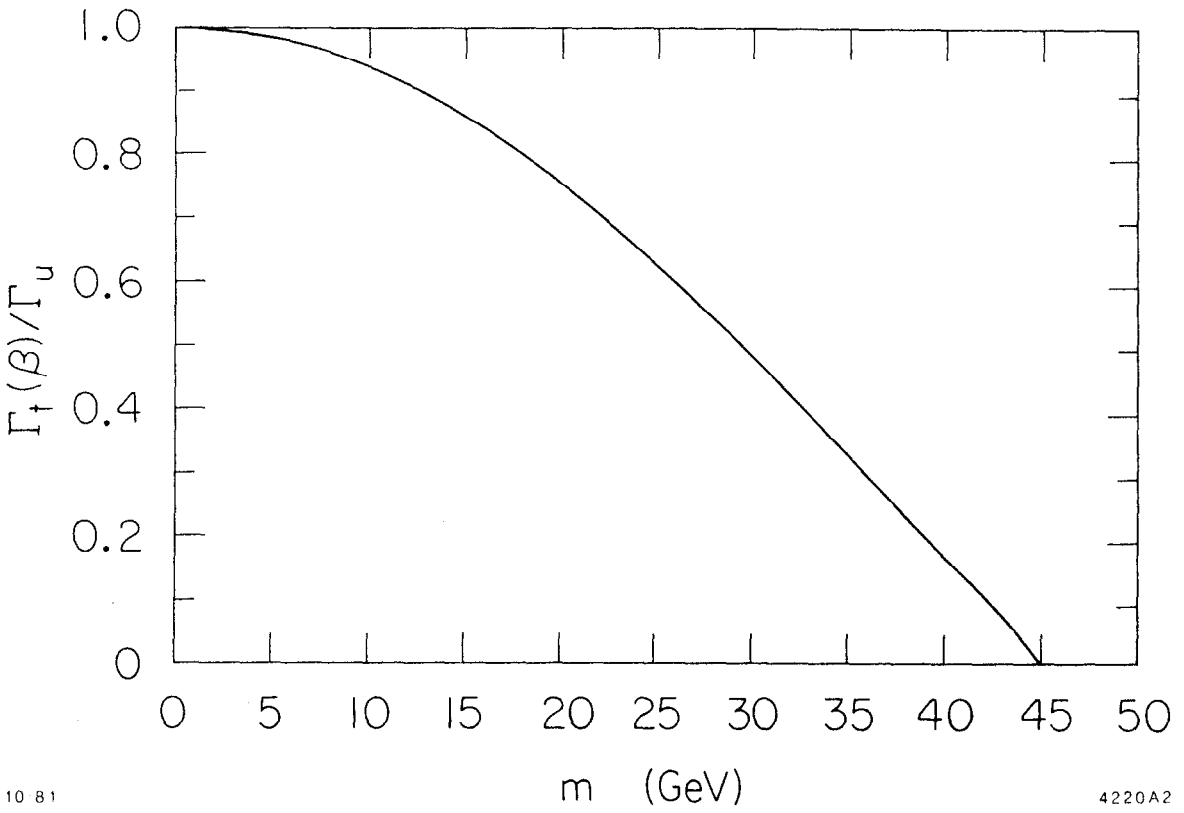

Fig. 26. The suppression factor of $t\bar{t}$ decays of the Z^o as a function of the top quark mass for $\sin^2\theta_w = 0.22$, $M_{Z^o} = 90$ GeV.

$$\rho = 1 + r \frac{\Gamma_{\mu\mu}}{\Gamma_u} - \frac{\Gamma_h}{\Gamma_u} \quad , \tag{3}$$

where Γ_h is the hadronic width calculated for three quark generations of massless, colored weak isospin doublets, $\Gamma_{\mu\mu}$ is the calculated $\mu^+\mu^-$ partial width and Γ_u is the calculated partial width into u quarks. Hence, in principle, the experiment is simple: it consists of counting the number of hadronic and muon pair events. There is no need to measure the luminosity, and the error of the t mass estimate depends on the ability of counting hadron events and muon pairs with small systematic errors. If one assumes 10^6 Z^o's, $N_{\mu^+\mu^-} = 31{,}000$, $N_h = 730{,}000$ and $\sin^2\theta_w = 0.001$,[28] the t quark mass resolution, in the absence of any systematic error, is given in Fig. 27. The resolution is adequate and independent of t quark mass. Inevitably, there will be some systematic effects; the resolution degrades by ~1 GeV per 1% systematic error in r. It should be pointed out that to apply this method one needs independent evidence that (a) the $t\bar{t}$ events are being produced at the Z^o; and (b) that there are no processes contributing to N_h beyond those of the five known quarks. Nonetheless, this method looks very promising for estimating the t quark mass.

5. Summary

In summary, general methods for tagging events involving the quarks u, d, s, c, and b have not been found. More work is required, however, on the use of vertex devices. Quark tagging is not an overwhelming motivation for good K/π separation, as individual events cannot be assigned on the basis of identified kaons of known momentum. There are several ways to tag $t\bar{t}$ events. Typical signal-to-noise ratios for these tags are 4:1, with event rates of about 400 per day each for high $p_\perp$ leptons and for high aplanarity events.

E. $Z^o \rightarrow$ Hadrons: Jets

A simple measure of a detector's aptitude to study multijet events is its ability to measure the direction and energy of the jets. These topics are discussed below.

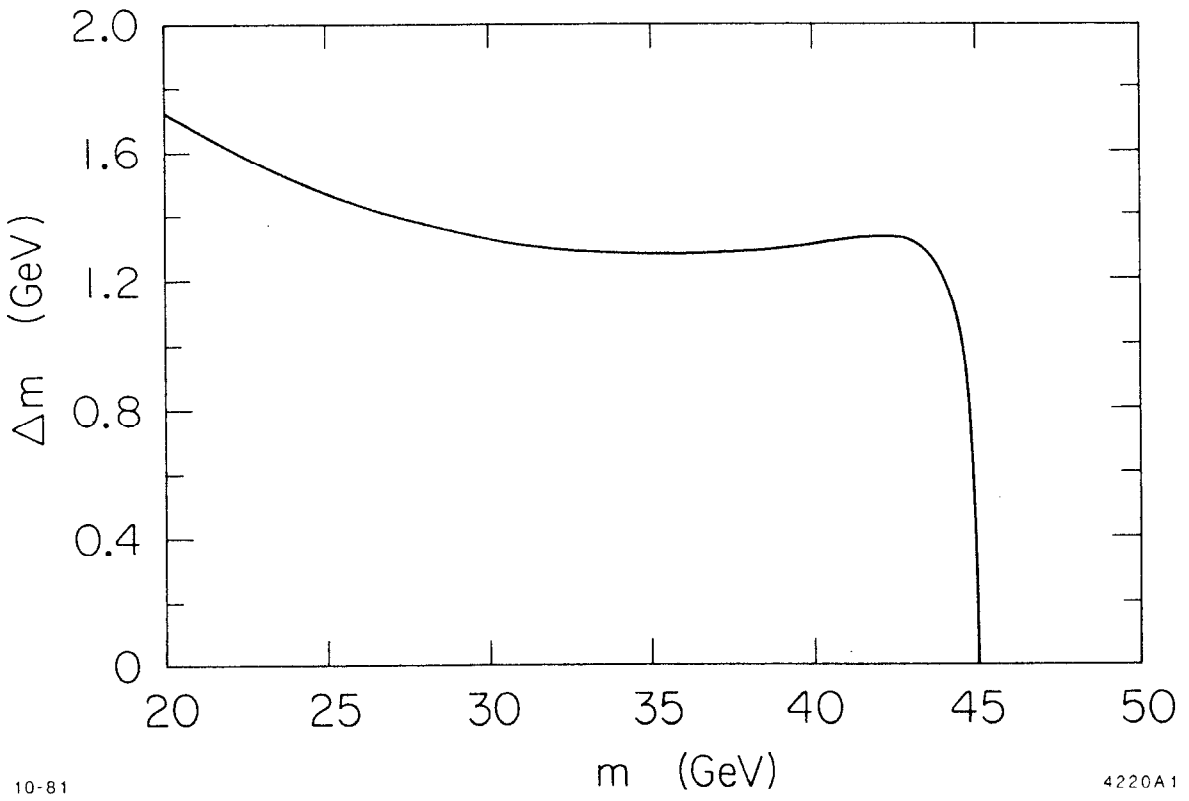

Fig. 27. The error in the determination of the top quark mass as a function of the top quark mass for a sample of 10^6 Z^o events. No systematic errors are included in this plot.

It has been shown[12] that a cylindrical drift chamber adequate for the two-jet topology has modest effectiveness in reconstructing three jet events, as shown in Table II. Consider now other systems.[7,29] The resolution of the measurement of the jet axis direction in two-jet events appears in Fig. 28a for a detector composed of calorimeters only. The inner radius of the calorimeter is 1.5 m. The curves show the distribution of the angle $\Delta\theta$ between the sphericity axis and the original quark direction for different calorimeters. An ideal detector yields the curve IRES = 0, which indicates that the error associated with the sphericity analysis algorithm is about 10 mr (the dip at $\Delta\theta = 0$ is a solid angle effect common to all curves). A calorimeter subtending $\Delta\Omega = 0.98 \times 4\pi$ sr with hadron and electromagnetic resolutions of $\Delta E/E = 35\%/\sqrt{E}$ and $10\%/\sqrt{E}$, respectively, and angular resolution of $\Delta\alpha = 10$ mr corresponds to the curve IRES = 1 and $\langle\Delta\theta\rangle \simeq 18$ mr. A lesser system ($\Delta\Omega = 0.96 \times 4\pi$ sr, $\Delta E/E = 70\%/\sqrt{E}$ (hadrons), $\Delta E/E = 20\%/\sqrt{E}$, (e's, γ's), $\Delta\alpha = 20$ mr) yields $\langle\Delta\theta\rangle \simeq 23$ mr (IRES = 2). The electromagnetic calorimeter defined by IRES = 1, used alone, achieves $\langle\Delta\theta\rangle \simeq 35$ mr. An alternative system assumes a drift chamber in the inner volume, with $\Delta\Omega = 0.96 \times 4\pi$ sr, a 5 kG solenoidal field, and electromagnetic calorimetry only. The results appear in Fig. 28b. For these model detectors of superior performance the hadron calorimeter version and the drift chamber version produce comparable results.

The three-jet topology at the SLC will be studied as a tag for $q\bar{q}g$ events. At the high SLC center-of-mass energy the three jet topology should be more easily distinguished than at the present PEP/PETRA energies, possibly allowing conclusive studies of the gluon fragmentation. While only three-jet events are discussed below, it should be pointed out that the expected sizable sample of four-jet events is of great interest as well.

A cluster alogorithm has been used to study the three-jet topology. This algorithm[23] is a method of partitioning an event into clusters, a cluster being defined by a group of particles which are correlated in direction. The particles which span the cluster define, via the vector (scalar) sum of their momenta, a cluster axis (energy). One now makes the association of clusters with jets. Application of the cluster

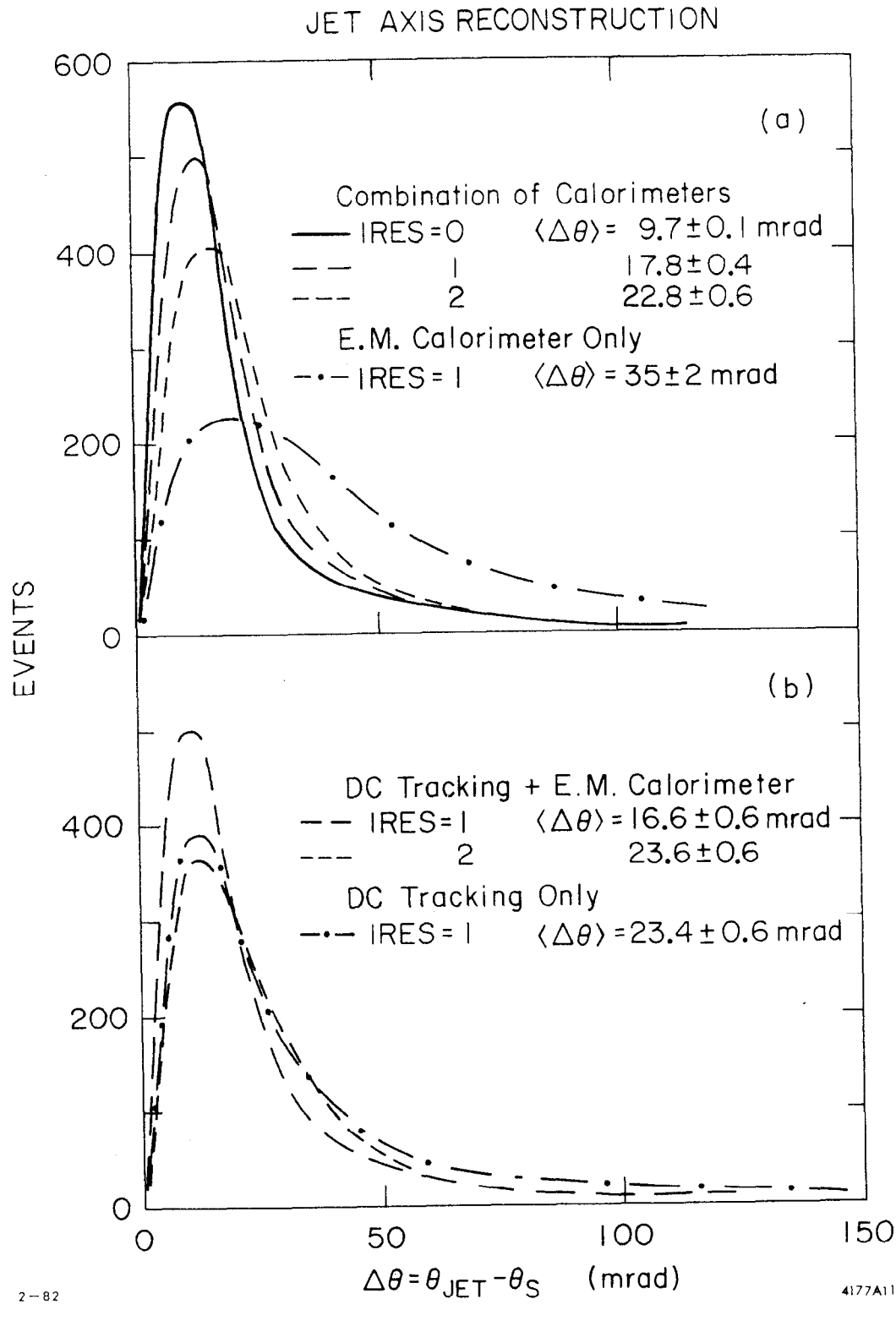

Fig. 28. Distribution of the angle between the sphericity axis and the original quark direction for various detector combinations as explained in the text.

algorithm to the $Z^o \rightarrow$ hadrons events results in the assignment of about 72% of the events to two clusters, 25% to three clusters, and the rest to four clusters.

For this study only the three-cluster events have been chosen. A word of caution is due about the t quark events. Since these events are quite spherical, their jets having large spreads, the notion of jets is ill-defined. Application of the cluster algorithm (or similar analyses) will unwittingly accept a very large fraction of $Z^o \rightarrow t\bar{t}$ events (as opposed to the desired $Z^o \rightarrow t\bar{t}g$ events) as three-jet candidates. Hence an aplanarity cut (<0.03) has been made to remove the $t\bar{t}$ events from the three-cluster class. This cut loses few (~12%) three-cluster events arising from the lighter quarks and only a very small number (4%) of $t\bar{t} + t\bar{t}g$ events enter the three-cluster class.

The efficiency for assigning the produced three-jet events to the three-cluster class limits the sample of identified $q\bar{q}g$ events. This efficiency has been studied[29] as a function of solid angle, resolutions, and calorimeter configuration. The most drastic reduction in the three-jet yield is due to the reduction of solid angle, as shown in Table VII.

Table VII

The fraction of events assigned to three clusters relative to the number of produced three-jet events, and the fraction of detected energy, are tabulated as a function of the solid angle covered by an otherwise perfect central detector.

Solid Angle Covered	Three-Jet Efficiency	Fraction of Energy Seen
$\lvert\cos\theta\rvert < 0.7$	0.36	0.57
$\lvert\cos\theta\rvert < 0.8$	0.46	0.67
$\lvert\cos\theta\rvert < 0.9$	0.63	0.77
All $\cos\theta$	0.78	0.90

For orientation, an efficiency of 60% for the three-jet events corresponds to an overall efficiency, relative to all hadron events, of ≃20% with a rate of several thousand $q\bar{q}g$ events per day. A discussion of angular and

energy resolution follows. The Monte Carlo parton directions have been compared with the calculated cluster axes to obtain the jet axis resolution. Then, from the jet measured direction and the assumption of zero-mass quarks it is possible to calculate the jet energies. Since most detectors will have better angular resolution than energy resolution, this method[23] yields better jet energy resolution than other approaches. Table VIII summarizes the jet energy and angular resolution obtained with the three cluster events. Three detector parameterizations, as indicated in the table caption, are compared to an ideal detector. One sees that for a detector similar to those which exist today (model 2) it is possible to achieve good three-jet efficiency, angular and energy resolution. The spatial distributions of the three clusters show that they are well separated in the detector. This, in addition to the good energy and direction resolution, should permit careful studies of both the quark-gluon matrix element and the fragmentation processes.

Table VIII

The table summarizes the results of a study of jet axis direction resolution ($\delta\theta_j$) and jet energy resolution (δE_j) for three-cluster events. Also shown is the fraction of energy detected (E_{seen}) and the fraction of produced three-jet events which are reconstructed as three clusters (ϵ_{3jet}). The index j is 1 for the fastest jet, 2 for the intermediate jet and 3 for the slowest jet.

Model 1: Charged tracking over 95%; $\Delta p/p^2 = 0.25\%\ GeV^{-1}$. Photon tagging over 98%, $\Delta E/E = 10\%/\sqrt{E}$, 2 cm (5 cm) strips (towers). Barrel detector is 4 m long at R = 1.5 m, rest endcaps.

Model 2: Charged tracking over 86%; $\Delta p/p^2 = 0.5\%\ GeV^{-1}$. Photon tagging over 98%; $\Delta E/E = 15\%/\sqrt{E}$, 5 cm (15 cm) strips (towers). Barrel detector is 3 m long, at R = 1.5 m, rest endcaps.

Model 3: Same as model 2 except no endcap photon detection.

		$\delta\theta_1$ degrees	$\delta\theta_2$ degrees	$\delta\theta_3$ degrees	δE_1 percent	δE_2 percent	δE_3 percent	E_{seen} percent	ϵ_{3jet} percent
Perfect Detector		1.2	1.6	3.4	1.6	4.7	12.0	90	78
Model 1	Strips	1.8	2.3	4.8	2.4	7.2	15.0	76	65
	Towers	2.0	2.5	4.8	2.5	7.2	15.0		
Model 2	Strips	1.9	2.4	4.2	2.8	7.2	17.3	72	63
	Towers	2.4	2.9	4.9	2.9	7.2	18.0		
Model 3	Strips	2.0	2.5	5.2	5.6	7.1	18.6	63	45
	Towers	2.5	3.0	5.6	5.6	7.0	18.7		

III. $Z^o \to$ CHARGED LEPTON PAIRS

A. General Considerations

We begin our discussion with some general remarks about cross sections and asymmetries. Formulas for cross sections and polarization effects in e^+e^- annihilation into $f\bar{f}$ pairs through an arbitrary number of neutral gauge bosons have been given in Ref. 30. If we limit ourselves to only two neutral gauge bosons, namely the photon and one Z^o, and unpolarized beams, the appropriate formulas in the limit $m_f/M << 1$ ($M = Z^o$ mass) are given by

$$\frac{d\sigma}{d\Omega} = \frac{\alpha^2}{4s}\left\{(1+\cos^2\theta)\left[q_f^2 + \left(v_e^2+a_e^2\right)\left(v_f^2+a_f^2\right)|\chi|^2 - 2\,q_f v_e v_f \mathrm{Re}\chi\right]\right.$$
$$\left. + \cos\theta\left[8\,v_e v_f a_e a_f|\chi|^2 - 4\,q_f a_e a_f \mathrm{Re}\chi\right]\right\} \qquad (4)$$

q_f is the charge of the outgoing fermion, v_e, v_f, a_e, a_f are the initial and final vector and axial vector couplings to the Z^o and the quantity χ is given by

$$\chi = \frac{s}{\left(s - M_{Z^o}^2\right) + i\Gamma M_{Z^o}} \qquad (5)$$

The forward-backward asymmetry follows from Eq. (4)

$$A_{ch} = \frac{3}{2}\,\frac{2\,v_e v_f a_e a_f|\chi|^2 - q_f a_e a_f \mathrm{Re}\chi}{q_f^2 + \left(v_e^2+a_e^2\right)\left(v_f^2+a_f^2\right)|\chi|^2 - 2\,q_f v_e v_f \mathrm{Re}\chi} \qquad (6)$$

We apply these formulas to the case of outgoing leptons (except electrons) for which $q_f = -1$, and assume lepton universality, hence $a_e = a_f \equiv a$, $v_e = v_f \equiv v$ leading to

$$\frac{d\sigma}{d} = \frac{\alpha^2}{4s}\left\{(1+\cos^2\theta)\left[1 + (a^2+v^2)^2|\chi|^2 + 2\,v^2\mathrm{Re}\chi\right]\right.$$
$$\left. + \cos\theta\left[8\,v^2a^2|\chi|^2 + 4\,a^2\mathrm{Re}\chi\right]\right\} \qquad (7)$$

$$A_{ch} = \frac{3}{2} \frac{2a^2v^2|\chi|^2 + a^2 Re\chi}{1 + (a^2 + v^2)^2|\chi|^2 + 2\, v^2 Re\chi} \tag{8}$$

We also give the outgoing lepton helicity, again for unpolarized beams, just at the Z^o energy

$$P = -\left[\frac{2av}{a^2 + v^2}\right] \frac{1 + \frac{2\cos\theta}{1 + \cos^2\theta}}{1 + \left[\frac{2av}{a^2 + v^2}\right] \cdot \frac{2\cos\theta}{1 + \cos^2\theta}} \tag{9}$$

If an average over θ is taken,

$$P = -\frac{2av}{a^2 + v^2} \tag{10}$$

The coupling constants a, v for the standard model are given by

$$a = -\frac{1}{2 \sin 2\theta_w} \qquad v = \frac{-1 + 4 \sin^2\theta_w}{2 \sin 2\theta_w} \tag{11}$$

We have neglected radiative corrections which, for $s > M^2$, substantially affect the cross section and asymmetry.[31] It is clear from Eq. (8) that measurements of the asymmetry as a function of energy provide determinations of the constants a^2, v^2. The outgoing helicity also tests the relative sign of a and v. The expected asymmetry as a function of energy[31] is shown in Fig. 29 with radiative effects for various energy resolutions shown on the figure.

B. Experimental Considerations in $Z^o \to \mu^+\mu^-$

The identification of the $\mu^+\mu^-$ final state as a pair of collinear muons seems straightforward. A tracking system which provides adequate momentum resolution to determine the signs of the muons with high reliability is required. A reasonable criterion is to require that each sagitta be $>2\sigma$ from zero, from which it follows that $\Delta p/p^2 = 1\%\ GeV^{-1}$, and that the assignment of signs to the muons is established to about the 3σ level.

The solid angle requirements to provide useful statistics have also been studied.[32] Expected asymmetries, as functions of cut-off angle are shown in Fig. 30 (with no radiative corrections). Fractional asymmetry

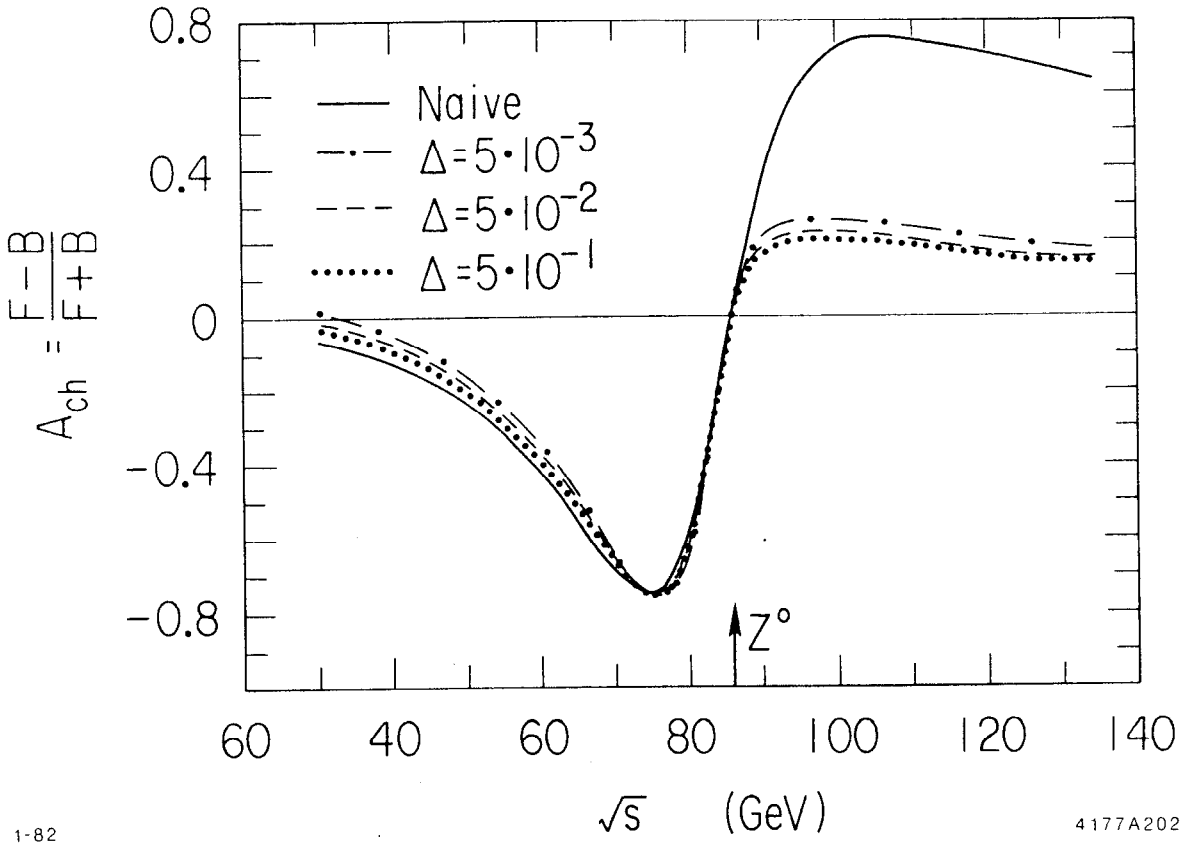

Fig. 29. Integrated forward-backward asymmetry for $Z^o \to \mu^+\mu^-$, including radiative corrections, as a function of total energy for various energy resolutions (dotted lines), and without radiative corrections (full line).

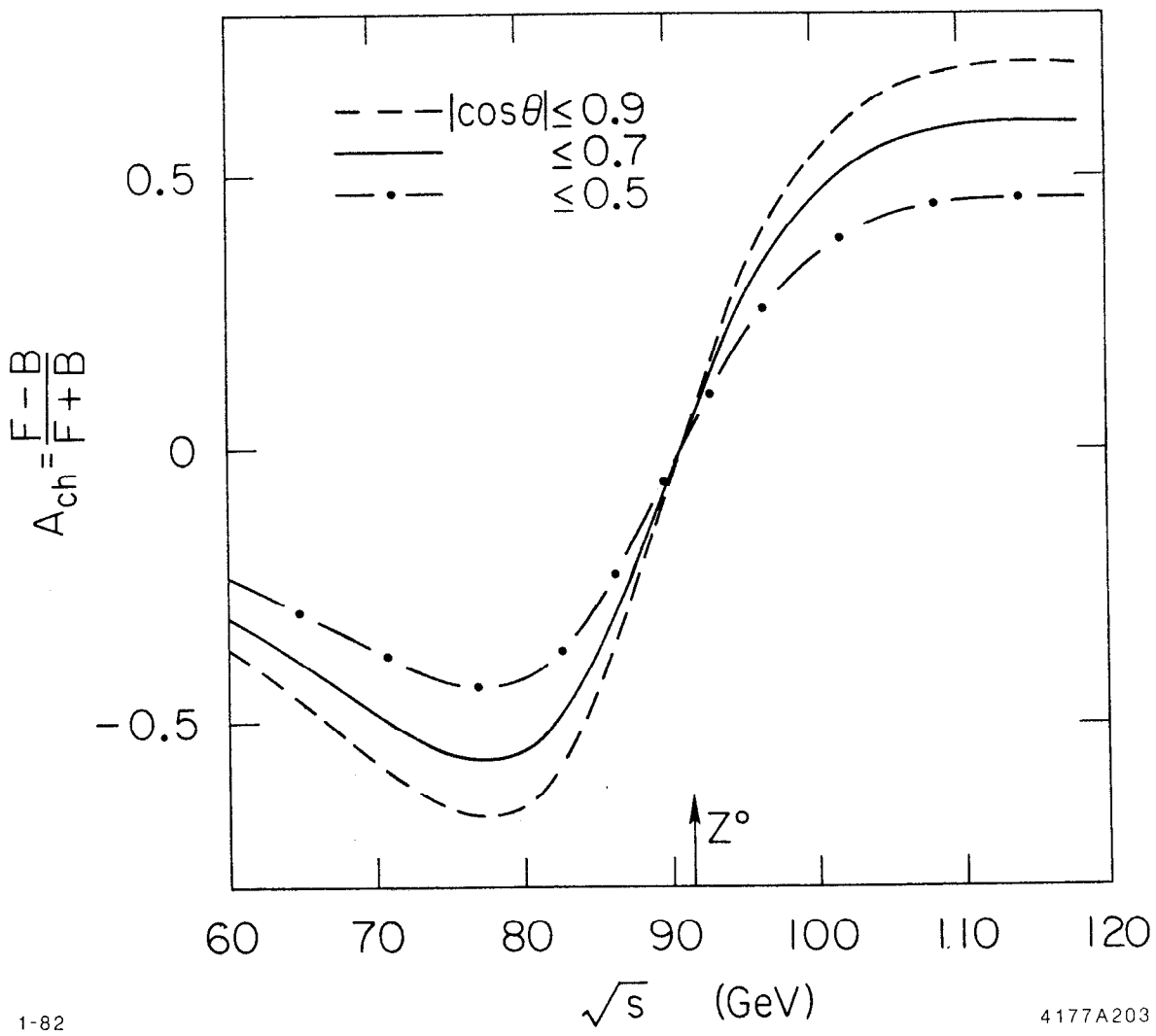

Fig. 30. Integrated forward-backward asymmetry without radiative corrections for detectors with various polar angle cut-offs.

errors based on full running efficiency one-month runs at $\mathscr{L} = 10^{30}$ cm^{-2} sec^{-1} are shown in Fig. 31. It is rather clear that a cut-off $|\cos\theta|$ close to 0.9 is very desirable.

If one considers a drift chamber of outer radius 1.5 m and length 3 m and demands that a precision $\Delta p/p^2 = 1\%$ GeV^{-1} be available down to $|\cos\theta| = 0.9$, the precision for tracks traversing the full chamber has to be $\Delta p/p^2 = 0.3\%$ GeV^{-1}. This figure increases to 0.7% GeV^{-1} for a chamber of length 4 m.

C. Measurement of the Lepton Polarization

1. Introduction

The unequal left- and right-handed couplings g_L, g_R of the Z^o to all elementary fields results in characteristic polarizations of the intermediate boson itself and of the states into which it decays. Both the standard[5] and extended[33] (multi-Z^o) models of the weak and electromagnetic interactions predict the partial polarization of pair-produced leptons. In the standard model, disregarding the electromagnetic interaction, the polarization of τ's is given at the Z^o pole by

$$P_\tau(\theta) = \frac{P(\tau) + P(Z^o)\,\dfrac{2\cos\theta}{1+\cos^2\theta}}{1 + P(\tau)\,P(Z^o)\,\dfrac{2\cos\theta}{1+\cos^2\theta}} \qquad (12)$$

where $P(\tau) = -2\,v_\tau a_\tau/(v_\tau^2 + a_\tau^2)$ is the intrinsic τ polarization, and $P(Z^o) = -2\,v_e a_e/(v_e^2 + a_e^2)$ is the intrinsic Z^o polarization. Here v_j, a_j are the vector and axial-vector couplings of particle j. If universality holds, all charged leptons have the same couplings, Eq. (11) above. For $\sin^2\theta_w = 0.23$, the coupling is predominantly axial-vector, with $a/v \cong 12$.

By integration of the numerator and denominator of Eq. (12) over an angular interval symmetric around 90^o, the dependence on the polarization state of the intermediate boson drops and $\langle P_\tau(\theta)\rangle = P(\tau) \approx -0.16$. Therein lies the importance of the measurement of the final state average polarizations, as the experimental observation depends only on the couplings of particle studied. This is not the case, for instance, for the determination of the forward-backward asymmetry, A_{ch},

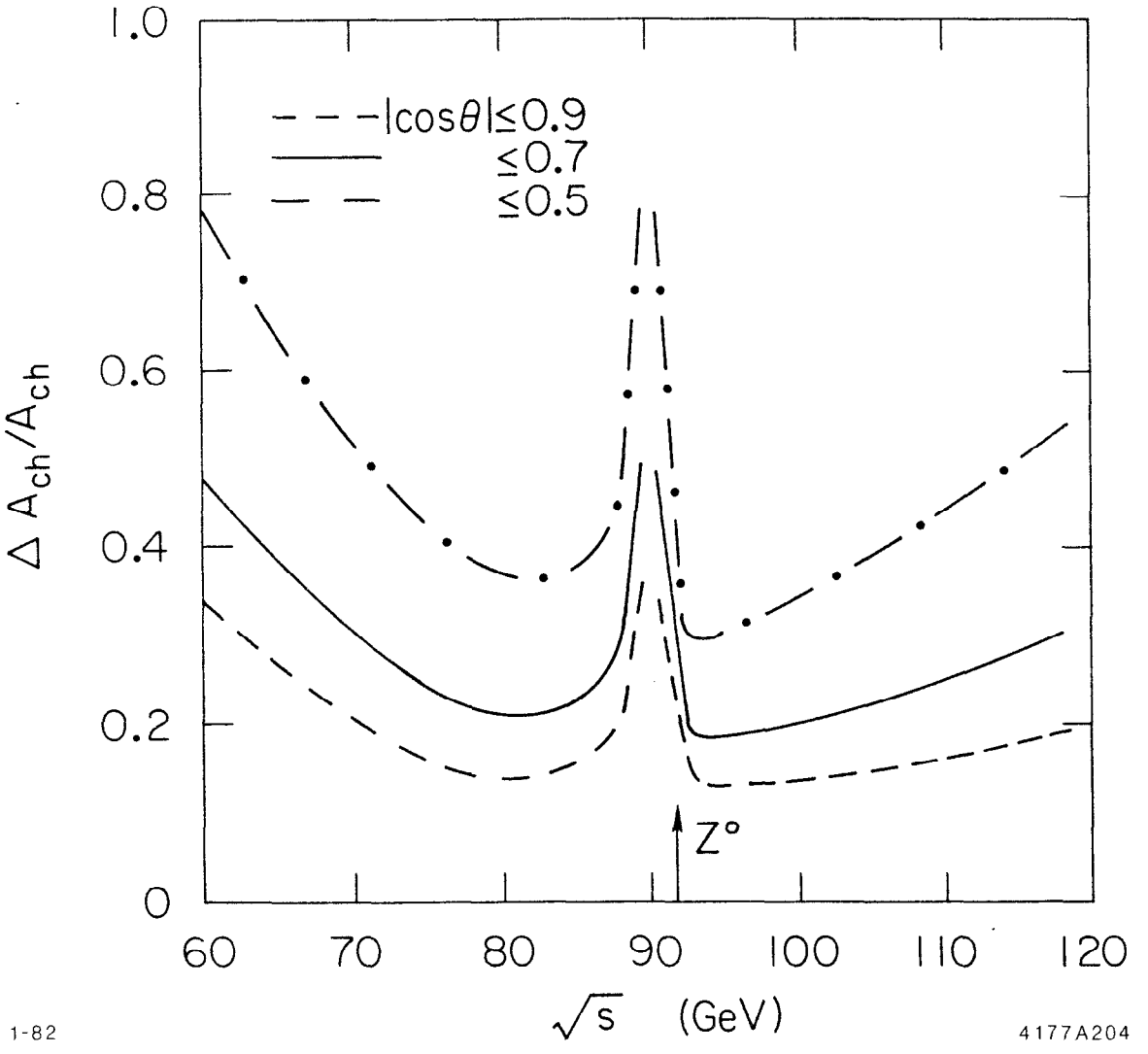

Fig. 31. Fractional error in asymmetry determination for various polar angle cut-offs. Each point corresponds to a one-month run of full efficiency with $\mathscr{L} = 10^{30}$ cm^{-2} sec^{-1}.

$$A_{ch} = \frac{3}{4} P(Z^o)\ P(\tau) \qquad (13)$$

which relies on an independent determination of $P(Z^o)$ in order to extract $P(\tau)$. Were universality to be broken, with $P(Z^o) = 0$ and $P(\tau) \neq 0$, the charge asymmetry would vanish, while the final lepton polarization would still yield $P(\tau)$.

Similar arguments apply for polarized beams. Both the polarization and asymmetry are affected by the longitudinal polarization P_e of the electron beam. When $P_e \neq 0$, the above formulae apply with the substitution

$$P(Z^o) \rightarrow P = \frac{P_e + P(Z^o)}{1 + P_e\ P(Z^o)} \qquad (14)$$

P being the actual Z^o polarization. The charge asymmetry determination relies now on measurements of both P_e and $P(Z^o)$, while the average τ polarization is independent of them and, in fact, even independent of any unknown residual beam polarization in the machine.

2. Muon Polarization Measurement

The measurement of the muon polarization in the channel $e^+e^- \rightarrow Z^o \rightarrow \mu^+\mu^-$ requires that the muons be stopped and their decay asymmetry observed in a polarimeter. Muons of $E_\mu \simeq 45$ GeV stop in about 39 m for iron and could be trapped in magnetized iron toroids concentric with the beam directions, as is done in CERN's neutrino experiment[34] and the NA4 deep inelastic muon scattering experiment. For Z^o physics, this type of detector has been suggested[35] in the LEP studies. While in principle feasible, the dimensions required to trap sufficient rate makes this scheme difficult. It has also been suggested[36] that the muons be stopped in the ground surrounding the subterranean interaction region, without any focussing, and that their decay asymmetry be measured in large distilled-water-tank Cerenkov counters.[37] Quite forbidding dimensions result for Cerenkov tanks adequate to collect sufficient numbers of muons.

3. Tau Polarization Experiment

The tau's have a mean decay length[38] of about 2.5 mm at $E_{beam} = 45$ GeV. The laboratory momentum distributions of the decay products in the

channels $\tau \to e\nu\bar{\nu}$, $\tau \to \mu\nu\bar{\nu}$ [branching fraction (17.3 ± 1)% each], $\tau \to \pi\nu$ [(8 ± 3)%], and $\tau \to \rho\nu$ [(22 ± 4)%], all depend on $P(\tau)$. In terms of the ratio $x = E/E_{beam}$, where E is the decay particle energy, the laboratory distributions are[39]

$$\frac{dN}{dx} = \left(\frac{1}{3}\right)\left[5 - 9x^2 + 4x^3 + P(\tau)(1 - 9x^2 + 8x^3)\right] \qquad (15)$$

for the leptonic decay, and

$$\frac{dN}{dx} = 1 + P(\tau)(2x - 1) \qquad (16)$$

for the $\pi\nu$ mode.[40] The $\rho\nu$ distributions are given in Ref. 41. Examples of these distributions for different values of the parameter $\sin^2\theta_w$ appear in Figs. 32a and 32b. The signature of the $\tau^+\tau^-$ events of interest is just two oppositely charged particles in the detector. Although hadron events outnumber tau events by a factor $\Gamma(Z^o \to \text{hadrons})/\Gamma(Z^o \to \tau^+\tau^-) \simeq 23$ ($\sin^2\theta_w = 0.23$, $M_t = 20$ GeV) their expected average charged multiplicity is $\langle n_{ch} \rangle = 22$ and thus will not contribute two-prong events. Two-photon processes, $e^+e^- \to e^+e^-e^+e^-$, $e^+e^-\mu^+\mu^-$, and e^+e^- + hadrons, could produce the same multiplicities, but not the same visible energy, as the τ events. From Eqs. (15) and (16) the average values of x are

$$\langle x \rangle = \left(7 - P(\tau)\right)/20 \qquad (e\nu\bar{\nu},\ \mu\nu\bar{\nu}) \qquad (17)$$

and

$$\langle x \rangle = \left(3 + P(\tau)\right)/6 \qquad (\pi\nu) \qquad (18)$$

An estimate for the average invariant mass of the observed pair of particles is

$$\langle M^2 \rangle \simeq 4 \langle x_1 \rangle \langle x_2 \rangle E_b^2 \qquad (19)$$

since the decay products are collimated along the τ initial direction by the boost $\gamma_\tau \simeq 25$. This quantity is about $(36 \text{ GeV})^2$ for lepton-lepton and $(42 \text{ GeV})^2$ for π-π pairs, well beyond the observable production levels via the two photon mechanisms.[42]

The pair production of heavy leptons L $\left(e^+e^- \to Z^o \to L^+L^-\right)$ with a threshold above the present storage ring energies, could contaminate the

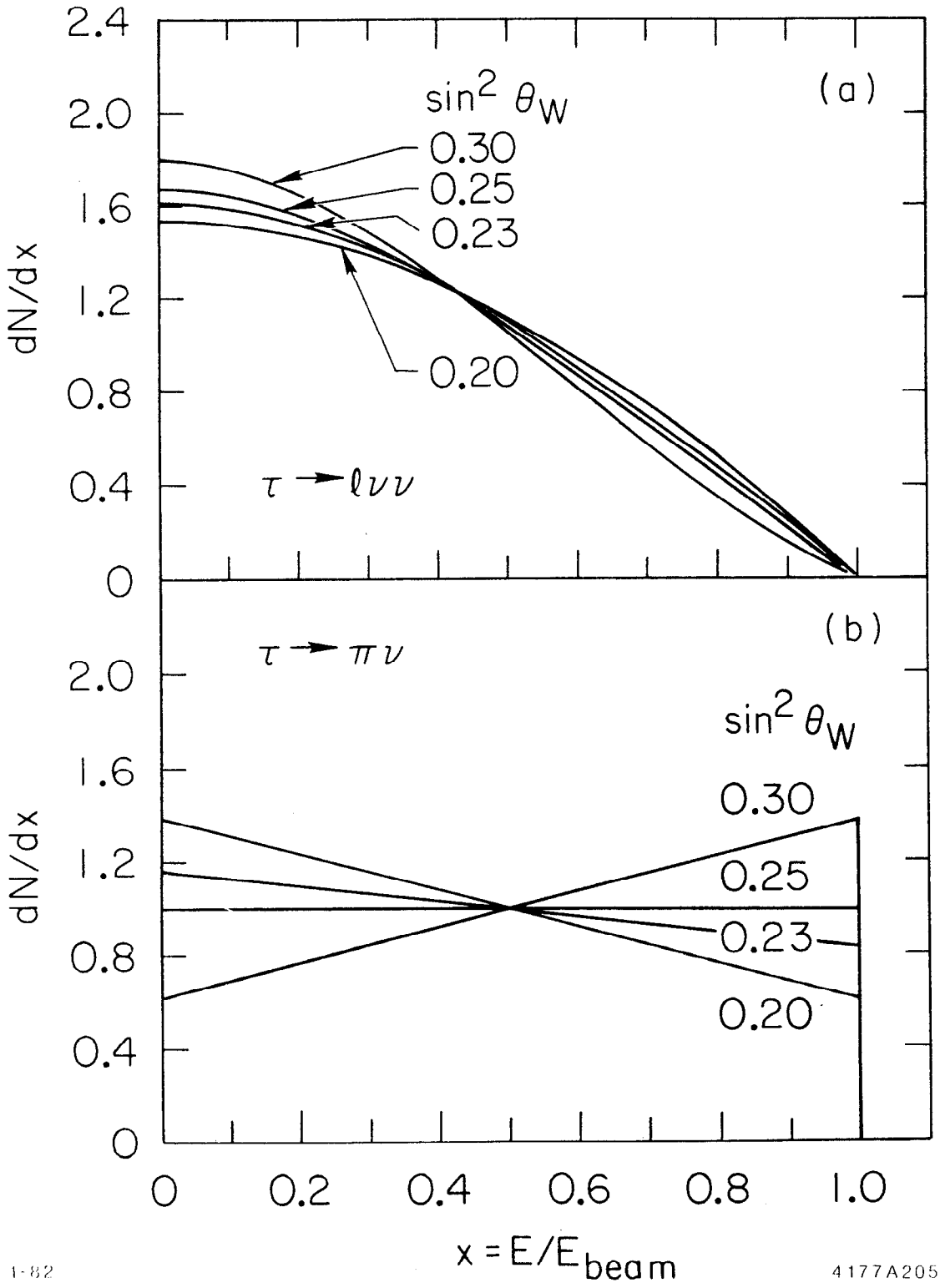

Fig. 32. Momentum spectra in the tau decay for different values of the weak parameter $\sin^2\theta_w$ for (a) charged leptons in $\tau \to \ell\nu\nu$; and (b) pions in $\tau \to \pi\nu$.

$\tau^+\tau^-$ sample. While this question needs quantitative study it is easy to estimate that the fraction of L^+L^- pairs yielding quasi-collinear decay products is small: the characteristic deviation from collinearity for decay products in opposite hemispheres is of order $\alpha_L \simeq M_L/E_b$, with M_L the heavy lepton mass, and $\alpha_\tau \simeq 30$ mr while $\alpha_L \simeq 300$ mr for $M_L = 20$ GeV.

Given that the $\tau^+\tau^-$ channel is not contaminated by other Z^o decays, the detector studies naturally focussed on separating the τ decay modes from one another, and on the precision required of the momentum and energy measurement.

A study[43] of parameters in a conventional detector deals with the question of statistics, e/π and μ/π separation, the electromagnetic calorimeter effective segmentation needed to avoid contamination by the $\tau \to \rho\nu \to \pi\gamma\gamma\nu$ mode, the chamber resolution, and the overall precision of determination of $\sin^2\theta_w$. The detector considered was of the standard cylindrical type, without end caps. It consisted of a tracking chamber with inner and outer radii $R_i = 10$ cm, $R_o = 150$ cm respectively, 3 m long, in a 5 kG solenoidal field; an electromagnetic calorimeter segmented in depth into an active converter and the bulk of the counter with four radiation lengths (X_o) and 12 X_o, respectively; the magnet coil; and a muon filter of five absorption lengths of iron ($P_\mu \geq 1.5$ GeV/c). The simulation did not include a hadron calorimeter, but assumed that the iron was instrumented to reduce the punch through to about 0.1%. These and other parameters were determined by requiring that the confusion of different τ decays, the main source of systematics measured, be below 1%, and by demanding that the measured, resolution-smeared, momentum distributions be sensitive to variations of $\sin^2\theta_w$. The chamber momentum resolution needed was found to be at least $\Delta p/p = 0.005\ p(\text{GeV})$, but no great increase of sensitivity is achieved by the use of $\Delta p/p = 0.002\ p$ since the errors become statistically limited in a sample of 30,000 $\tau^+\tau^-$. The shower counter resolution requirement is about $\sigma(E)/E = 0.02 + 0.12/\sqrt{E}$, and plays a direct role in the $P(\tau)$ determination as the electron spectrum was determined by the weighted average of p and E measurements. Of particular interest is the study of the effective lateral segmentation of the shower counter. In order to isolate the channels $\rho\nu$ and $e\nu\bar{\nu}$ at the 1% level by alternatively requiring energy and momentum match, symmetry of the shower around the

track impact point, and physical separation of the photons, an effective cell size of 40 mr × 40 mr was obtained. A separate study[44] indicates that a segmentation 10 to 40 times finer is needed for the calorimeter to isolate these channels without using the p, E match and shower-track geometrical association.

With the quoted statistics and parameters, the following errors in the determination of $\sin^2\theta_w$ resulted:

Channel	$\Delta\sin^2\theta_w$	
$e\nu\nu$	0.008	Combined: 0.006
$\mu\nu\nu$	0.010	
$\pi\nu$	0.005	
all	0.004	

Simulated measured spectra appear in Figs. 33a and 33b.

In conclusion, the measurement of τ polarization does not demand unusual performance of each detector component but because the τ decays into both leptons and hadrons the particle identification requirements are quite stringent. The segmentation of a central electromagnetic shower counter calls for 7500 to 15000 reconstruction cells with which probably the $\rho\nu$ mode could be also used to determine $\sin^2\theta_w$. The muon filter requires about 500 t of iron and 100 m^2 of sensitive area. Because all decay modes have comparable branching fractions it is not worthwhile to measure any one channel with a special detector, save perhaps the $\mu\nu\bar{\nu}$ mode. The τ polarization measurement should be then one of the physics goals of a general detector.

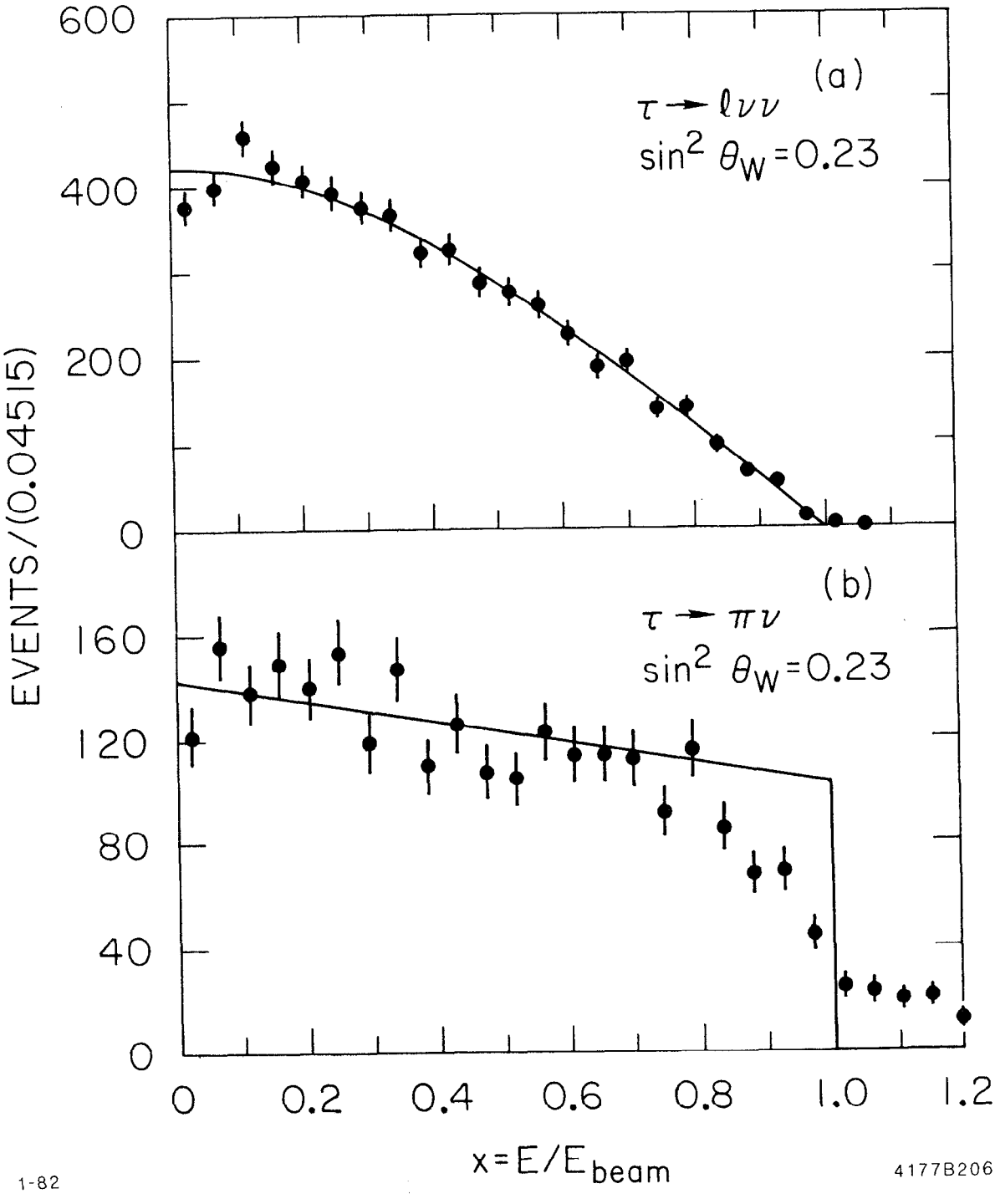

Fig. 33. The momentum spectrum of decay products in polarized tau decays distorted by the chamber and shower counter resolutions for electrons (a), and by the chamber resolution for pions (b). The simulated measurements refer to 10,000 electron and 4,800 pion events.

IV. OTHER PROCESSES

A. Neutrino Counting

One of the most important measurements to be performed at the SLC — the determination of the partial decay width of the neutral gauge boson (Z^o) into neutrinos (or other low mass weakly interacting particles) has been the subject of recent study[45,46]. This measurement would show whether there are neutrinos, beyond the three types already known (ν_e, ν_μ, ν_τ), having charged partners with masses too large to be produced by the accelerators now available. Besides having important implications in particle physics, the number of low mass neutrinos is an important parameter of models of the development of the early universe.

The total Z^o width, Γ_Z, is given in terms of the number of fundamental fermions by

$$\Gamma_Z = \frac{G_F M_Z^3}{24\sqrt{2}\pi} \left\{ 2N_\nu + \left[1 + \left(1 - 4\sin^2\theta_w\right)^2\right] N_\ell + 3\left[1 + \left(1 - \frac{8}{3}\sin^2\theta_w\right)^2\right] N_{2/3} + 3\left[1 + \left(1 - \frac{4}{3}\sin^2\theta_w\right)^2\right] N_{-1/3} \right\} \quad (20)$$

where G_F is the Fermi coupling constant; N_ν is the number of low mass neutrinos; N_ℓ is the number of charged leptons with masses less than $M_Z/2$; and $N_{2/3}$ and $N_{-1/3}$ are, respectively, the number of 2/3 and -1/3 charged quarks with masses less than $M_Z/2$. Phase space effects from finite lepton and quark masses have been ignored in this equation. Equation (20) shows that one can determine N_ν by a precision measurement of Γ_Z. With the accepted value of $\sin^2\theta_w$, Γ_Z = 2.6 GeV and varies by 0.16 GeV per additional neutrino. An unambiguous, 3-σ, determination of $\Gamma_{\nu\bar{\nu}}$ requires then a precision of better than 2% in Γ_Z and it is not clear that systematic errors in the main experiment $e^+e^- \to Z^o \to$ all, at resonance, will permit a determination of the width to the required accuracy.

A method less dependent on current prejudices has been proposed:[46] Since the numbers of fundamental fields N_ℓ, $N_{2/3}$, and $N_{-1/3}$ are not known,

and since vertex corrections result in theoretical uncertainties, at the few percent level, in the effective quark couplings to the Z^o, one should determine separately each of the total, hadron (Γ_h), and charged lepton (Γ_{cl}) widths obtaining the neutrino width $\Gamma_{\nu\bar{\nu}}$ from the relation

$$\Gamma_{\nu\bar{\nu}} = \Gamma_Z - \Gamma_h - \Gamma_{cl} \tag{21}$$

This determination is a sensitive measure of $\Gamma_{\nu\bar{\nu}}$, but the experimental difficulties have been compounded: in addition to an accurate determination of Γ_Z, the measurement of the partial widths Γ_h, Γ_{cl}, demand knowledge of the integrated luminosity and of the electronic width. For instance, at resonance,

$$\Gamma_h = \sigma_h \frac{\Gamma_Z}{\sigma_{total}} = \left(\frac{N_h}{L}\right) \cdot \Gamma_Z \cdot \left(\frac{M_Z^2}{12\pi} \cdot \frac{\Gamma_Z}{\Gamma_e}\right) , \tag{22}$$

where N_h is the number of hadronic events, L is the integrated luminosity, and Γ_e is the electronic width. The experimental hardships are evident.

All these considerations have motivated the study of radiative Z^o production. This method involves Z^o tagging in the reaction

$$e^+e^- \to \gamma\nu\bar{\nu} \tag{23}$$

As discussed in Ref. 45, the SLC is to be operated at a center-of-mass energy above the Z^o mass. A photon is observed with an energy such that the recoil system has an energy about equal to the Z^o mass. Auxiliary detectors surround the collision point to separate those reactions in which no charged particles, neutral hadrons, or additional photons emerge ($Z^o \to \nu\bar{\nu}$), from those in which such additional particles do emerge. From the rate of this process N_ν can be obtained. In the standard model, the cross section for radiative neutrino pair production, corresponding to the Feynman diagrams of Fig. 34, is given by[45]

$$\frac{d^2\sigma}{dx\,dy} = \frac{G_F^2\,\alpha\, s(1-x)\left[(1-x/2)^2 + x^2y^2/4\right]}{6\pi^2\, x\,(1-y^2)} \times \left\{ \frac{N_\nu\left(g_V^2 + g_A^2\right) + 2(g_V + g_A)\left[1 - s(1-x)/M_Z^2\right]}{\left[1 - s(1-x)/M_Z^2\right]^2 + \Gamma_Z^2/M_Z^2} + 2 \right\} \tag{24}$$

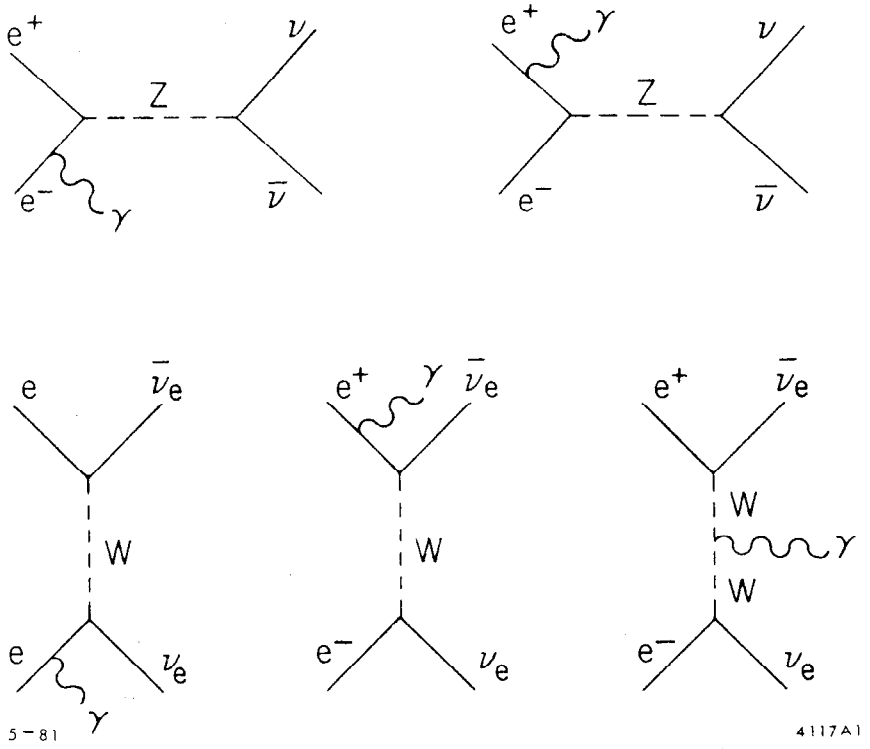

Fig. 34. Lowest order Feynman diagrams contributing to the process $e^+e^- \to \gamma\nu\bar{\nu}$.

where G_F is the fermi coupling constant, α is the fine structure constant, $\sqrt{s}$ is the square of the e^+e^- center-of-mass energy, x is the photon energy in units of the beam energy, and y is the cosine of the photon angle with respect to the incident beam direction; in the standard model $g_V = -1/2 + 2\sin^2\theta_w$ and $g_A = -1/2$. Figure 35 shows this cross section, integrated over photon angles, versus photon energies at $\sqrt{s}$ = 105 GeV for the mass M_Z = 90 GeV in a detector covering the range $20^o \leq \theta_\gamma \leq 160^o$.

The $e^+e^- \rightarrow \gamma\nu\bar{\nu}$ cross section integrated over the region E = 14 ± 2.5 GeV is ≈0.025 nb. A 30 day run at an average luminosity of 5×10^{30} cm^{-2} sec^{-1} will produce about 300 events with photon energies within ±2.5 GeV of the Z^o peak, enough to determine the number of neutrinos to sufficient accuracy, since the cross section increases by 0.008 nb for each additional neutrino. The contributions to the rate by the main background processes, radiative Bhabha scattering $e^+e^- \rightarrow \gamma e^+e^-$ and three photon annihilation $e^+e^- \rightarrow \gamma\gamma\gamma$, can be kept at a tolerable level since there exists a kinematic constraint between the minimum transverse momentum of the detected photon in the apparatus and the minimum angle with respect to the beam direction above which at least one other final state particle must appear. For the photon detection limits used in the example above this angle is about 2.5^o. Calculations[45] bear out a limit less stringent than 2.5^o on the solid angle coverage of the detector, the background being less than 10% of the signal for a detector covering down to about 6^o from the beam direction. The total solid angle of 0.995 × 4π sr is to be instrumented with an electromagnetic shower calorimeter, adequately segmented, with a resolution of 3% at 15 GeV or $\Delta E/E = 12\%/\sqrt{E}$, to permit the observation of the Z^o peak in the photon spectrum. A crude charged particle tracking system with the same coverage is also required to veto any charged prongs, but no large volume magnetic fields or calorimeters are required. This process could thus be measured by a limited scope detector. However, radiative neutrino pair production may also be accessible to a general facility detector, provided it reaches down to small angles ≈100 mr around the beam pipes. For both the specialized and the general facility detector the forward and backward cones around the beams require special care to shield them from direct and scattered synchrotron radiation backgrounds.[47]

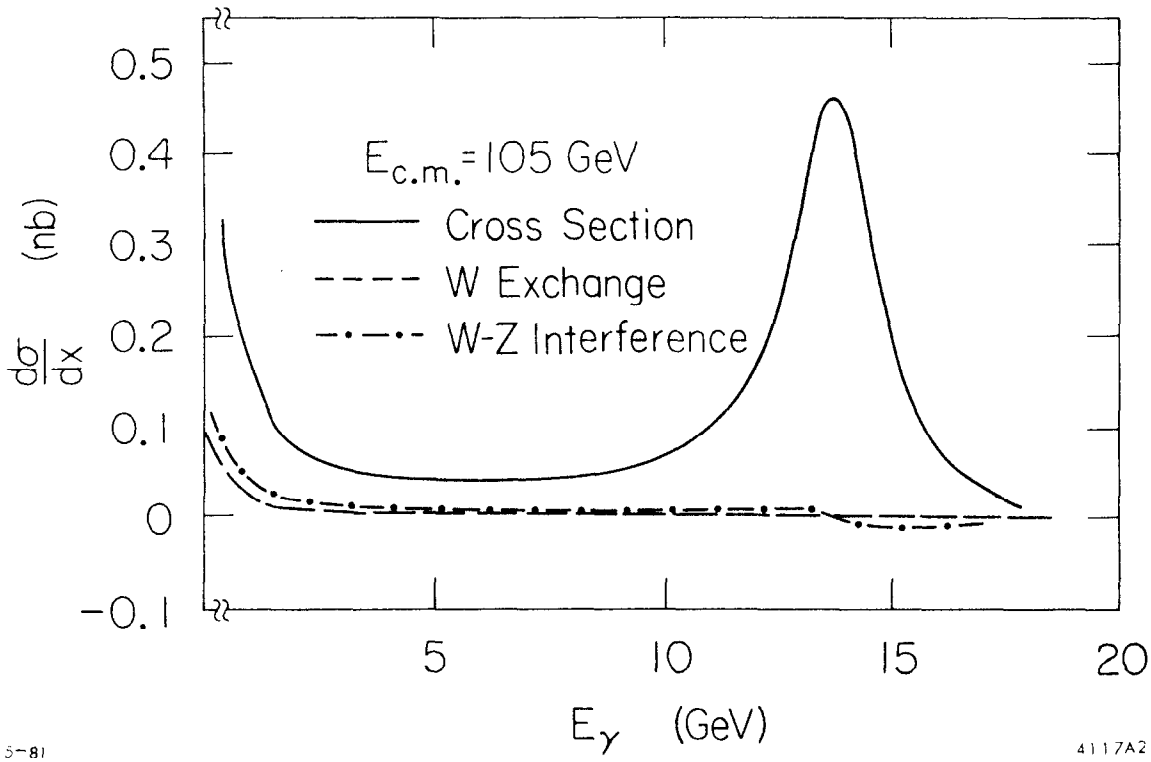

Fig. 35. Differential cross section dσ/dx versus the photon energy E_γ. The three curves are for the total cross section, the contribution from W exchange, and the W-Z inteference term.

B. Higgs Boson Search

One of the most exciting areas which can perhaps be explored with an e^+e^- collider at the Z^o is the existence of the Higgs boson. For the standard model with one neutral Higgs particle, the dominant production mechanism is

$$e^+ + e^- \rightarrow Z^o \rightarrow H^o + Z^{o\prime},$$

where H^o is the Higgs boson and $Z^{o\prime}$ is a virtual Z^o of mass smaller than the Z^o mass. The most conveniently studied channel is one in which the $Z^{o\prime}$ decays into a high-mass pair of leptons. In the standard model, the partial width for the process $Z^o \rightarrow H^o \ell^+ \ell^-$ with invariant mass of lepton pair equal to M_L is given by,

$$\frac{1}{\Gamma(Z^o \rightarrow \mu^+\mu^-)} \frac{d\Gamma(Z^o \rightarrow H^o\, \ell^+\ell^-)}{dM_L} = \frac{\alpha F}{4\pi \sin^2\theta_w \cos^2\theta_w}$$

where

$$F = \frac{10K^2 + 10^2\lambda + 1 + (K^2 - \lambda^2)^2 \left[(1 - K^2 - \lambda^2)^2 - 4K^2\lambda^2\right] 1/2}{(1 - K^2)^2} \qquad (25)$$

and $K = M_L/M_{Zo}$, $\lambda = M_{Ho}/M_{Zo}$. The above ratio integrated over M_L is shown as a function of M_H in Fig. 36. Clearly for $M_H > 20$ GeV, the low rate is a very serious problem. The dilepton mass spectrum is shown in Fig. 37. As expected from the denominator in the above formula, the spectrum peaks at high mass.

The identification of the above reaction has been considered with both dimuons and dielectrons.[48] Because of both the greater ease of identifying high energy electrons (well separated here from the jets produced by the Higgs decay products) and the much better energy measurements of the electrons by calorimetry, the $H^o e^+ e^-$ final state is highly favored and is exclusively considered in the following discussion.

Figure 38 shows e^+e^- mass spectra from $H^o e^+ e^-$, and e^+e^- background spectra from multijet hadronic Z^o final states (Z^o mass = 94 GeV, M_t = 25 GeV). The background can be substantially reduced with almost no loss in signal by a requirement that each electron make an angle greater than 200 mr with the sphericity axis of the particles remaining after removal of the leptons. The corresponding background level is shown by the dashed

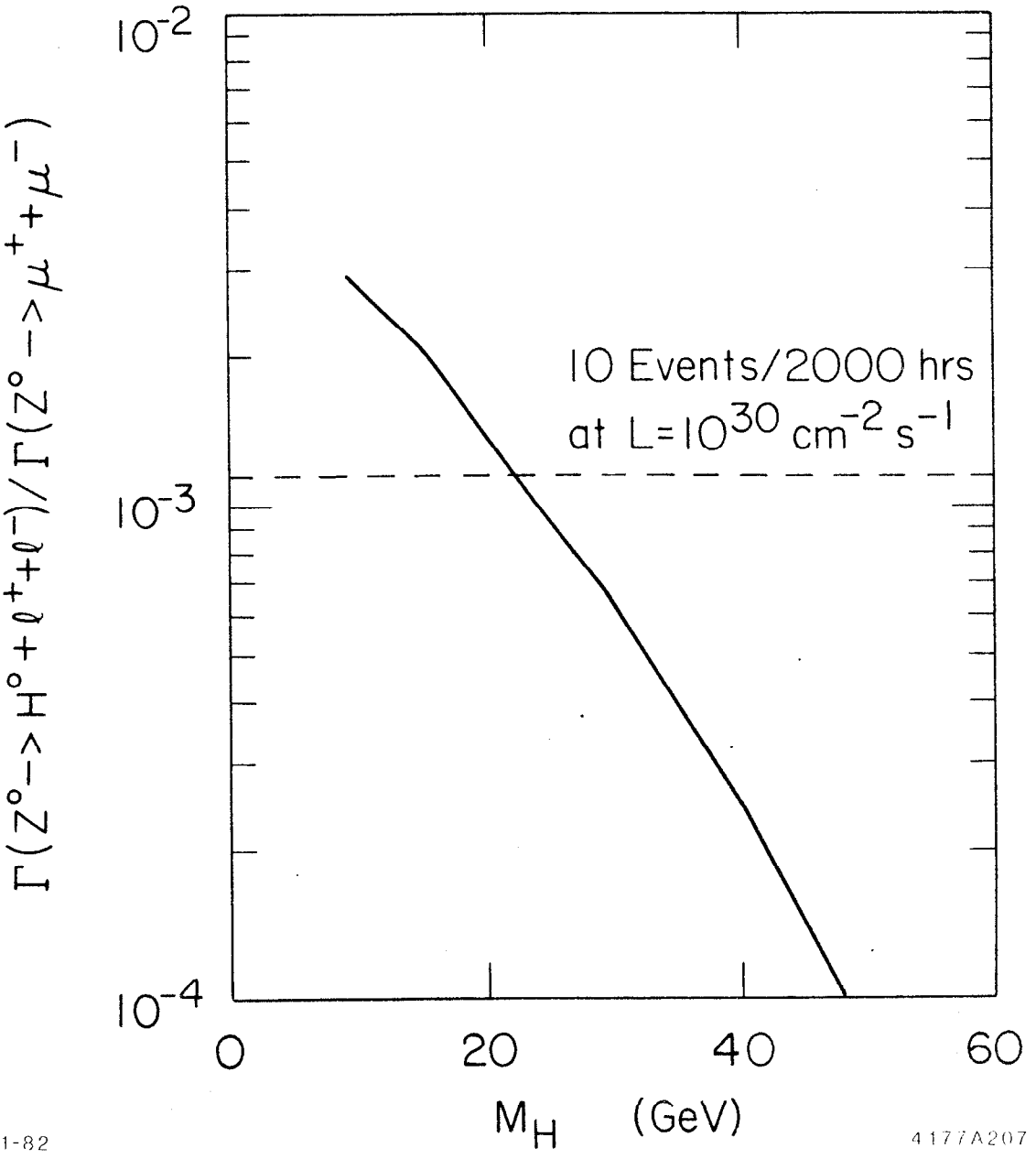

Fig. 36. Ratio $\Gamma(Z^o \to H^o \ell^+ \ell^-)/\Gamma(Z^o \to \mu^+ \mu^-)$ as a function of M_H, the Higgs boson mass.

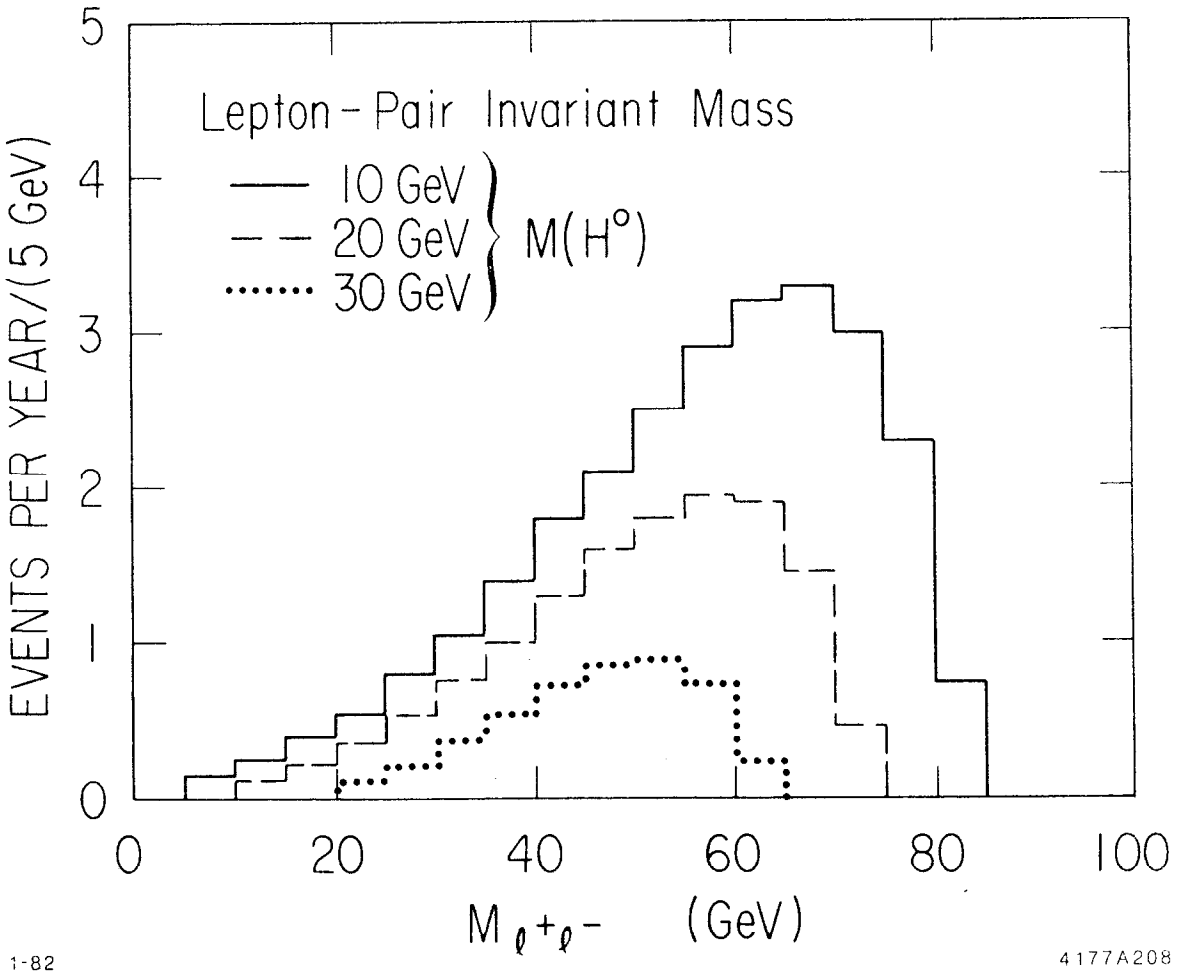

Fig. 37. Dilepton mass spectra in $Z^{o} \rightarrow H^{o}\ell^{+}\ell^{-}$ for various Higgs boson masses. The normalization corresponds to 2000 hours at an average luminosity of 10^{30} cm^{-2} sec^{-1}.

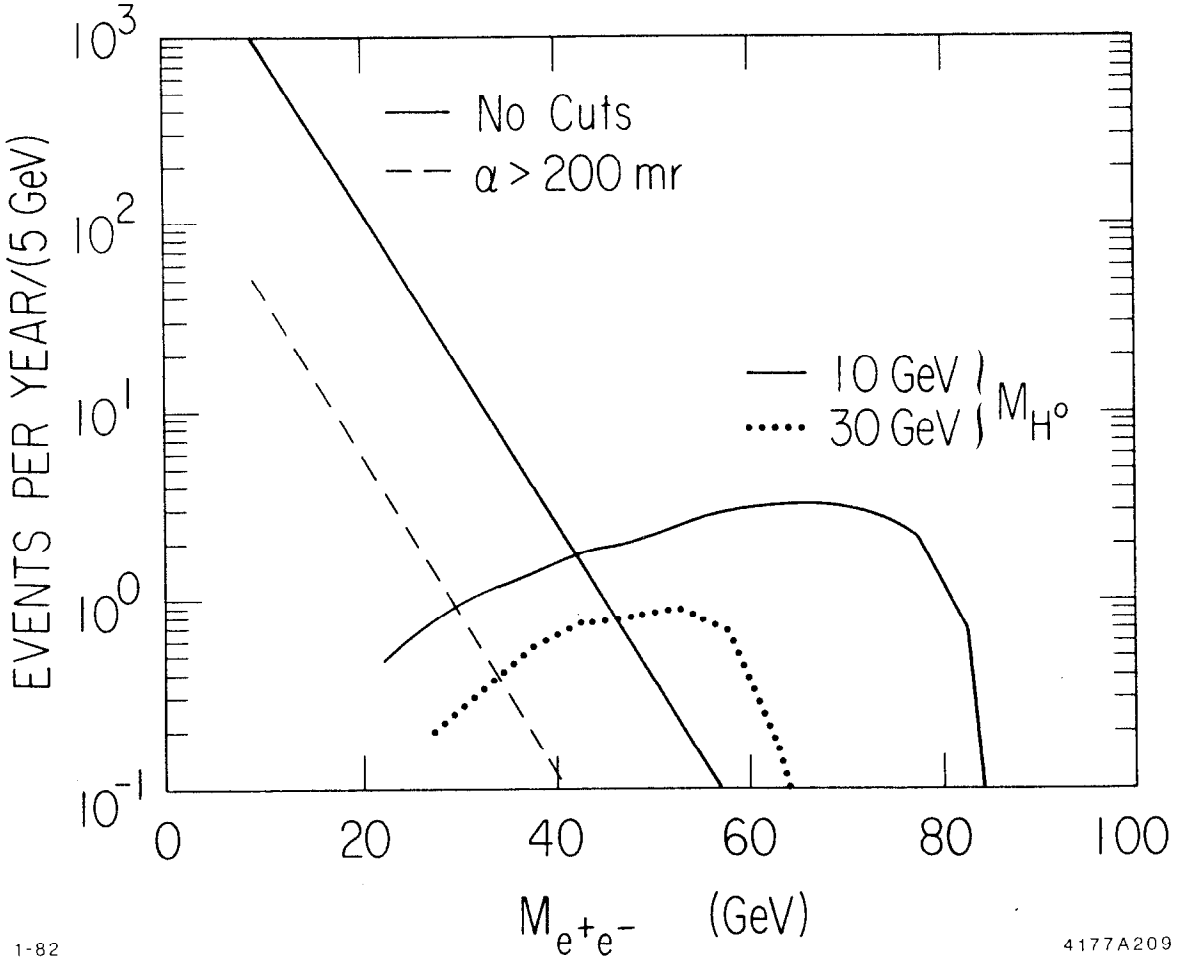

Fig. 38. Electron-positron pairs mass spectra for:

(i) e^+e^- pairs from jets without cuts (solid line),
(ii) e^+e^- pairs from jets with 200 mr cut described in text (dashed line),
(iii) e^+e^- pairs from $Z^o \to H^o e^+e^-$, M_H = 10 GeV (solid curve),
(iv) e^+e^- pairs from $Z^o \to H^o e^+e^-$, M_H = 30 GeV (dashed curve).

line in Fig. 38. It is clear that for $M_L > 40$ GeV the signal to background ratio is rather good. It is worth noting that without the electron identification the background lines in Fig. 38 are a factor of about 300 higher. This sets the requirement for electron-hadron separation.

Having established a credible high mass dilepton signal, one needs to look at the mass spectrum recoiling against the dilepton system to establish further the presence of the Higgs and determine its mass. A scatter plot of recoil mass versus dilepton mass for $M_{H^o} = 10$ GeV, based on an electromagnetic calorimeter of resolution $10\%/\sqrt{E}$ is shown in Fig. 39. The recoil mass spectrum has a σ of about 1 GeV. A calorimeter of resolution $20\%/\sqrt{E}$ would roughly double the width of the recoil mass spectrum (the effect of energy spread is relatively small), and still deliver a useful result.

There is an important further background to the $H^o e^+ e^-$ final state, namely the production of two outgoing electrons plus a low mass hadronic system through two-photon processes. The estimated recoil mass spectrum from such processes with both electrons separated from the beam by at least 100 mr is shown in Fig. 40, again for $10\%/\sqrt{E}$ calorimeter resolution and $M_{H^o} = 10$ GeV. It is clear that the two-photon background sets a lower limit to observable M_{H^o} of about 8 GeV. With poorer resolution that lower limit may even be somewhat higher.

In conclusion, detection of the process $Z^o \to H^o e^+ e^-$ appears hopeful for H^o masses in the range of 10-30 GeV with reasonable electromagnetic calorimetry.

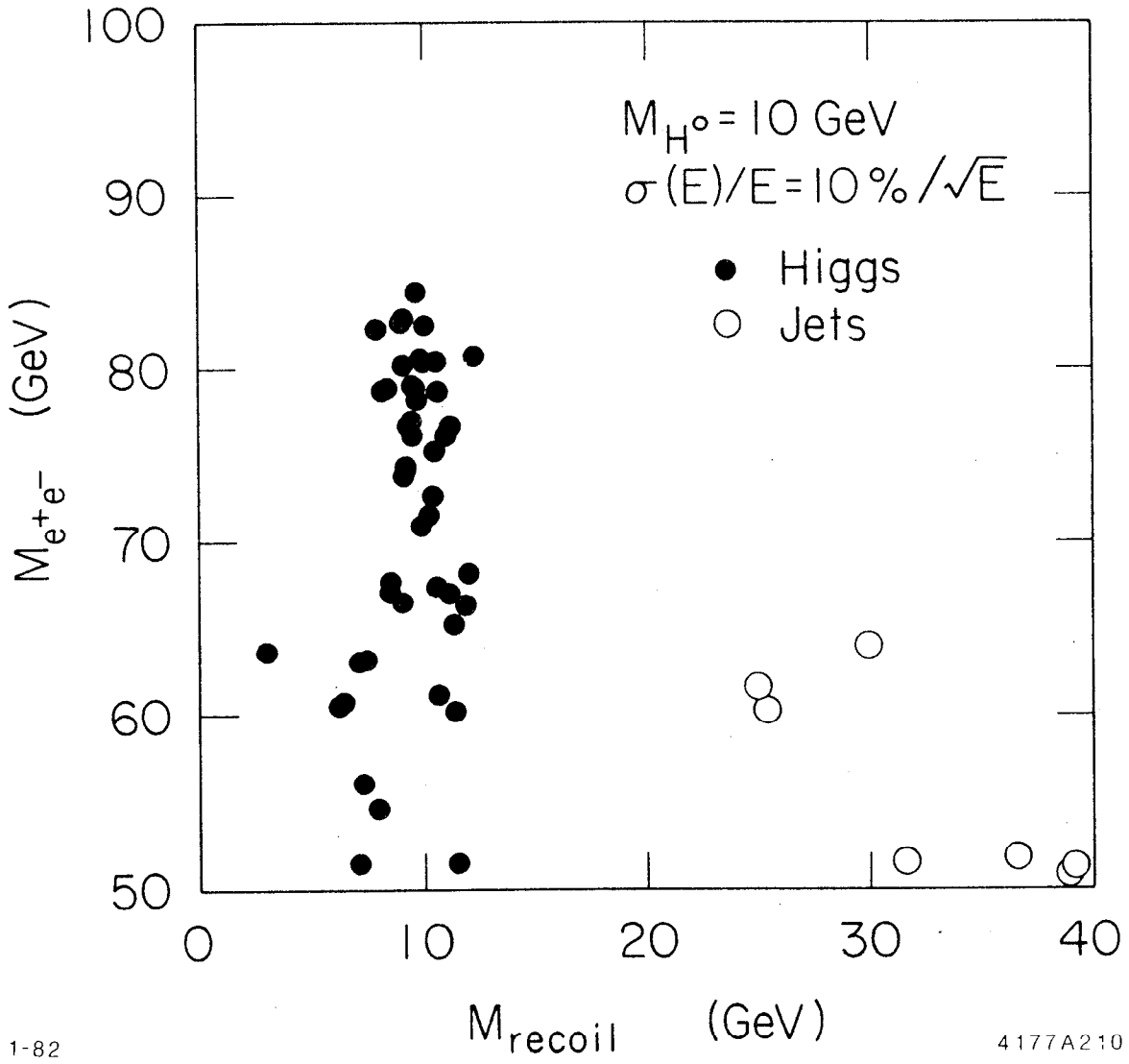

Fig. 39. Scatter plot of $M(e^+e^-)$ versus recoil mass with calorimeter resolution $\Delta E/E = 0.1/\sqrt{E}$.

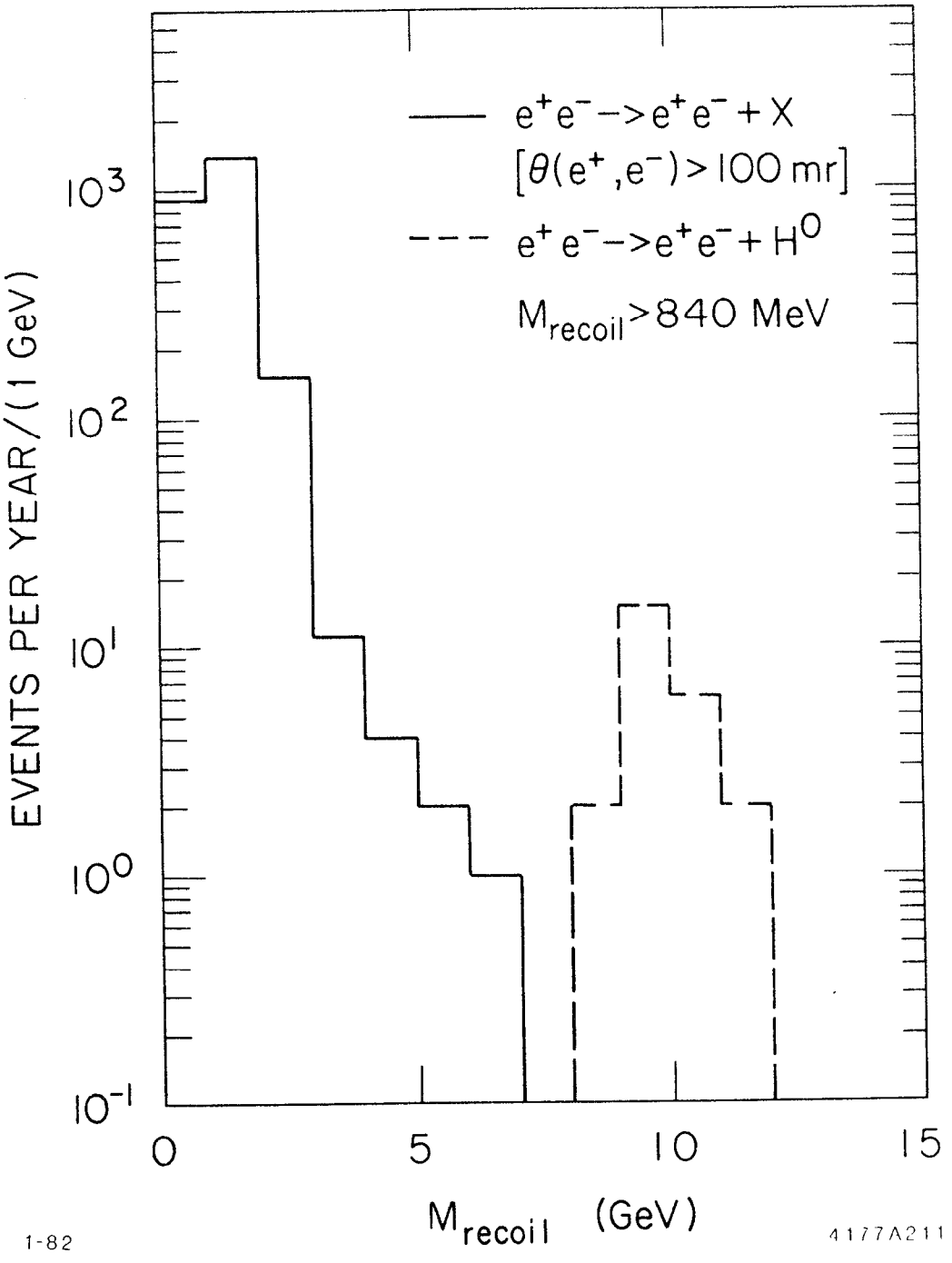

Fig. 40. Mass spectrum recoiling against high mass (>50 GeV) e^+e^- pairs from $Z^o \rightarrow H^o e^+e^-$ and $e^+e^- \rightarrow e^+e^- + X$.

V. CONCLUSIONS

A. Summary of Impact of Detector Properties on Physics

In this section we summarize those detector properties which seem to be demanded by the considerations of the previous sections.

1. Solid Angle

For the consideration of solid angle, Figs. 8 and 31, and Tables VII and VIII are relevant. From all these inputs, it appears that a solid angle for both tracking and calorimetry of at least 90% of 4π is highly desirable. It has been found that one can achieve this solid angle in a cylindrical tracking detector with uniformly spaced layers with a ratio of length to diameter of about 4/3 (assuming no tracking detectors in the end caps).

2. Momentum Resolution in Tracking Detector

A number of processes requiring accurate momentum measurements are given below,[49] and corresponding values of $f = \sigma_p/p^2$ (GeV^{-1}) are suggested:

(a) Study of Single Particle Exclusive Spectra. If one requires $\sigma_p/p \approx 10\%$ at 50 GeV/c, $f = 0.2\%$.

(b) Charged Particle Identification by p versus β. It has been shown that $f \approx 20\%/p$ for π,K,p separation. At $p = 50$ GeV/c, this gives $f = 0.4\%$.

(c) Electron Identification by p versus E. One might match the calorimeter energy resolution to the tracking momentum resolution at some appropriate momentum, $\sigma_E/E = \sigma_p/p$. If $\sigma_E/E = 10\%/\sqrt{E}$, and one matches at $p = 10$ GeV/c, $f = 0.3\%$.

(d) Identification of K_s from $\pi^+\pi^-$ Effective Mass. One can show that $f \approx \sqrt{8}\left(\frac{\Delta M_K}{M_K}\right)/p_K$ where ΔM_K is the standard deviation in the K mass measurement and p_K is the K momentum. For $\Delta M_K = 10$ MeV and $p_K = 20$ GeV/c, $f = 0.3\%$.

It should also be noted that angular resolution plays an important role, $\sigma_\theta \approx 2\,\Delta M_K/p_K$. For the same ΔM_K and p_K, one finds $\sigma_\theta \approx 1$ mr. These formulas are entirely consistent with the $\pi^+\pi^-$ mass spectrum shown in Fig. 26.

(e) Studies of $Z^o \to \mu^+\mu^-$. For correct assignment of signs of μ^+ and μ^- at the 3σ level, f = 1.0%.

(f) Studies of τ Polarization from $Z^o \to \tau^+\tau^-$. For adequate measurement of polarization, f = 0.5%.

From all these considerations it appears that $f \lesssim 0.5\%$ is highly desirable. It is important to note that the actual value of f achieved from a given detector configuration will depend, for a particular track, on the actual number of layers in which unconfused hits are recorded, on the polar angle of the track; and, on whether the beam-beam interaction point can be used to constrain the track fit.

3. Segmentation in Tracking Detector

Information on segmentation is given in Figs. 9, 10 and 12, and Tables II and IV for cylindrical detectors with pattern recognition based principally on x - y (and not z) information. The track confusion problem is greatest for intermediate momenta (5 to 15 GeV/c). The analysis can be summarized by saying that high tracking efficiency at all momenta requires the ability to associate hits correctly with the appropriate tracks even when pairs of tracks are separated by as little as 2.5 mm over as much as half their lengths in the detector. For vertex drift chambers of inner and outer radii 10 and 30 cm respectively, the corresponding number is 0.5 mm. These figures of 2.5 mm and 0.5 mm put requirements on both the number of good hits which must be available per track and on the quality of the position information which must be used at the pattern recognition stage. For drift chambers of the small cell, single hit Mark II/CLEO design, approximately 40 layers comprising 8000 cells are required.

4. Vertex Detector

With two CCD planes at radii of 1 and 2 cm respectively, one can summarize the requirements as follows:

(a) To have less than 10% confusion of adjacent tracks one needs an overlap resolution of $<200\mu$ for a two-dimensional device and $<50\mu$ for a one-dimensional device.

(b) For three measurement precision levels one can summarize typical efficiencies for finding tracks from D decays and the corresponding fraction of the found tracks which really come from D decays:

Precision =	Efficiency ≈	Purity ≈
3 μ	60%	80%
10 μ	40%	70%
30 μ	25%	60%

5. Remarks on Electromagnetic Calorimetry

(a) π^o Reconstruction. π^o reconstruction is principally impacted by the resolution of the two decay photons and the accurate measurement of the angle between them. Angular resolutions of $\lesssim$5 mr and energy resolutions of $0.1/\sqrt{E}$ are required to reconstruct π^o over some reasonable momentum range.

(b) $Z^o \to \tau^+\tau^-$ — Polarization Measurements. Separation of relevant decay modes required an energy resolution of $0.12/\sqrt{E}$ and an effective cell size of 40 mr × 40 mr.

(c) Neutrino Counting. The electromagnetic calorimeter for study of $e^+e^- \to \gamma\nu\bar{\nu}$ requires an energy resolution of about $0.12/\sqrt{E}$ and a complete solid angle coverage down to within 6^o of the beam direction.

(d) $Z^o \to H^o e^+ e^-$. An energy resolution for electrons of about $0.1/\sqrt{E}$ and a hadron rejection of $\leqq 1/500$ for electron energies $\gtrsim$20 GeV are required for the Higgs search.

6. Muon Identification

To detect muons from t, b and c decays a detector should have a total amount of material equivalent to at least 1 meter of iron and a detector system with spatial resolution of 1/2 cm. Segmentation of the iron into layers would be useful to improve hadron-muon separation. With one meter of iron and a central detector which cannot distinguish π from K, the ratio of signal to punch-through will be ~2 for μ^- and ~1.3 for μ^+ in the 2 - 30 GeV/c momentum range. Ability to separate K would improve these ratios by about a factor of 2.

REFERENCES

1. G. G. Hanson, SLC Workshop Note No. 9 (1981).

2. A. Ali et al., Phys. Lett. 93B, 155 (1980).

3. C. Day, SLC Workshop Note No. 7 (1981)

4. T. Sjostrand, LUTP 80-3 (1980).

5. S. L. Glashow, Nucl. Phys. 22, 479 (1961); S. Weinberg, Phys. Rev. Lett. 19, 1264 (1967); A. Salam, Proc. 8th Nobel Symposium on Elementary Particle Physics, Stockholm, Sweden, 1968, ed. by N. Suartholm (Almquist and Wiksell), p. 367.

6. J. D. Bjorken, Proc. of the Summer Institute on Particle Physics, SLAC Report 198, November 1976.

7. V. Lüth, SLC Workshop Note No. 18 (1981).

8. V. Lüth, Calorimeter Group Report, these proceedings.

9. R. Fabrizio, SLC Workshop Note No. 30 (1981).

10. G. J. Tarnopolsky, SLC Workshop Note No. 11 (1981).

11. J. Nishimura, Handbuck der Physick 46 II, 96 (1965).

12. G. H. Trilling, SLC Workshop Note No. 13; SLC Workshop Note No. 46 (1981).

13. T. Yuda, Nucl. Instrum. Methods 73, 301 (1969).

14. John Hauptman, SLC Workshop Note No. 27 (1981).

15. H.F.W. Sadrozinski, SLC Workshop Note No. 23 (1981).

16. D. Coyne, V. Lüth, L. Price and H. Williams, SLC Workshop Note No. 29 (1981).

17. B. N. Ratcliff, SLC Workshop Note No. 59 (1981).

18. H.F.W. Sadrozinski, SLC Workshop Note No. 58 (1981).

19. G. J. Tarnopolsky, private communication.

20. J. M. Dorfan, SLC Workshop Note No. 56 (1981).

21. J. D. Bjorken and S. J. Brodsky, Phys. Rev. D1, 1416 (1970).

22. G. G. Hanson et al., Phys. Rev. Lett. 35, 1609 (1975).

23. J. M. Dorfan, Z. Phys. C7, 349 (1981); also see SLAC-PUB-2813.

24. See Reference 7.

25. B. Blumenfeld, B. Barnett, and David Hon, SLC Workshop Note No. 26 (1981).

26. A. Grant, Nucl. Instrum. Methods 130, 167 (1975).

27. G. J. Tarnopolsky, SLAC-PUB-2842 (SLC Workshop Note No. 43)(1981).

28. The error in $\sin^2\theta_W$ is assumed to be one order of magnitude smaller than its present valve, since that precision will be achieved by the measurement of the Z^o mass.

29. J. M. Dorfan, SLC Workshop Note No. 55 (1981).

30. G. Bonneaud, M. de Crombrugghe and C. Y. Prescott, SLC Workshop Note No. 32 (1981).

31. M. Greco, G. Pancheri-Srivastava and Y. Srivastava, Nucl. Phys. B171, 118 (1980).

32. See Reference 18.

33. W. Hollik, Z. Phys. C8, 149 (1981).

34. M. Holder et al., Nucl. Instrum Methods 148, 235 (1978).

35. J. H. Field and B. Richter, in Physics with Very High Energy e^+e^- Colliding Beams, CERN 76-18 (1979).

36. G. J. Tarnopolsky, private communication.

37. James W. Cronin and Morris L. Swartz, Fermilab proposal 600 (1978).

38. G. J. Feldman et al., Phys. Rev. Lett. 48, 66 (1982).

39. L. B. Okun, Weak Interaction of Elementary Particles; S. V. Golovkin et al., Nucl. Instrum. Methods 138, 235 (1976).

40. Y. S. Tsai, Phys. Rev. D4, 2821 (1971).

41. J. E. Brau and G. J. Tarnopolsky, Phys Rev. D24, 2521 (1981), and Reference 40.

42. J.A.M. Vermaseren et al., Phys. Rev. D19, 137 (1979) and references therein.

43. James E. Brau and G. J. Tarnopolsky, SLC Note No. 41 (1981).

44. John Hauptman, SLC Note No. 37 (1981).

45. G. Barbiellini, B. Richter and J. L. Siegrist, Phys. Lett. 106B, 414 (1981).

46. R. J. Cence, SLC Note No. 48 (1981).

47. E. S. Miller and J. C. Sens, SLC Workshop Note No. 43 (1981).

48. P. Kooijman, SLC Workshop Note No. 57 (1981).

49. H. Lynch, SLC Workshop Note No. 40 (1981).

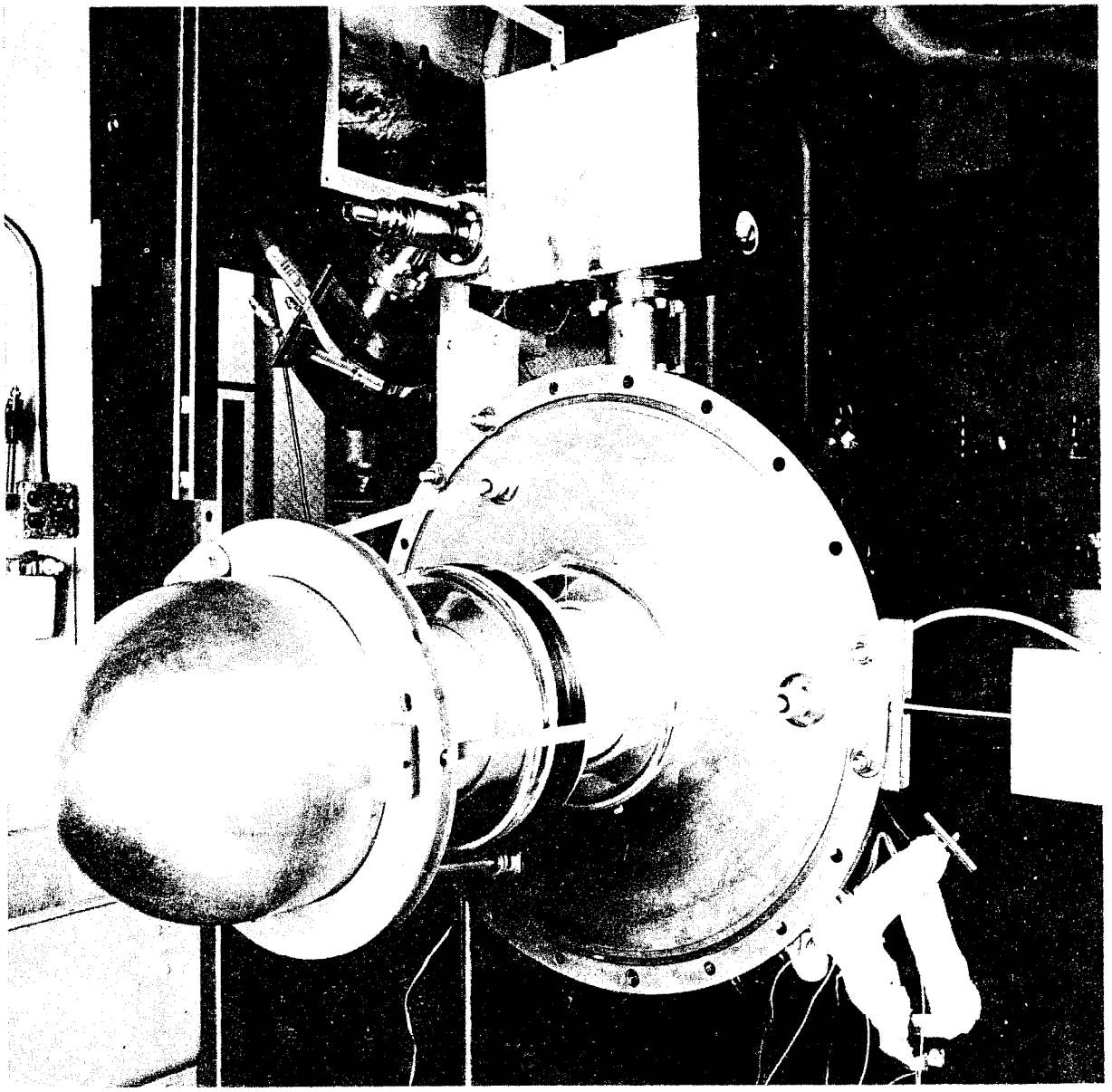

This photograph shows the back structure of a high-current laser-activated gun being developed for producing intense, tightly bunched beams of polarized electrons for the SLC. A high-performance thermionic gun is already in use in the SLC testing program and has given up to 20 nanocoulombs of charge in a single S-band bunch.

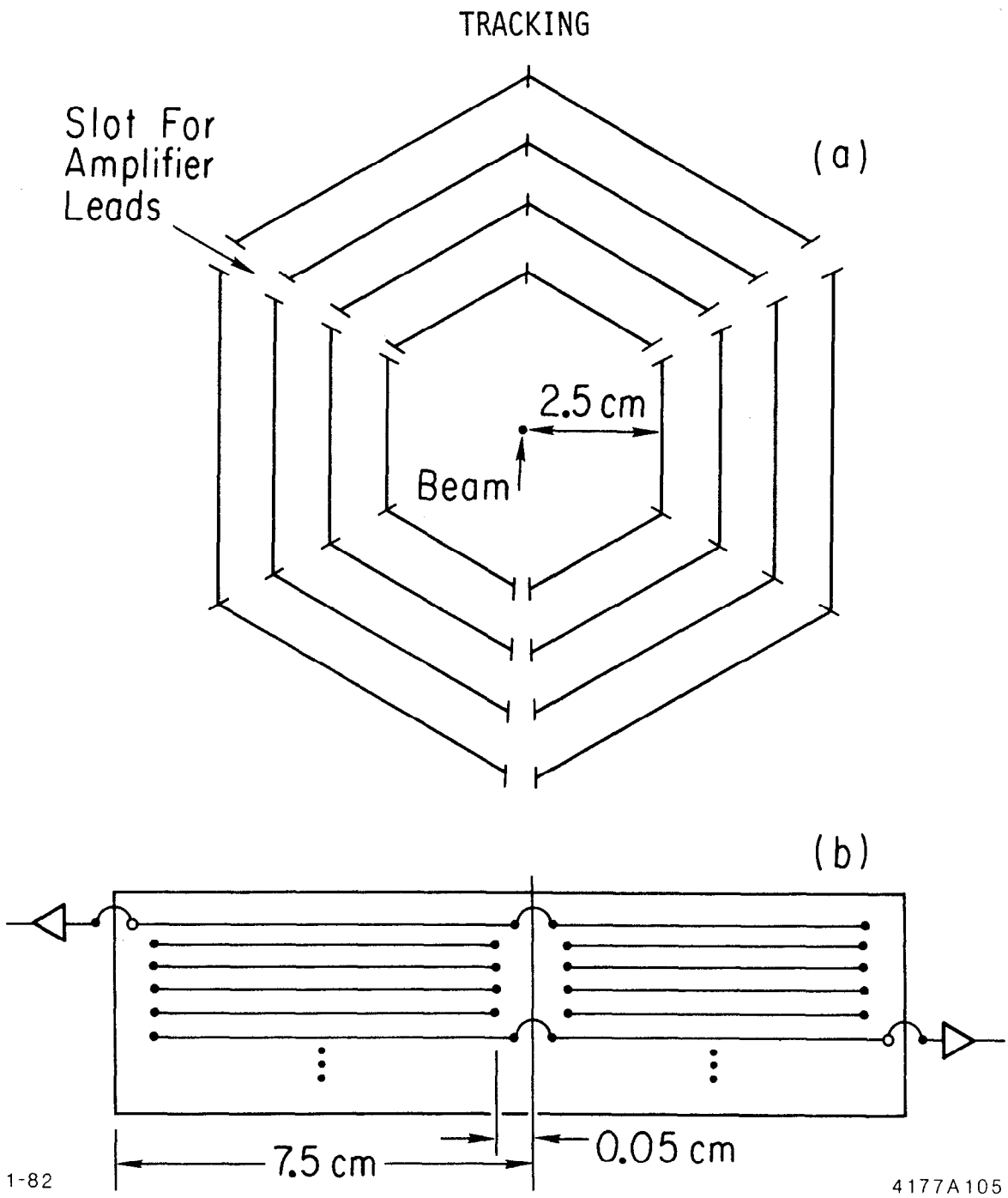
TRACKING
Slot For
Amplifier
Leads
(a)
2.5 cm
Beam
(b)
7.5 cm
0.05 cm
1-82
4177A105

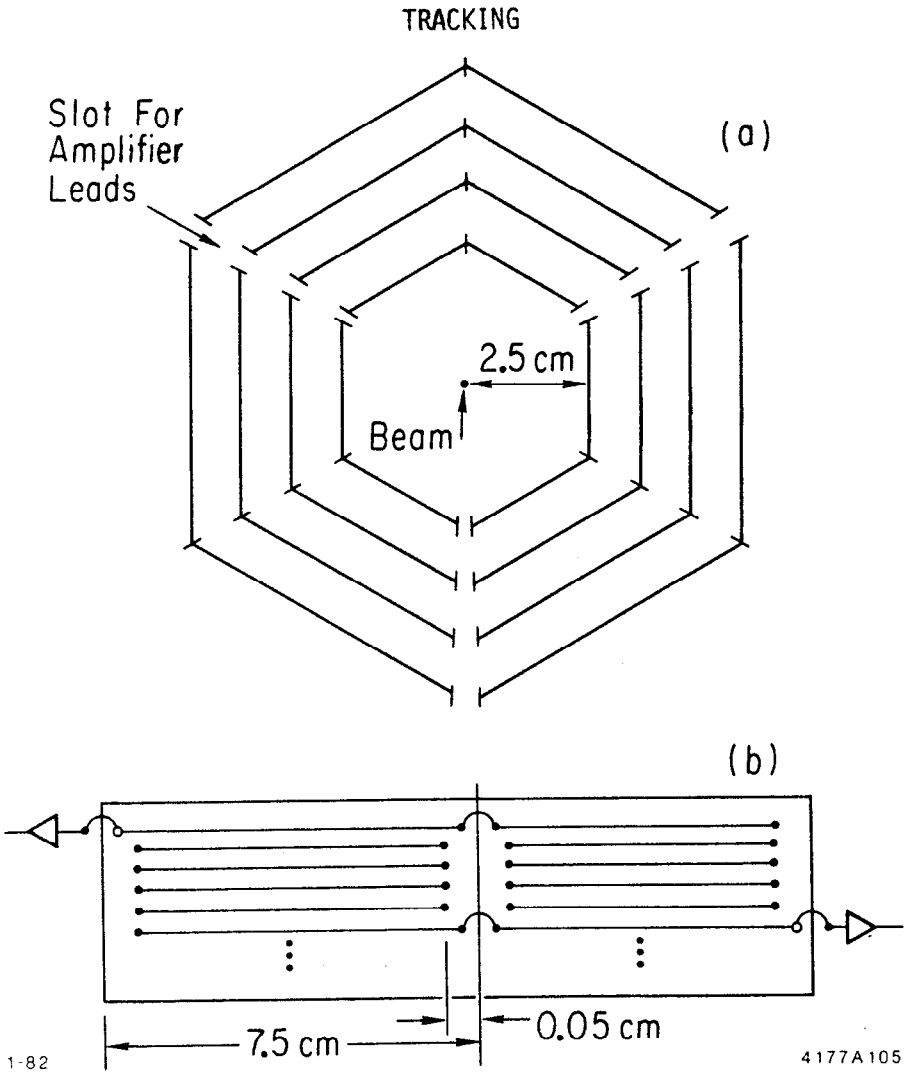
TRACKING
Slot For
Amplifier
Leads
(a)
2.5 cm
Beam
(b)
7.5 cm
0.05 cm
1-82
4177A105